Order Number 9026325

A finite difference numerical model for the propagation of finite amplitude acoustical blast waves outdoors over hard and porous surfaces

Sparrow, Victor Ward, Ph.D.

University of Illinois at Urbana-Champaign, 1990

U·M·I
300 N. Zeeb Rd.
Ann Arbor, MI 48106

A FINITE DIFFERENCE NUMERICAL MODEL FOR THE PROPAGATION OF FINITE AMPLITUDE ACOUSTICAL BLAST WAVES OUTDOORS OVER HARD AND POROUS SURFACES

BY

VICTOR WARD SPARROW

B.S., Duke University, 1985
M.S., University of Illinois, 1987

THESIS

Submitted in partial fulfillment of the requirements
for the degree of Doctor of Philosophy in Electrical Engineering
in the Graduate College of the
University of Illinois at Urbana-Champaign, 1990

Urbana, Illinois

UNIVERSITY OF ILLINOIS AT URBANA-CHAMPAIGN

THE GRADUATE COLLEGE

APRIL 1990

WE HEREBY RECOMMEND THAT THE THESIS BY

VICTOR WARD SPARROW

ENTITLED A FINITE DIFFERENCE NUMERICAL MODEL FOR THE PROPAGATION OF FINITE AMPLITUDE ACOUSTICAL BLAST WAVES OUTDOORS OVER HARD AND POROUS SURFACES

BE ACCEPTED IN PARTIAL FULFILLMENT OF THE REQUIREMENTS FOR THE DEGREE OF DOCTOR OF PHILOSOPHY

Director of Thesis Research

Head of Department

Committee on Final Examination†

Chairperson

† Required for doctor's degree but not for master's.

O-517

A FINITE DIFFERENCE NUMERICAL MODEL FOR THE PROPAGATION OF FINITE AMPLITUDE ACOUSTICAL BLAST WAVES OUTDOORS OVER HARD AND POROUS SURFACES

Victor Ward Sparrow, Ph.D.
Department of Electrical and Computer Engineering
University of Illinois at Urbana-Champaign, 1990

This study has concerned the propagation of finite amplitude, i.e., weakly nonlinear, acoustical blast waves from explosions over hard and porous media models of outdoor ground surfaces. The nonlinear acoustic propagation effects require a numerical solution in the time domain. To model a porous ground surface, which in the frequency domain exhibits a finite impedance, the linear phenomenological porous model of Morse and Ingard was used. The phenomenological equations are solved in the time domain for coupling with the time domain propagation solution in the air.

The numerical solution is found through the method of finite differences. The second-order in time and fourth-order in space MacCormack method was used in the air, and the second-order in time and space MacCormack method was used in the porous medium modeling the ground. Two kinds of numerical absorbing boundary conditions were developed for the air propagation equations to truncate the physical domain for solution on a computer. Radiation conditions first were used on those sides of the domain where there were outgoing waves. Characteristic boundary conditions secondly are employed near the acoustic source.

The numerical model agreed well with the Pestorius algorithm for the propagation of electric spark pulses in the free field, and with a result of Pfriem for normal

plane reflection off a hard surface. In addition, curves of pressure amplification versus incident angle for waves obliquely incident on the hard and porous surfaces were produced which are similar to those in the literature. The model predicted that near grazing finite amplitude acoustic blast waves decay with distance over hard surfaces as $r^{-1.2}$. This result is consistent with the work of Reed. For propagation over the porous ground surface, the model predicted that this surface decreased the decay rate with distance for the larger blasts compared to the rate expected in the linear acoustics limit.

DEDICATION

This thesis is dedicated to the glory of God. Of the Lord's creations one of my favorites must be the wave, since through waves our senses of hearing and seeing reveal the magnificent beauty of the world around us.

ACKNOWLEDGEMENTS

I first thank my advisor, Dr. Richard Raspet. He introduced me to the need for research on finite amplitude wave reflection and attracted me to the University of Illinois, Urbana-Champaign, to work in acoustics. His encouragement, patience, and lucid understanding of the difficulties involved in this work were without bound throughout my graduate training. I feel I was fortunate to have been his student.

Next, I thank my other committee members Drs. Franke, O'Brien, and Swenson for helping in reviewing my work. I greatly appreciate Dr. Franke chairing my committee, and I thank him and Drs. Swenson and O'Brien for their valuable comments.

I also want to express my gratitude to Dr. Schomer, Dr. White, Dr. Pater, and everyone else at the U. S. Army Construction Engineering Research Laboratory in Champaign, IL. Their steadfast financial support, forethought for long term research, and helpfulness made this work possible. Numerous enjoyable conversations with Drs. Swenson and White over lunch also had a significant impact on keeping my sanity and on this research generally.

The computational support provided by the National Center for Supercomputing Applications in Champaign, IL is additionally acknowledged. Almost all the numerical simulations presented in this thesis were performed either on their Cray-XMP or Cray-2 supercomputers and their post-processing software. I also appreciate the comments and suggestions of several researchers at other institutions. They are James Sabatier, Henry Bass, Mark Hamilton, David Blackstock, Jacqueline Naze

Tjótta, Keith Attenborough, Tony Embleton, Gilles Daigle, and Robert Higdon.

I also thank all my family for their support, especially Mom, Dad, and "G." And, Jan, I couldn't have done it without you. Thanks to you, most of all.

TABLE OF CONTENTS

LIST OF SYMBOLS

dB, decibel

h, hour

kg, kilogram

m, meter

min, minute

N, newton

Pa, mks pascal = N/m^2

s, second

a, pressure amplification factor

c_0, speed of sound in air

c_e, Morse and Ingard effective sound speed

c_{eff}, effective sound speed

c_p, specific heat at constant pressure

c_{v_ν}, specific heat contributions from internal vibrations of ν type molecules

d, cylindrical range coordinate

$\hat{d}$, d direction unit vector

E, energy release of explosive

f, frequency

F, acoustic system d direction conservation function

$F(t - r/c_0)$, spherical potential function

G, acoustic system z direction conservation function

G, numerical amplification matrix, Chapter 8

I, identity matrix

k, wavenumber

K, porous effective density factor

l_1, l_2, left eigenvectors

$L_d(\Delta t)$, finite difference operator in d direction

$L_z(\Delta t)$, finite difference operator in z direction

n, time epoch

n, dynamic shape factor, Chapter 5

$\tilde{n}$, temporary time epoch

N_2, nitrogen

O_2, oxygen

p, acoustic pressure

p, total pressure, Chapters 2 and 5

p', acoustic pressure, Chapters 2 and 5

p_i, incident total pressure

p_o, ambient pressure

q, tortuosity of porous material

r, spherical radial distance

$\bar{r}$, spherical discontinuity distance

r_{max}, spherical old age distance

r_o, effective radius

r_1, r_2, right eigenvectors

s, condensation, Chapter 2

s, static shape factor, Chapter 5

s_p, shape factor ratio

s_{fr}, entropy deviation with vibrations frozen

SF, acoustic system d direction "source" function

SG, acoustic system z direction "source" function

t, time

t_+, positive phase duration of Reed pulse

t_1, t_2, t_3, initial pulse duration parameters

T', temperature deviation

T_o, ambient temperature

T_1, T_2, apparent vibration temperatures

u, d component of particle velocity

u, particle velocity vector

v, z component of particle velocity

v_r, spherical coordinate radial particle velocity component

w, vector of acoustic variables

w, cylindrical characteristic variables vector

w', spherical characteristic variables vector

$w1$, $w2$, cylindrical characteristic variables

$w1'$, $w2'$, spherical characteristic variables

W, weight of explosive

W_o, reference weight

$\bar{x}$, plane discontinuity distance

x_{max}, plane old age distance

z, cylindrical height coordinate

Z, impedance

$\hat{z}$, z direction unit vector

α, absorption coefficient

α_i, incident angle i, Chapter 8

$(\alpha_i \lambda)_m$, maximum absorption per unit wavelength for the ith relaxation process

β, parameter of nonlinearity, Chapter 2

β, coefficient of volume (thermal) expansion

γ, ratio of specific heats

Δp_o, peak pressure of initial pulse

Δt, small increment in t

Δx, small increment in d or z

$\Delta \mu_B$, bulk viscosity increment

ϵ, acoustic Mach number

θ, spherical coordinates polar angle

κ, thermal conductivity

κ_e, Morse and Ingard effective compressibility

κ_p, Morse and Ingard effective compressibility in pores

λ, eigenvalue

μ, viscosity

μ_B, bulk viscosity

ν, artificial viscosity

ρ, total density

ρ', density deviation

ρ_e, Morse and Ingard complex effective density

ρ_o, ambient density

ρ_p, Morse and Ingard effective density in pores

τ, duration of Reed pulse

τ_i, ith relaxation time

ϕ, cylindrical and spherical azimuthal angle

Φ, flow resistance

ω, radian frequency

Ω, porosity

1. INTRODUCTION

What do the following situations have in common: a wailing civil defense siren, a refrigerating thermoacoustic engine, a jet airplane taking off from an airport, a hyperthermia treatment for a cancerous tumor, an outdoor blast from a small explosion, a lithotripsy treatment for breaking up a kidney stone, a parametric array on a submarine sending a low frequency sonar signal, and a 4th of July fireworks display? In each of these circumstances sound waves of high amplitude are present. The civil defense siren, the jet taking off, the small explosion, and the 4th of July fireworks are all loud, very loud if you are close to them. You may not be able to hear directly with your ears a thermoacoustic engine, or a hyperthermia treatment, or the sound of a parametric array. But each of these cases is analogously loud, involving the same physical processes as the loud sound waves outdoors.

This dissertation presents a method for calculating numerically how the sound from loud sources propagates through an acoustic medium. The specific problem addressed in this work is the propagation of blast noise in a homogeneous atmosphere near hard and porous ground surfaces. To verify the computer model developed for blast sounds, the sound of an electric spark pulse propagating in the free field and near hard surfaces is also examined in detail. The spark problem occurs on a scale measured in centimeters, and the blast noise occurs over distances measured in many meters, but again the physical problems in the two situations are nearly identical. The only difference between the two is that the amount of attenuation in the air is greater for sparks.

The measurement and characterization of the impulse noise from blasts are critical to the prediction of the environmental impacts of military operations. One must take measurements close enough to a source to eliminate meteorological variations but far enough away that finite amplitude wave effects do not dominate. In most cases this restriction implies that one must make these measurements over natural outdoor surfaces. The effects of the finite impedance of the ground on the propagation of linear continuous waves are profound, and this fact is widely accepted.

The techniques for predicting sound propagation outdoors, using the infinitesimal pressure amplitude assumption, linear acoustic methods, are well established. The fast field program (the FFP) and the parabolic equation method (the PE) are currently the most prevalent computational approaches using the linear theory.[1-6] These methods, however, do not accurately model the physics when the sounds become very loud, over 150 dB referenced to 20 μPa, and the amplitudes of the pressure variations making up the sound become finite instead of infinitesimal.

This dissertation develops a numerical model to predict sound propagation at high acoustic amplitudes where the infinitesimal theory breaks down. The model will include the contributions of geometrical spreading, ground effects, attenuation, and nonlinear distortion to blast pulse propagation. With this model it will be possible to make predictions for how far a receiver should be from a blast of a certain charge size for the infinitesimal acoustic propagation theory to be considered valid. This knowledge will allow measurements to be made as close to blast sources as

possible to minimize meteorological effects but far enough away that nonlinear acoustical effects will not dominate.

The remainder of this thesis is divided into chapters. The next five chapters will present the background for the physical problem and detail the equations which describe it. Chapter 2 will review some of the other methods researchers are using to explore nonlinear acoustics and some of the fundamentals governing finite amplitude waves assuming some knowledge of linear acoustic theory. Chapter 3 will review some of the considerations involved in outdoor sound propagation, especially the effect of ground impedance. Chapter 4 will detail the finite amplitude equations for a fluid such as air and will manipulate these equations into a form suitable for a numerical solution. Chapter 5 specifies a low frequency phenomenological model for a porous ground surface. The initial conditions appropriate for blasts and spark pulses are described in Chapter 6.

Chapters 7 through 9 give the numerical methods used to simulate the physical problem. Chapter 7 presents the finite difference procedures employed for the air propagation numerical solution and some motivation as to why the method was chosen. Chapter 8 describes the numerical absorbing boundary conditions used to truncate the physical domain of the atmosphere for simulation on a computer with finite memory. The numerical solution found for the porous medium ground surface is in Chapter 9.

Chapter 10 gives examples to show that the numerical simulation method is operating correctly. Here, electric spark free field propagation, normal reflection, and oblique reflection from hard surfaces are investigated in detail. This chapter

also discusses the values of artificial viscosity needed for the blast wave propagation runs.

Chapter 11 presents the results of the numerical simulations for blast waves propagating over the hard and porous medium surfaces, both for oblique and near grazing geometries. Chapter 12 concludes the main body of this thesis and points to possible future work using and extending the methods given here. Appendix A applies finite amplitude acoustic propagation outdoors as addressed in this dissertation to music, specifically to performances of Tchaikovsky's *Overture 1812* with cannons. Appendix B describes the computer program **mcnalp** developed for the numerical simulations.

2. AN INTRODUCTION TO NONLINEAR ACOUSTICS

The theory of finite amplitude sound waves, or nonlinear acoustics, is a well understood subject. Several recent books have been written on the topic, or have chapters devoted to it as well as summary articles in journals.[7-10] These references can provide a history of the subject, which will not be detailed here. The following paragraphs review some of the results of this theory.

Sound waves are dilatational, or longitudinal, waves which propagate in compressible fluids and solids. If there is nothing to compress, as in vacuum, there can be no sound. The equations

$$\frac{\partial \rho}{\partial t} + \nabla \cdot (\rho \mathbf{u}) = 0 \tag{2.1}$$

$$\rho[\frac{\partial \mathbf{u}}{\partial t} + (\mathbf{u} \cdot \nabla)\mathbf{u}] + \nabla p = 0 \tag{2.2}$$

$$p = p(\rho) \tag{2.3}$$

characterize compressible fluids where p is the total pressure of the fluid, $\mathbf{u}$ is a fluid particle velocity vector, and ρ is the total density of the fluid. Equation (2.1) is a mass conservation equation, (2.2) is a lossless Navier-Stokes force equation, and (2.3) is an equation of state. One may add additional terms to these equations, or additional equations coupled to them, to account for viscous, heat conduction, or molecular relaxation loss effects.

Usually, in acoustics, the total variables p and ρ do not change very much around their ambient values p_o and ρ_o, and $\mathbf{u}$ is assumed to have an ambient value of zero, so one may insert the substitutions $\rho = \rho_o + \rho'$ and $p = p_o + p'$ into the

first two of the above equations to obtain

$$\frac{\partial(\rho_o + \rho')}{\partial t} + \nabla\cdot[(\rho_o + \rho')\mathbf{u}] = 0 \tag{2.4}$$

$$(\rho_o + \rho')[\frac{\partial \mathbf{u}}{\partial t} + (\mathbf{u}\cdot\nabla)\mathbf{u}] + \nabla(p_o + p') = 0 \tag{2.5}$$

where ρ' and p' are the deviations of the density and pressure, respectively, from their ambient values. Further, one can expand the equation of state (2.3) in a Taylor's series[11]

$$p = p_o + As + \frac{B}{2!}s^2 + \frac{C}{3!}s^3 + \ldots \tag{2.6}$$

where the condensation $s = (\rho - \rho_o)/\rho_o = \rho'/\rho_o$.

The linear acoustic approximation neglects any terms which contain more that one acoustic variable or its derivative, or power higher than one. If one denotes the variables $\mathbf{u}$, ρ', and p' as the acoustic variables and keeps only the first-order linear terms, the linear acoustic equations result

$$\frac{\partial \rho'}{\partial t} + \rho_o \nabla\cdot\mathbf{u} = 0 \tag{2.7}$$

$$\rho_o \frac{\partial \mathbf{u}}{\partial t} + \nabla p' = 0 \tag{2.8}$$

$$p' = c_o^2 \rho' \tag{2.9}$$

where c_o is the speed of sound coming out of the first term, A, of the Taylor's series expansion of the equation of state. Here, constant ρ_o and p_o in time and space are assumed. One can solve these equations simply by combining them into a wave equation in one of the three variables, for example, the acoustic pressure wave equation,

$$\left(\frac{\partial^2}{\partial t^2} - c_o^2 \nabla^2\right) p' = 0 \,. \tag{2.10}$$

Typically, one then Fourier transforms away the time dependence of these equations to obtain the Helmholtz equation

$$\left(\nabla^2 + k^2\right) p' = 0 \tag{2.11}$$

where k is the wavenumber equal to ω/c_o, and ω is the radian frequency.

This Helmholtz equation is the basis for most linear acoustic propagation programs such as the PE and the FFP. The accuracy of these programs in modeling the physics of the fluid depend, therefore, on how well the linear acoustic approximation made in the last paragraph holds up. If any of the neglected terms in fact become significant compared to the linear terms which were kept, the linear acoustic model will break down.

Table 2.1, for example, lists the ratio of ρ' to ρ_o for various sound pressure levels, referenced ω 20 μPa. The abbreviation SPL for sound pressure level will be used throughout this thesis. In Table 2.1 it is assumed that c_o = 343 m/sec and ρ_o = 1.21 kg/m^3, values appropriate for air. It is clear that for an SPL lower than

Table 2.1. Ratio of acoustic and ambient densities versus SPL.

SPL, dB	ρ'/ρ_o
60	1.4×10^{-7}
80	1.4×10^{-6}
100	1.4×10^{-5}
120	1.4×10^{-4}
140	0.0014
160	0.014
180	0.14

120 dB, ρ' is negligible compared to ρ_0, but for a higher SPL, especially above 160 dB, ρ' is significant compared to ρ_0.

Nonlinearity is a cumulative process.[12] A distortion of 1/1000 does not seem appreciable over one wavelength, but will manifest itself as a serious distortion in 1000 wavelengths.

To see that nonlinearity is cumulative, look at one of the simplest nonlinear acoustic equations. The one-directional version of the linear wave equation (2.10) in one dimension is

$$\frac{\partial p'}{\partial t} + c_0 \frac{\partial p'}{\partial x} = 0 . \tag{2.12}$$

This equation represents a plane wave moving in the $+x$ direction. If the second-order nonlinear terms but none higher are included, the equation becomes

$$\frac{\partial p'}{\partial t} + c_0 \left(1 + \beta \frac{p'}{\rho_0 c_0^2}\right) \frac{\partial p'}{\partial x} = 0 . \tag{2.13}$$

The plane wave now travels at a speed $c_0 \left(1 + \beta \frac{p'}{\rho_0 c_0^2}\right)$ instead of c_0, and this speed is dependent on the amplitude of the wave. Therefore, the different parts of the wave will propagate at different speeds and, over long distances, the nonlinear effect can severely distort the wave even though the effect is small over short distances.

The constant β is the parameter of nonlinearity and it contains two types of nonlinearity in its equation $\beta = 1 + B/2A$. The 1 comes from the convection effect of an acoustic particle traveling at the speed $c_0 + |\mathbf{u}|$ instead of c_0. The B/A term comes from the second-order term in the nonlinear equation of state (2.6). Typical

values of B/A are 0.4 and 5.0 for air and water, respectively, so β is about 1.2 and 3.5. Theories using β account only for plane wave nonlinear effects, as there are other second-order nonlinear terms β does not include. Nevertheless, researchers have extended the use of β to the approximate cases of spherical waves and cylindrical waves.

In the 1960s Blackstock developed a theory of finite amplitude sound that could predict three distances to describe the various stages of weak nonlinear propagation.[13, 14] For an initially sinusoidal wave Blackstock called the distance in which the wave would develop its first discontinuity the discontinuity distance. Later, when the wave fully developed a shock, this larger distance was called the shock distance. Eventually, the wave would travel so far that the attenuation in the medium would begin to dominate the finite amplitude effects, and this was named the old age distance. For plane waves the discontinuity distance, $\bar{x}$, is

$$\bar{x} = \frac{1}{\beta \epsilon k} \tag{2.14}$$

where ϵ is the acoustic Mach number $|\mathbf{u}|/c_o$ and k is the wavenumber. For the approximate case of divergent spherical waves, however, the discontinuity distance $\bar{r}$ is

$$\bar{r} = r_o e^{\frac{1}{\beta \epsilon k r_o}} \tag{2.15}$$

where $\bar{r}$ is the range from the center of curvature, and r_o is the effective radius of the spherical source. The plane wave result is valid under the assumption that the old age distance $x_{\max} >> \bar{x}$ where

$$x_{\max} = \frac{1}{\alpha} - \frac{1}{\beta\epsilon k}, \tag{2.16}$$

and where the spherical wave old age distance $r_{\max} >> \bar{r}$ where $r_{\max}$ is given by the transcendental relation

$$r_{\max} = \frac{\beta\epsilon k r_o}{\alpha\left[1 + \beta\epsilon k r_o \ln(r_{\max}/r_o)\right]}. \tag{2.17}$$

Here α is the plane wave absorption coefficient in Nepers/m.

The equations for discontinuity and old age distance can be used to judge how far away from its source an initially sinusoidal finite amplitude wave might be considered linear again, exactly for the plane wave case, and approximately for the spherical wave case. Table 2.2 gives $\bar{x}$ as a function of peak pressure amplitude and frequency for air and similarly Table 2.3 for $\bar{r}$ and $r_{\max}$. The $x_{\max}$ and $r_{\max}$ values

Table 2.2. $\bar{x}$ for peak pressure amplitudes and frequencies.

SPL, dB	$\bar{x}$, 10 Hz	$\bar{x}$, 100 Hz	$\bar{x}$, 1000 Hz
120	32.4 km	3.24 km	324 m
140	3.24 km	324 m	32.4 m
160	324 m	32.4 m	3.24 m
180	32.4 m	3.24 m	0.324 m

Table 2.3. $\bar{r}$ and $r_{\max}$ for peak pressure amplitudes and frequencies.

SPL, dB at r_o = 1 m	$\bar{r}$, 100 Hz $r_{\max}$, 100 Hz $\alpha \approx 5\times10^{-5}$	$\bar{r}$, 200 Hz $r_{\max}$, 200 Hz $\alpha \approx 1.5\times10^{-4}$	$\bar{r}$, 500 Hz $r_{\max}$, 500 Hz $\alpha \approx 5\times10^{-4}$	$\bar{r}$, 1000 Hz $r_{\max}$, 1000 Hz $\alpha \approx 8\times10^{-4}$
160	$r_{\max} < \bar{r}$	$r_{\max} < \bar{r}$	$r_{\max} < \bar{r}$	25.4 m 151.4 m
170	$r_{\max} < \bar{r}$	167.0 m 580.5 m	7.75 m 262.5 m	2.0 m 198.0 m
180	25.4 m 1857 m	5.05 m 802.5 m	1.91 m 312.8 m	1.38 m 218.8 m

were calculated using values of α appropriate for the frequencies involved, and the values of r_{max} were found using an iterative computer program. Muir and Carstensen have stated that shocks will not develop if $r_{max} < \bar{r}$ so Table 2.3 does not give numerical values for these cases. For each frequency and SPL x_{max} was always greater than the values of $\bar{x}$ given in Table 2.2.

From these tables it is apparent that the discontinuity distance decreases as the frequency or the SPL increases. It is also clear that the discontinuity distances for spherical waves are greater than for plane waves. For example, at 160 dB SPL and 1000 Hz, $\bar{x}$ is 3.24 m, but $\bar{r}$ is 25.4 m. It makes sense that the discontinuity distance is greater for the spherical case, since the amplitude of a spherical wave falls off as $1/r$ while the amplitude of a plane wave changes only slightly when propagating. Unfortunately, these results are valid only for sinusoids and are approximate for the cylindrical and spherical wave cases.

A model that includes both the parameter of nonlinearity β and absorption has become known as Burgers' equation. This equation can model both pulses and sinusoids and may be derived from the form

$$\frac{\partial p'}{\partial t} + c_o \left[1 + \beta \frac{p'}{\rho_o c_o^2}\right] \frac{\partial p'}{\partial x} = \delta \frac{\partial^2 p'}{\partial t^2} \tag{2.18}$$

where

$$\delta = \frac{\mu}{2\rho_o} \left[\frac{4}{3} + \frac{\mu_B}{\mu} + \frac{(\gamma - 1)\kappa}{c_p \mu}\right] \tag{2.19}$$

accounts for the classical and bulk relaxational dissipative processes. Note that the only difference between Equations (2.13) and (2.18) is the right-hand side. Here, μ

is the shear viscosity coefficient, μ_B is a bulk viscosity coefficient, γ is the ratio of specific heats, κ is the thermal conductivity, and c_p is the coefficient of specific heat at constant pressure. Burgers' equation is often written as

$$u_t + \beta u u_{x'} = \delta u_{x'x'} \tag{2.20}$$

where the plane wave particle velocity $u = p'/\rho_o c_o$ has been substituted into Equation (2.19) with the change of variable $x' = t - x/c_o$. Much research has been done using Burgers' equations.[15-17]

Trivett and Van Buren solved a Burgers' type equation numerically via a coupled Fourier series analysis for plane, cylindrical, and spherical waves.[18,19] A recent addition to the study of Burgers' equation is given by Mitome.[20] However, at the time of these studies it was not clear how molecular relaxation effects could be added to the model, as it is today.[21] Hence, another method of computation using the parameter of nonlinearity β arose, called the Pestorius algorithm.

The Pestorius algorithm incorporates the competitive effects of absorption and finite amplitude nonlinearity by assuming the two processes are independent over small steps in range.[22-24] A small step in range is taken in the time domain accounting for nonlinear steepening. Then a fast Fourier transform is taken to the frequency domain where losses are accounted for over the range step. Then an inverse fast Fourier transform returns the wave to the time domain, and the process continues. The iteration repeats until the modeled waves have propagated as far as is necessary. Researchers have used this method successfully for the prediction of shock wave rise times from sonic booms, ballistic waves, blasts and electric spark

pulses.[25-27] It has been applied exactly to plane wave propagation and approximately to cylindrical and spherical waves since it employs the plane wave parameter of nonlinearity β.

Another method based on the parameter of nonlinearity β is the NPE, which stands for nonlinear parabolic equation.[28] This technique is similar to the standard parabolic equation, but contains the plane wave nonlinear steepening effects in addition to the effects of refraction and diffraction. Here, one steps the equations in the time domain in a particular direction.

Aanonsen *et al.* have introduced a similar one way wave solution,[29-31] this time including all the second-order nonlinear effects coming from the compressible fluid equations, not just those associated with β. These authors solve this parabolic type equation numerically using an implicit finite difference solution of a frequency coupled Fourier series expansion, not unlike the method of Trivett and Van Buren.

The Aanonsen *et al.* work seems most promising, but like the NPE, the Pestorius algorithm, and Burgers' equation methods, it can model only waves which are propagating primarily in one direction. These methods are not sufficient to model the propagation of sound outdoors, near ground surfaces which reflect sound. Reflected waves are not accounted for in the above theories.

In addition, only the Aanonsen method accounts for all the second-order nonlinearities of the compressible fluid equations. The second-order nonlinearities not associated with β are important in the near field of a blast source, for example, since the waves here are far from planar. Second-order terms are also important

when direct and reflected waves interact, near a surface or near a turning point in a refractive atmosphere. Chapter 4 will give a model to include all the second-order nonlinear effects and both incoming and outgoing waves simultaneously.

3. SOUND PROPAGATION OUTDOORS

This chapter reviews the keys to the modeling of sound propagation outdoors. Much of this material has appeared as summary articles in the literature[32-34] and is widely accepted. Other than geometrical spreading, the primary mechanisms which can influence the prediction of sound levels over flat, featureless surfaces are absorption, ground impedance, refraction, and turbulence.

The best understood aspect of sound propagation in the free field is the absorption and transference of energy as an acoustic wave moves. The primary processes are viscous and heat conduction effects, and molecular relaxational effects. The classical effects were discovered in the 1800s, whereas the understanding of relaxation has become clear only in the last 25 years. This thesis will not detail either of these processes, as a number of standard textbooks describe the particulars of the mechanisms.[35,36]

The theory to account for the influence of an outdoor ground surface is well understood also, if the impedance Z of the ground is known. Two of the better journal articles which review the important aspects of the development of this theory are listed in the references,[37,38] although the latter has innumerable misprints. Unfortunately this has been a problem in the literature of propagation near finite acoustical impedance boundaries,[39] the difficulty often being that some authors use the $e^{i\omega t}$ notation and others $e^{-i\omega t}$. In addition, Nobile and Hayek recently have found an exact solution for sound propagating in a homogeneous atmosphere with arbitrary impedance Z that is easily implemented in a computer pro-

gram.[40] Such a program will be used in Chapter 11 to examine what peak levels result in the linear acoustic limit for certain frequencies and impedances, for comparison with the nonlinear predictions described there.

The problem, however, is that researchers have had difficulty accurately ascribing surface impedances to particular ground surfaces. Numerous models have been published in the literature to relate the physical properties of the ground to Z as a function of frequency. One of the more frequently cited theories is provided by Chessel, based on the work of Delany and Bazley.[41] In this formulation the ground is characterized by a static flow resistance, a measure of how easily air moves through a ground sample. The Delany-Bazley-Chessel theory is simple and is commonly in use in most modern outdoor acoustic propagation programs such as the FFP (fast field program) and the PE (parabolic equation method). Another more complex model of natural outdoor surfaces is the four parameter model of Attenborough. This theory includes a second physically intuitive parameter in addition to the flow resistance, called the porosity. The porosity is the volume fraction of air in a ground sample. In addition to porosity and flow resistance, Attenborough adds two more parameters, the tortuosity and the pore shape factor ratio.[42] The tortuosity is a measure of how tortuous or twisty the pores of the ground are, and the shape factor ratio gives some measure of the pores' cross-sectional shape relative to a square or a circle.

It will become clear in Chapter 4 that the second-order nonlinear equation of the air can be formulated only in the time domain. All of the above cited ground

models, on the other hand, are in terms of the impedance Z in the frequency domain. Thus, an efficient solution to the outdoor propagation problem will require a formulation of the ground in the time domain. Morse and Ingard have described such a model for propagation in a porous medium.[43] In addition, Attenborough has related this theory to a low frequency model of the ground. Chapter 5 will elaborate on this model in detail.

Morse and Ingard's equations do not include the effects of nonlinearities in a porous ground, however. Little work has been performed on this topic. One exception has been the research by Kuntz, Nelson, and Blackstock.[44,45] These gentlemen investigated the effects of nonlinear propagation in batted Kevlar, a strong fibrous material. Their results showed that the nonlinearity in porous propagation is associated with the flow resistivity and is not similar to the nonlinearity in air. Hersh also developed a model for the acoustic properties of materials such as Kevlar.[46] Wilson, McIntosh, and Lambert have extended some of the knowledge in this area,[47] but more research is needed. Note that the porous model employed in Chapter 5 is a linear model.

Another major factor in predicting the propagation of sound outdoors is refraction in the atmosphere. Because of the heating and cooling of the ground and because of the effect of wind, the speed of sound in the air varies as a function of height, distance, direction, and time. Simple refraction models have been incorporated into programs such as the FFP and the PE to estimate the combined effects of ground impedance and refraction.

Random inhomogeneities in the air, called turbulence, also affect the propagation of sound outdoors.[48,49] This phenomenon is particularly important for long ranges, because the weak scattering of acoustical energy by turbulence can accumulate over distance. The uncertainty of turbulence effects renders all acoustic propagation prediction programs approximate, and more research is needed on this topic. Some recent simulation results and references to the literature may be found in McBride.[50]

This dissertation later develops a model which at present accounts for neither refraction nor turbulence. Refraction should be no problem to add at a later date, as long as one rederives the equations in the next chapter under the assumption that ρ_o and c_o, the ambient density and speed of sound, are functions of space. There should be no need to regard them as functions of time since they change negligibly during the passage of a sound wave. One might implement turbulence as a perturbation on the variables ρ_o and c_o as functions of space, making many runs with many different perturbations to give some statistical average propagation results.

4. THE TIME DOMAIN AIR PROPAGATION EQUATIONS

This chapter presents the equations to describe lossy, weakly nonlinear sound propagation in air. The equations include both of the classical dissipation effects, the effect of a bulk viscosity, and all of the second-order nonlinear terms from the compressible fluid equations. The expressions do not include relaxation effects. The equations are[51-53]

$$\frac{\partial \rho'}{\partial t} + \rho_o \nabla \cdot \mathbf{u} = -\rho' \nabla \cdot \mathbf{u} - \mathbf{u} \cdot \nabla \rho' \tag{4.1}$$

$$\rho_o \frac{\partial \mathbf{u}}{\partial t} + \nabla p = -\rho' \frac{\partial \mathbf{u}}{\partial t} - \rho_o \mathbf{u} \cdot \nabla \mathbf{u} + (\frac{1}{3}\mu + \mu_B)\nabla(\nabla \cdot \mathbf{u}) + \mu \nabla^2 \mathbf{u} \tag{4.2}$$

$$\rho_o T_o \frac{\partial s_{fr}}{\partial t} = \kappa \nabla^2 T' \tag{4.3}$$

$$p - c_o^2 \rho' = \frac{c_o^2}{\rho_o} \frac{B}{2A} \rho'^2 + c_o^2 \left(\frac{\rho \beta T}{c_p} \right)_o s_{fr} \tag{4.4}$$

$$T' - \left(\frac{T\beta}{\rho c_p} \right)_o p = \left(\frac{T}{c_p} \right)_o s_{fr} \, . \tag{4.5}$$

The variables introduced in Chapter 2 are used in these equations, except for p, which now represents the acoustic pressure deviation instead of the total pressure. In Chapter 2 p' denoted the acoustic pressure. Again, these equations assume ρ_o and p_o are constants in time and space.

The newly introduced variables are the following: T', the acoustic temperature deviation; s_{fr}, the acoustic entropy deviation with vibrational degrees of freedom frozen; T_o, the ambient temperature; B/A, the ratio of the first two terms of the Taylor's series expansion of total pressure in terms of ρ'; and β, the coefficient of thermal expansion. Note that in the rest of this thesis β does not represent the

parameter of nonlinearity as it did in Chapter 2. For ideal gases, $\beta T_o = 1$. The Equations (4.1) to (4.5) use the notation of Pierce, with the second-order nonlinear terms of Hamilton and Blackstock.

To clarify the above equations, one can write them as

$$\frac{\partial \rho'}{\partial t} + \rho_o \nabla \cdot \mathbf{u} = N1 \tag{4.6}$$

$$\rho_o \frac{\partial \mathbf{u}}{\partial t} + \nabla p = N2 + D1 \tag{4.7}$$

$$\rho_o T_o \frac{\partial s_{fr}}{\partial t} = D2 \tag{4.8}$$

$$p - c_o^2 \rho' = N3 + D3 \tag{4.9}$$

$$T' - \left[\frac{T\beta}{\rho c_p}\right]_o p = D4 \tag{4.10}$$

where

$$N1 = -\rho' \nabla \cdot \mathbf{u} - \mathbf{u} \cdot \nabla \rho' \tag{4.11}$$

$$N2 = -\rho' \frac{\partial \mathbf{u}}{\partial t} - \rho_o \mathbf{u} \cdot \nabla \mathbf{u} \tag{4.12}$$

$$N3 = \frac{c_o^2}{\rho_o} \frac{B}{2A} \rho'^2 \tag{4.13}$$

$$D1 = (\frac{1}{3}\mu + \mu_B) \nabla (\nabla \cdot \mathbf{u}) + \mu \nabla^2 \mathbf{u} \tag{4.14}$$

$$D2 = \kappa \nabla^2 T' \tag{4.15}$$

$$D3 = c_o^2 \left[\frac{\rho \beta T}{c_p}\right]_o s_{fr} \tag{4.16}$$

$$D4 = \left[\frac{T}{c_p}\right]_o s_{fr} \, . \tag{4.17}$$

Equations (4.6) to (4.10) give the linear lossless terms explicitly. The nonlinear

terms begin with the letter N in (4.11) - (4.13), and the dissipative terms begin with the letter D in (4.14) - (4.17). If $N1$, $N2$, and $N3 \rightarrow 0$, Equations (4.6) - (4.10) become linear and, similarly, if $D1$, $D2$, $D3$, and $D4 \rightarrow 0$, (4.6) - (4.10) become lossless.

By examining the terms $N1$, $N2$, and $N3$, one may see that each of these terms is indeed second-order. They are each made of the sums or differences of two acoustic quantities or their derivatives multiplying each other. In the case of $N3$ the acoustic density deviation is multiplied by itself to give ρ'^2. Note that there are no higher-order quantities such as the product of three acoustic variables or their derivatives.

Since these terms contain products of acoustic variables, it is impossible to Fourier transform Equations (4.6) to (4.10) without introducing convolution, a computationally expensive process. This circumstance is not unique to the lossy nonlinear acoustic equations employed here, but is a mathematical reality for any set of nonlinear partial differential equations. Hence this research has centered on time domain solutions.

To make a time domain solution possible it is necessary that each of the Equations (4.6) - (4.10) have no more than one time derivative present. The only offender is (4.7) which has two. Here, the time derivative term $\rho_o \frac{\partial \mathbf{u}}{\partial t}$ must be present regardless of the amplitude of the wave. But since the term $\rho' \frac{\partial \mathbf{u}}{\partial t}$ in $N2$ is not present in the linear limit, one can eliminate this time derivative as follows:

$$
\begin{aligned}
N2 &= -\rho' \frac{\partial \mathbf{u}}{\partial t} - \rho_o \mathbf{u}\cdot\nabla \mathbf{u} \\
&= -\rho' \left(\frac{-\nabla p}{\rho_o} \right) - \rho_o \mathbf{u}\cdot\nabla \mathbf{u} \\
&= \frac{\rho'}{\rho_o} \nabla p - \rho_o \mathbf{u}\cdot\nabla \mathbf{u} .
\end{aligned}
\tag{4.18}
$$

Here, the linear lossless portion of (4.7) has been substituted into the term $N2$ itself. Note that the new form of $N2$ is still of second-order.

Before a particular geometry is specified, the following assumption should be understood. Equations (4.1) - (4.5), or equivalently (4.6) - (4.18), implicitly assume that the interaction effects of dissipation and second-order nonlinearity are small. If one were to include such effects, terms would be introduced that were third-order or higher. One neglects such interaction effects to keep the equations consistently second-order.

Note that it is easy to incorporate the effects of molecular relaxation into the above equations. To include the primary relaxation processes of oxygen and nitrogen in air, Equation (4.3) becomes

$$
\rho_o T_o \frac{\partial s_{fr}}{\partial t} + \rho_o c_{v_1} \frac{\partial T_1}{\partial t} + \rho_o c_{v_2} \frac{\partial T_2}{\partial t} = \kappa \nabla^2 T' \tag{4.19}
$$

where

$$
\frac{\partial T_1}{\partial t} = \frac{T' - T_1}{\tau_1} \tag{4.20}
$$

and

$$
\frac{\partial T_2}{\partial t} = \frac{T' - T_2}{\tau_2} . \tag{4.21}
$$

The subscripts 1 and 2 denote the relaxation processes of oxygen and nitrogen, respectively. Using the notation of Pierce, T_1 and T_2 are apparent vibration temperatures, c_{v_1} and c_{v_2} are specific heats at constant volume associated with internal molecular vibrations, and τ_1 and τ_2 are relaxation times for vibrational energies. The introduction of Equations (4.19), (4.20), and (4.21) poses no additional difficulties. One merely needs to keep track of two additional variables, T_1 and T_2.

Now specialize the Equations (4.6) - (4.18) for a two-dimensional cylindrical geometry, natural for outdoor sound propagation. This thesis will use the coordinates (d, z, ϕ), as seen in Figure 4.1. Here, the variable d represents range, instead of r because this is a spherical coordinate variable, and instead of ρ because one might confuse this with a density variable.

If there are no variations with respect to the variable ϕ, i.e. $\frac{\partial}{\partial \phi} = 0$ and the ϕ component of $\mathbf{u}$ is zero, then $\mathbf{u} = u\hat{d} + v\hat{z}$ and Equations (4.6), (4.7), and (4.8) become

$$\frac{\partial \rho'}{\partial t} + \rho_o \left(\frac{\partial u}{\partial d} + \frac{u}{d} + \frac{\partial v}{\partial z} \right) = N1A \tag{4.22}$$

$$\rho_o \frac{\partial u}{\partial t} + \frac{\partial p}{\partial d} = N2A + D1A \tag{4.23}$$

$$\rho_o \frac{\partial v}{\partial t} + \frac{\partial p}{\partial z} = N2B + D1B \tag{4.24}$$

$$\rho_o T_o \frac{\partial s_{fr}}{\partial t} = D2A \tag{4.25}$$

where

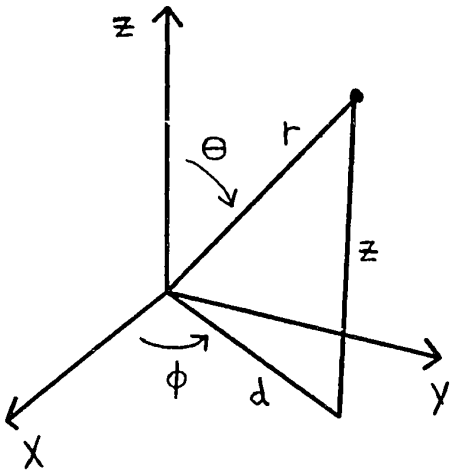

Figure 4.1. Coordinate system.

$$N1A = -\rho'\left(\frac{\partial u}{\partial d} + \frac{u}{d} + \frac{\partial v}{\partial z}\right) - u\frac{\partial \rho'}{\partial d} - v\frac{\partial \rho'}{\partial z} \tag{4.26}$$

$$N2A = \frac{\rho'}{\rho_o}\frac{\partial p}{\partial d} - \rho_o\left(u\frac{\partial u}{\partial d} + v\frac{\partial u}{\partial z}\right) \tag{4.27}$$

$$N2B = \frac{\rho'}{\rho_o}\frac{\partial p}{\partial z} - \rho_o\left(u\frac{\partial v}{\partial d} + v\frac{\partial v}{\partial z}\right) \tag{4.28}$$

and

$$\begin{aligned} D1A = &\left(\frac{1}{3}\mu + \mu_B\right)\left(\frac{\partial^2 u}{\partial d^2} + \frac{1}{d}\frac{\partial u}{\partial d} - \frac{u}{d^2} + \frac{\partial^2 v}{\partial d\,\partial z}\right) \\ &+ \mu\left(\frac{\partial^2 u}{\partial d^2} + \frac{1}{d}\frac{\partial u}{\partial d} + \frac{\partial^2 u}{\partial z^2} - \frac{u}{d^2}\right) \end{aligned} \tag{4.29}$$

$$\begin{aligned} D1B = &\left(\frac{1}{3}\mu + \mu_B\right)\left(\frac{\partial^2 u}{\partial d\,\partial z} + \frac{1}{d}\frac{\partial u}{\partial z} + \frac{\partial^2 v}{\partial z^2}\right) \\ &+ \mu\left(\frac{\partial^2 v}{\partial d^2} + \frac{1}{d}\frac{\partial v}{\partial d} + \frac{\partial^2 v}{\partial z^2}\right) \end{aligned} \tag{4.30}$$

$$D2A = \kappa\left(\frac{\partial^2 T'}{\partial d^2} + \frac{1}{d}\frac{\partial T'}{\partial d} + \frac{\partial^2 T'}{\partial z^2}\right). \tag{4.31}$$

Equation (4.22) simplifies under the assumption of a homogeneous atmosphere. For this case

$$\frac{\partial \rho_o}{\partial d} = \frac{\partial \rho_o}{\partial z} = 0\,, \tag{4.32}$$

thus

$$\frac{\partial \rho'}{\partial t} + \frac{\partial}{\partial d}\left[\left(\rho_o + \rho'\right)u\right] + \frac{\partial}{\partial z}\left[\left(\rho_o + \rho'\right)v\right] = -\left(\rho_o + \rho'\right)\frac{u}{d}\,. \tag{4.33}$$

Further, one can make rearrangements and see that the four time-dependent equations can take the forms

$$\frac{\partial \rho'}{\partial t} + \frac{\partial}{\partial d}\left[\left(\rho_o + \rho'\right)u\right] + \frac{\partial}{\partial z}\left[\left(\rho_o + \rho'\right)v\right] = N1B \tag{4.34}$$

$$\frac{\partial u}{\partial t} + \frac{\partial}{\partial d}\left[\frac{p}{\rho_o}\right] = N2C + D1C \tag{4.35}$$

$$\frac{\partial v}{\partial t} + \frac{\partial}{\partial z}\left[\frac{p}{\rho_o}\right] = N2D + D1D \tag{4.36}$$

$$\frac{\partial s_{fr}}{\partial t} = D2B \tag{4.37}$$

where

$$N1B = -\left(\rho_o + \rho'\right)\frac{u}{d} \tag{4.38}$$

and $N2C = N2A/\rho_o$, $N2D = N2B/\rho_o$, $D1C = D1A/\rho_o$, $D1D = D1B/\rho_o$, and $D2B = D2A/\rho_o T_o$.

Equations (4.34) to (4.37) have been written in a special way. They are each almost written in conservation law form where the four acoustic variables ρ', u, v, and s_{fr} are the only time derivatives which occur. The terms $N1B$, $N2C$, $N2D$, $D1C$, $D1D$, and $D2B$ may be regarded as "pseudo - source" terms. Also note that when these right-hand side terms approach zero and ρ' becomes negligible compared to ρ_o, the equations accurately describe two-dimensional linear acoustics. In contrast, if one uses the full equations of computational fluid dynamics to solve a nearly linear acoustics problem, the numerical solutions are usually poor in the linear limit. Now one can write these lossy, second-order nonlinear acoustical equations as the system

$$w_t + F_d + G_z = SF + SG \tag{4.39}$$

where

$$w = \begin{bmatrix} \rho' \\ u \\ v \\ s_{fr} \end{bmatrix} \tag{4.40}$$

$$F = \begin{bmatrix} (\rho_o + \rho')u \\ \dfrac{p}{\rho_o} \\ 0 \\ 0 \end{bmatrix} \tag{4.41}$$

$$G = \begin{bmatrix} (\rho_o + \rho')v \\ 0 \\ \dfrac{p}{\rho_o} \\ 0 \end{bmatrix} \tag{4.42}$$

$$SF = \begin{bmatrix} N1B \\ N2C + D1C \\ 0 \\ D2B \end{bmatrix} \tag{4.43}$$

and

$$SG = \begin{bmatrix} 0 \\ 0 \\ N2D + D1D \\ 0 \end{bmatrix} \tag{4.44}$$

with the equations of state (4.9) and (4.10). The system (4.39) is a form solvable numerically by time stepping. Given the initial conditions of ρ', u, v, and s_{fr} over all space, these variables and p and T' are known everywhere at all future times using (4.39) and the equations of state (4.9) and (4.10). Chapter 7 will present a specific numerical solution method for (4.39).

5. THE TIME DOMAIN POROUS MEDIA EQUATIONS

This chapter examines the time domain phenomenological equations of sound propagation in a porous medium. The porous equations are compatible with the time-dependent equations of the air. The porous medium equations will be analyzed in the frequency domain to determine the surface impedance, effective sound speed, and absorption of a porous ground surface model based on the equations. Chapter 9 will describe the time domain numerical solution used for the porous medium.

Sound propagation in pores is a classical topic, which has been examined since the beginning of research in acoustics. In 1896 Lord Rayleigh devoted several sections in his book, *The Theory of Sound*, to the propagation of sound in pores and narrow tubes.[54] Rayleigh's work was based on research by Kirchhoff. The book that is probably most often cited on porous materials, however, is *Sound Absorbing Materials* by Zwikker and Kosten from 1949.[55] They extended Rayleigh's calculations in pores to acoustical absorbing materials. Zwikker and Kosten include many experimental results along with their theoretical analysis.

This chapter employs a model that is originally from Morse and Ingard's *Theoretical Acoustics*.[56] These authors model a bulk porous medium as an idealized fluid. Their model porous acoustical equations are

$$\Omega \frac{\partial \rho'}{\partial t} + \rho_o \nabla \cdot \mathbf{u} = 0 \tag{5.1}$$

$$\rho_p \frac{\partial \mathbf{u}}{\partial t} + \Phi \mathbf{u} + \nabla p' = 0 \tag{5.2}$$

$$\rho' = \kappa_p \rho_o p' \tag{5.3}$$

where Ω is the porosity, ρ' and ρ_o are the acoustic and ambient densities, $\mathbf{u}$ is the average particle velocity in the direction of propagation, ρ_p is an effective density, Φ is a flow resistance, p' is the acoustic pressure, and κ_p is the effective compressibility of the fluid in the pores. Equations (5.1), (5.2), and (5.3) are the equations of continuity, motion, and state, respectively. Note that κ_p and ρ_p should be viewed as functions of frequency. In fact, Morse and Ingard solve (5.1) - (5.3) in the frequency domain, bypassing the time dependence of these equations. Their transformations using $e^{-i\omega t}$ time dependence were

$$\rho_e = \rho_p \left(1 + \frac{i\Phi}{\rho_p \omega}\right) \tag{5.4}$$

$$c_e = \frac{1}{\sqrt{\rho_e \kappa_e}} \tag{5.5}$$

$$\kappa_e = \Omega \kappa_p \tag{5.6}$$

for an effective density, sound speed, and compressibility to obtain the Helmholtz equation

$$\nabla^2 \psi + \left(\frac{\omega}{c_e}\right)^2 \psi = 0 \tag{5.7}$$

where $\mathbf{u}$ is calculated from $\mathbf{u} = -\nabla \psi$. The impedance of such a porous material is then

$$\begin{aligned} Z &= \rho_e c_e = (\rho_e/\kappa_e)^{1/2} \\ &= (\rho_p/\kappa_p \Omega)^{1/2} (1 + i\Phi/\rho_p \omega)^{1/2} . \end{aligned} \tag{5.8}$$

Using Morse and Ingard's results, but using the $e^{i\omega t}$ time dependence, Donato com-

pared this impedance model to some averaged experimental data over a wide range of frequencies in 1977.[57] He showed that the above model was probably not as good as a model where porosity varied as a function of depth.

Attenborough has analyzed porous equations similar to those of Morse and Ingard and then related them to a low frequency model of a finite ground impedance.[58-60] His form of the generalized pore equations in one dimension are

$$\Omega \frac{\partial \rho}{\partial t} + \rho \frac{\partial u}{\partial x} = 0 \tag{5.9}$$

$$\rho_o \frac{K}{\Omega} \frac{\partial u}{\partial t} + \Phi u + \frac{\partial p}{\partial x} = 0 \tag{5.10}$$

$$c_o^2(\rho - \rho_o) = \gamma(p - p_o) \, . \tag{5.11}$$

Note that (5.9) was misprinted in Attenborough's 1983 J. Acoust. Soc. Am. paper, but appeared correctly in his 1982 Physics Reports work. These equations use a different notation than (5.1), (5.2), and (5.3). Here p represents a total pressure, with p_o the ambient pressure, and similarly for ρ and ρ_o. The constant K represents an effective density factor or structure factor. If one linearizes these equations to first-order, under the assumption $p = p_o + p'$ and $\rho = \rho_o + \rho'$, and remembers that at low frequencies[61] $\gamma \rightarrow 1$,

$$\Omega \frac{\partial \rho'}{\partial t} + \rho_o \frac{\partial u}{\partial x} = 0 \tag{5.12}$$

$$\rho_o \frac{K}{\Omega} \frac{\partial u}{\partial t} + \Phi u + \frac{\partial p'}{\partial x} = 0 \tag{5.13}$$

$$p' = c_o^2 \rho' \, . \tag{5.14}$$

These equations involve only linear variables and may be compared to Morse and Ingard's Equations (5.1) - (5.3).

To derive equations for a complex wavenumber, one eliminates ρ' and p' to obtain the governing wave equation for this porous model in the average velocity u,

$$\rho_o K \frac{\partial^2 u}{\partial t^2} + \Phi\Omega \frac{\partial u}{\partial t} - \rho_o c_o^2 \frac{\partial^2 u}{\partial^2 x} = 0 . \tag{5.15}$$

By substituting $u = e^{i(\omega t - k_x x)}$ into this equation, the plane wave dispersion relation results,

$$-\omega^2 \rho_o K + i\omega\Phi\Omega + k_x^2 \rho_o c_o^2 = 0 \tag{5.16}$$

or

$$k_x^2 = K\frac{\omega^2}{c_o^2} - i\frac{\Phi\Omega}{\rho_o c_o^2}\omega . \tag{5.17}$$

This latter form will be useful later, since the effective sound speed in the pores is $c_{\text{eff}} = \omega/Re[k_x]$ and the attenuation is $\alpha = -Im[k_x]$, i.e., $k_x = \omega/c_{\text{eff}} - i\alpha$.

In his 1983 paper Attenborough relates the structure factor K to one of the parameters of his four-parameter model of a porous medium by

$$K = \frac{4}{3}q^2 \tag{5.18}$$

where q is the tortuosity. The correspondence between the Morse and Ingard model and his four-parameter model is exact when

$$\frac{n^2}{s} = 1 \tag{5.19}$$

where n is the dynamic shape factor and s is the static shape factor. In the four-

parameter theory of this 1983 paper, $n = s = 1$ corresponds exactly to the case of perfectly circular cylindrical pores. Note that in his 1987 paper Attenborough shifts to the notation $s_p^2 = n^2 A^2/s$ where $A = 1/2$ for circular cylindrical pores, where s_p is called a pore shape factor ratio. Under the 1983 theory,[62] a typical value of q for soil is 1.5.

In the 1983 paper the impedance of the Morse and Ingard phenomenological equations is found to be

$$\frac{Z}{\rho_o c_o} = (2\gamma\Omega)^{-1/2} n(1+i)(\Phi/\rho_o s\omega)^{1/2} \tag{5.20}$$

which is independent of tortuosity. Note that the exponent of $(2\gamma\Omega)$ is misprinted in the 1983 paper itself, but (5.20) may be verified from his Equations (32), (36), and (38) under the assumption of large Φ and low ω.

For a typical outdoor mown grass surface Φ and Ω might be 300,000 mks Rayls = 300,000 kg/(s m^2) and 0.30, respectively.[63] For these values and where $\rho_o = 1.21$ kg/m^3, $\gamma \rightarrow 1$ (low frequency), and $s = n = 1$ (circular cylindrical pores)

$$\frac{Z}{\rho_o c_o} = \frac{256.44}{\sqrt{f}}(1+i)\ . \tag{5.21}$$

This is the impedance predicted from the Attenborough interpretation of the phenomenological porous model. Table 5.1 lists values of $Z/[\rho_o c_o(1+i)]$ for various frequencies, using the above constants. With these same values, one can find the speed of sound and attenuation in the pores from (5.17). Here, $k_x^2 = 25.5t, imes 10^{-6}\omega^2 - i0.632\omega$. Column three in Table 5.1 gives values of the

Table 5.1. Porous model impedance, sound speed, and absorption.

f, Hz	$Z/\rho_o c_o(1+i)$	$c_{\text{eff}} = \omega/Re[k_x]$, m/s	$\alpha = -Im[k_x]$, Np/m
500	11.468	93.61	29.58
400	12.82	84.79	26.79
300	14.80	74.35	23.5
200	18.13	61.48	19.43
100	25.64	44.03	13.91
75	29.61	38.25	12.08
50	36.26	31.35	9.90
25	51.28	22.25	7.02
10	81.09	14.08	4.45
5	114.68	9.97	3.14

effective sound speed in the pores, and column four gives the attenuation coefficient for the listed frequencies.

Notice that as the frequency decreases, the magnitude of impedance increases, the effective sound speed decreases, and the attenuation decreases. Also note that below 50 Hz c_{eff} is less than 1/10th the speed of sound in air, $c_o = 343$ m/s. This fact supports the hypothesis that the porous medium is locally reacting, i.e., plane waves in air incident on the porous surface at significant angles of incidence from normal will propagate into the pores normal to the surface. If the surface were not locally reacting, waves incident on one part of the surface would affect the waves propagating on nearby parts of the surface. Local reaction implies that each part of a porous surface is independent of all others. This concept is useful and will be used in Chapter 9.

Because the reactance of the impedance, the imaginary part of Z, is equal to the resistance, the real part of Z in Equation (5.20), surface waves should not develop for propagation over this porous medium. Surface waves are independent

propagating waves at the interface of the air and porous medium which can sometimes develop depending on whether the reactance of the impedance is greater than the resistance. Surface waves have been studied in great detail, and are reasonably well understood.[64-68] For a spherical source they propagate along the ground with a $r^{-1/2}$ dependence and decrease exponentially with height. Because these waves decrease with distance as $r^{-1/2}$, their contribution to the total sound field can be significant at medium ranges since the rest of sound field components fall off as $1/r$. Surface waves are different from the "ground waves" of AM radio propagation, and one may obtain a more complete discussion on surface waves in the references.

6. MODEL INITIAL CONDITIONS IN AIR

This chapter presents the initial conditions for both blast waves and spark pulses used in the numerical simulations given in Chapters 10 and 11. Blasts are discussed first, and then sparks. Scaling law theory is also discussed with reference to the blast initial conditions. This chapter closes describing how the initial conditions were implemented near surfaces.

6.1 Blast Initial Conditions and Scaling Laws

The pulse shape originally used in this investigation was the ideal blast pulse of Reed.[69] The shape closely approximates the pressure waveforms emitted both by electric sparks and by explosions, on different scales. Reed's pulse is

$$p(t) = \Delta p_o \left[1 - \frac{t}{t_+}\right]\left[1 - \frac{t}{\tau}\right]\left[1 - \left(\frac{t}{\tau}\right)^2\right] \tag{6.1}$$

for $0 \leq t \leq \tau$ and $p(t) = 0$ otherwise. The constant Δp_o is the peak pressure of the pulse, τ is the waveform duration, and t_+ is the length of the positive phase, when $p(t) > 0$.

One problem with this idealization for numerical computations is that it has a discontinuity at $t = 0$, where it jumps from $p(0^-) = 0$ to $p(0^+) = \Delta p_o$. To eliminate this discontinuity, which contains much high frequency energy, a modified Reed pulse was developed. It has the wave shape of (6.1), with a raised cosine introduction so that at no point in the pulse is $p(t)$ or $p'(t)$ discontinuous. The expression for this pulse is

$$p(t) = \begin{cases} p_1(t), & 0 \le t \le t_3 \\ p_2(t), & t_3 \le t \le t_2+\tau \\ 0, & \text{otherwise} \end{cases} \tag{6.2}$$

where

$$p_1(t) = \frac{\Delta p_o}{2}\left[1 - \cos\frac{\pi\, t}{t_1}\right] \tag{6.3}$$

and

$$p_2(t) = \Delta p_o \left[1 - \frac{t - t_2}{t_+}\right]\left[1 - \frac{t - t_2}{\tau}\right]\left[1 - \left[\frac{t - t_2}{\tau}\right]^2\right]. \tag{6.4}$$

Here $t_1 < t_2 < t_3$ where t_2 is the "delay" of the original Reed pulse and where t_3 is when the two waveforms both meet

$$p_1(t) = p_2(t)\Big|_{t = t_3} \tag{6.5}$$

and their derivatives match

$$\frac{d}{dt}p_1(t) = \frac{d}{dt}p_2(t)\Big|_{t = t_3}. \tag{6.6}$$

Because this thesis considers only weak nonlinear acoustical waves, the pulse shape should be realizable in the linear acoustics limit. In this linear limit the pulse $p(t)$ additionally should balance, satisfying the conservation of impulse

$$\int_0^{t_2+\tau} p(t)\, dt = 0\,. \tag{6.7}$$

This expression means that after the pulse passes by, it should leave the compressible fluid particles in their original state.

For the blast wave case the durations τ = 0.04 s for the Reed waveform and $t_1 = 0.5\times10^{-3}$ s for the first π radians of the cosine introduction were used. These values mean the 0% to 100% rise time of the cosine introduction was approximately 1/80th the length of the rest of the pulse. This duration of τ corresponds to that observed 30 m from a 0.57 kg C-4 plastic explosive detonation.[70] The peak level for this pulse is 164.1 dB SPL at 30 m.

A computer program was written to find t_+, t_2, and t_3 to satisfy (6.5), (6.6), and (6.7) with the above given values of t_1 and τ. The values found were $t_+ = 11.0326\times10^{-3}$, $t_2 = 0.50293016\times10^{-3}$, and $t_3 = 0.50585915\times10^{-3}$ s.

The above specification, however, is only on the pressure. The system of equations (4.39) requires initial values on the four variables ρ', u, v, and s_{fr}, which imply p and T'. In this research the approximation was made that the initial conditions would be lossless and linear, under the assumption that the variable values would settle into their lossy nonlinear relationships in a few time steps.

Using this lossless linear assumption, s_{fr} was assumed zero everywhere initially. Then T' is linearly related to p from Equation (4.5). Also, in a linear approximation one can find $p = c_o^2\rho'$, and u and v from p using a potential.

For spherical pulses the radial component of particle velocity v_r is related to the pressure by the spherical potential $F(t - r/c_o)$ as

$$p = \frac{\partial}{\partial t}\frac{F(t - r/c_o)}{r} \tag{6.8}$$

and

$$v_r = \frac{p}{\rho_o c_o} + \frac{F(t - r/c_o)}{\rho_o r^2} . \tag{6.9}$$

The variables u and v are, of course, related to v_r by the geometrical expressions[71] $u = v_r \sin\theta$ and $v = v_r \cos\theta$. Thus, given p for a spherical pulse, ρ', u, v, s_{fr}, and T' can be found in a linear lossless approximation.

Corresponding to the pressure waveform (6.2) - (6.4) one can find $F(t - r/c_o)/r$ by integrating p with respect to t. The result is

$$\frac{F(\,(t - r/c_o) = t_b)}{r} = \begin{cases} \dfrac{\Delta p_o}{2}\left[t_b - \dfrac{t_1}{\pi}\sin\left(\dfrac{\pi t_b}{t_1}\right)\right], & 0 \le t_b \le t_3 \\ \dfrac{\Delta p_o}{2}\left[t_3 - \dfrac{t_1}{\pi}\sin\left(\dfrac{\pi t_3}{t_1}\right)\right] + I_1, & t_3 < t_b \le t_2 + \tau \\ 0, & \text{otherwise} \end{cases} \tag{6.10}$$

where

$$\begin{aligned} \frac{I_1}{\Delta p_o} = {} & t_b - t_3 - \left(\frac{1}{\tau} + \frac{1}{t_+}\right)\frac{(t_b - t_2)^2 - (t_3 - t_2)^2}{2} \\ & + \left(\frac{1}{\tau t_+} - \frac{1}{\tau^2}\right)\frac{(t_b - t_2)^3 - (t_3 - t_2)^3}{3} \\ & + \left(\frac{1}{\tau^3} + \frac{1}{t_+ \tau^2}\right)\frac{(t_b - t_2)^4 - (t_3 - t_2)^4}{4} \\ & - \frac{1}{\tau^3 t_+}\frac{(t_b - t_2)^5 - (t_3 - t_2)^5}{5} . \end{aligned} \tag{6.11}$$

For all the runs of Chapters 10 and 11 an approximate version of I_1 was used,

$$\frac{\text{approximate } I_1}{\Delta p_o} = t_b - t_3 - \left(\frac{1}{\tau} + \frac{1}{t_+}\right)\frac{(t_b - t_3)^2}{2} + \left(\frac{1}{\tau t_+} - \frac{1}{\tau^2}\right)\frac{(t_b - t_3)^3}{3} + \left(\frac{1}{\tau^3} + \frac{1}{t_+\tau^2}\right)\frac{(t_b - t_3)^4}{4} - \frac{1}{\tau^3 t_+}\frac{(t_b - t_3)^5}{5}. \quad (6.12)$$

For the particular values of t_1, t_2, t_3, t_+, τ used in this study, the difference between (6.11) and (6.12) is very small. Figure 6.1 plots Equation (6.10) using both Equations (6.11) and (6.12), with the former using a solid line and the latter a dashed line.

A most successful theory[72] for predicting the effects of explosions has been the scaling laws of Hopkinson from 1915. These relationships have been experimentally verified over many orders of magnitude of energy release and are very useful in an empirical sense. Scaling laws do not explicitly account for the absorption of the air or ground impedance, but instead simply state that the distance, time, and impulse of blasts scale as $E^{-1/3}$, or equivalently $W^{-1/3}$. Here E and W are the energy release and weight of an explosive, respectively.

To obtain the initial conditions at 30 m for C-4 charge sizes other than 0.57 kg, the blast durations can be found from a scaling law. The duration of the pulse from a blast with weight W should be proportional to $(W/W_o)^{1/3}$ where W_o is the reference charge weight.

Another relation,[73] more approximate and based on the observation that blast overpressures decrease with distance at a rate of about $r^{-1.2}$, can be used to predict

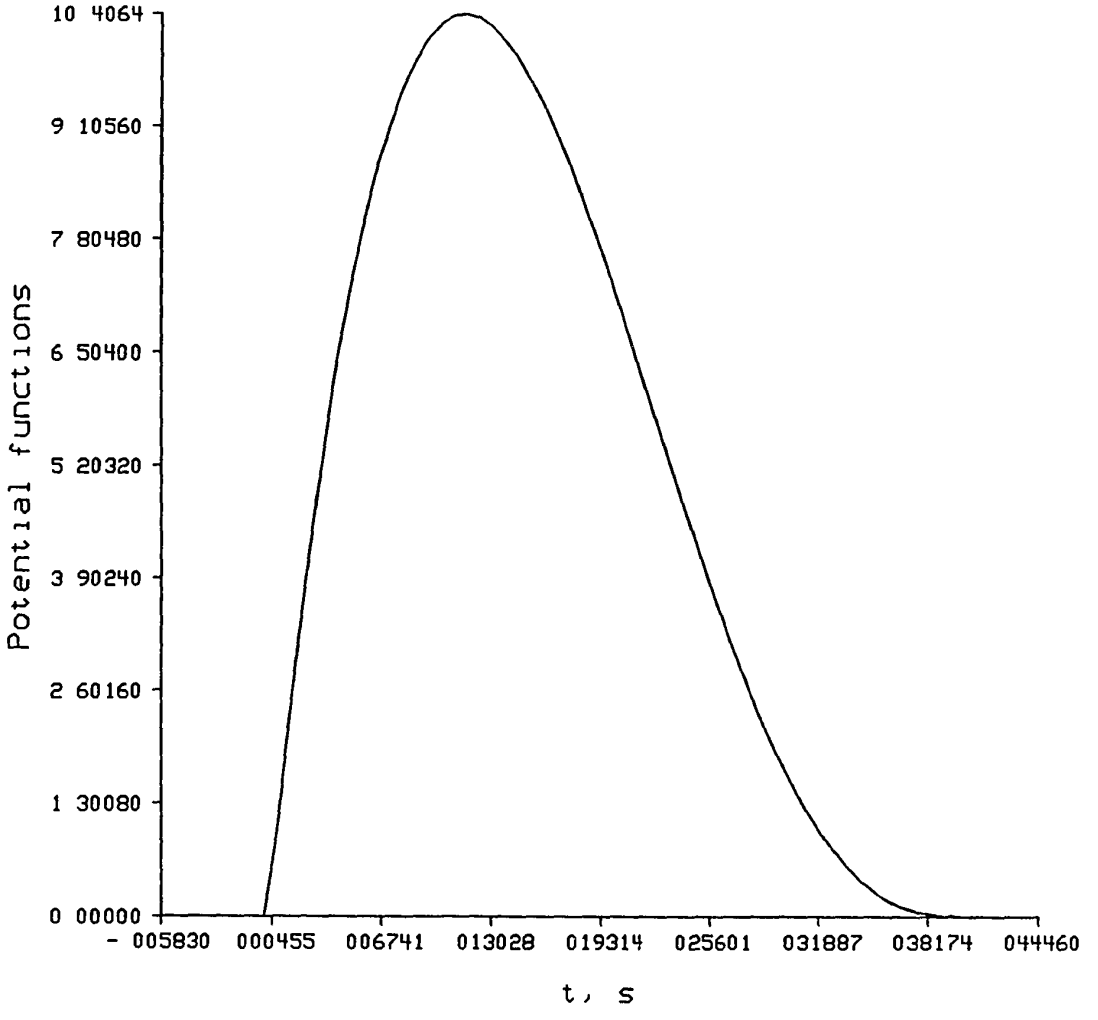

Figure 6.1. Pulse spherical potential from Equation (6.10). The solid line is for the exact I_1, the dotted line is for the approximate I_1.

initial overpressures for different size blasts at a fixed distance. If the peak pressure is known for a charge of weight W at a fixed range,[74] the expression $8\log(W/W_0)$ gives the increase in pressure in dB expected over that from a charge of weight W_0.

Using these expressions for peak pressure and pulse duration relative to the 164.1 dB data, Table 6.1 gives values of the approximate duration of the pulses τ in milliseconds and the weights W in kg, for blasts with peak sound pressure levels at 3 dB intervals. The next chapters will use these values of peak SPL and τ for the blast calculation initial conditions.

6.2 Electric Spark Initial Conditions

Because of scaling, the small explosion relative durations given in the last section are nearly the same as those seen for electric spark pulses in air. It turns out that if one divides the blast values τ, t_+, t_1, t_2, and t_3 by 1000, the wave shape is similar to that observed for an electric spark pulse. See, for example, the thesis of

Table 6.1. Scaled blast data.

SPL, dB	τ, ms	W, kg
164.1	40.	0.57
180.	183.89	55.38
177.	137.8	23.35
174.	103.4	9.84
171.	77.5	4.15
168.	58.15	1.751
165.	43.6	0.738
162.	32.7	0.311
159.	24.5	0.131
156.	18.34	0.055
153.	13.72	0.023
150.	10.32	0.0098

Anderson.[75] Here τ is approximately 40 μs. Thus, the duration values for sparks used in Chapter 10 are $\tau = 40\times10^{-6}$, $t_1 = 0.5\times10^{-6}$, $t_+ = 11.0326\times10^{-6}$, $t_2 = 0.50293016\times10^{-6}$, and $t_3 = 0.50585915\times10^{-6}$ s.

6.3 Initial Conditions near Surfaces

Chapters 10 and 11 will present propagation results including reflections from hard surfaces for sparks and hard and porous surfaces for blasts. This section describes the initial conditions used for those cases when a reflected wave initially existed in the computational domain. For simulations where an initial condition contained a reflected wave, linear superposition was used between the incident pulse and its hard surface reflection image. This starting condition is approximate, but is certainly satisfactory for the propagation decay analysis in Chapter 11.

For the high amplitudes of interest in this research, the pressure doubling seen next to a hard surface in linear acoustics should be replaced with a more accurate relation dependent on the amplitude and past history of the incident wave. Thus the starting wave contains nonphysical components. The nonphysical wave components, however, do not severely affect the overall solution down range.

This linear hard surface superposition method also was employed for the initial conditions for blast waves over a porous ground. Boundary points where the incident pulse initially intersected the ground were implemented using the hard ground boundary condition. For all distances greater than those initially touched by the incident and reflected waves, the porous medium equations coupling the air propagation equations acted as a boundary condition. See Figure 6.2. for the initial po-

sitions in space of the direct and reflected waves with respect to the implementation of the boundary conditions for this porous case.

The initial conditions described in this chapter worked well for the simulations of Chapters 10 and 11. They can be improved with additional work, but as will be seen later, the conditions were satisfactory for the modeling of finite amplitude propagation near the hard and porous ground surfaces.

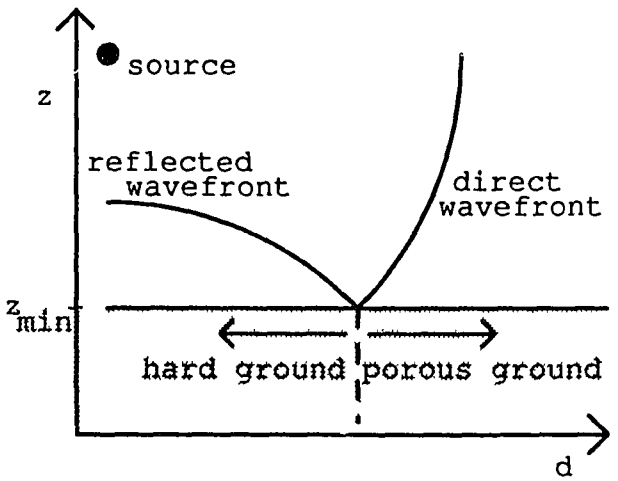

Figure 6.2. The initial condition in space for the direct and reflected waves with respect to the boundary conditions for the porous ground simulations.

7. NUMERICAL SOLUTION TO THE AIR EQUATIONS

In the second volume of his lectures on physics[76] Richard Feynman states "The *only* [sic] general methods of solution are numerical." This chapter describes the different types of numerical solutions possible for the equations given in Chapter 4 and then specifies the particular solution chosen for this thesis. This type of numerical solution should be applicable to many types of problems involving finite amplitude sound waves in fluids, not just the one addressed in this work. The properties of the techniques such as accuracy and high frequency resolution are also discussed.

7.1 Background

A finite element solution to (4.39) is possible. However, an iterative solution is required to evaluate the nonlinear terms in the system at each time step. This procedure is highly expensive from a computational point of view.[77] New methods of finite element solution to nonlinear problems are being investigated currently,[78] but it seems that finite element methods are best suited to linear equations.

Explicit finite difference methods do not have any difficulties with nonlinear equations. One can implement nonlinear terms just as easily as the linear ones with this technique. An explicit method, therefore, will be used in this research.

The application of finite differences to acoustical equations is not a recent idea. For example, an entire chapter is devoted to the finite difference solution of sound waves in Richtmyer and Morton's *Difference Methods for Initial-Value Problems.*[79] That work, however, did not consider acoustical nonlinearities. To study blast

waves with strong nonlinearities, Brode used a finite difference solution to a set of fluid dynamics equations in the 1950s.[80,81] Brode's methods were used for overpressures of 2000 atmospheres to 0.10 atmosphere and are not applicable for weaker waves, the subject of this thesis. Rao and Zumwalt in 1970 modeled the pressure history of a sonic boom.[82] Their method is not dissimilar to the one used in this thesis. Rao and Zumwalt's finite difference method is simplistic and it includes no absorption effects, but they do solve a linearized system of equations. By the early 1970s it was apparent that for weak pressure waves, the linearized compressible flow equations should be used instead of the full equations of computational fluid dynamics.[83]

In 1974 Alford et al. stated that highly accurate fourth-order finite difference algorithms gave superior results to those of lower-order for acoustic equations.[84] This "order" is meant in a slightly different sense than the second-order nonlinearities discussed earlier. In a finite difference approximation, a derivative is represented by using a finite difference expression such as

$$\psi'(x) \approx \frac{\psi(x + \Delta x) - \psi(x)}{\Delta x} \tag{7.1}$$

where Δx is a small increment in x. The "order" of a finite difference approximation is related to how accurately the derivative is modeled in a numerical sense. Here

$$\frac{\psi(x + \Delta x) - \psi(x)}{\Delta x} = \psi'(x) + C_1 \Delta x + C_2 \Delta x^2 + \ldots \tag{7.2}$$

where C_1, C_2, . . . are constants. This approximation is first-order since the approx-

imation is dominated by the term $C_1\Delta x$. Another discretization of $\psi'(x)$ is

$$\frac{\psi(x+\Delta x)-\psi(x-\Delta x)}{2\Delta x}=\psi'(x)+D_1\Delta x^2+D_2\Delta x^4+\ldots \tag{7.3}$$

which is instead dominated by the term $D_1\Delta x^2$, so this approximation is second-order. Similarly the approximation

$$\begin{aligned}&\frac{8\psi(x+\Delta x)-8\psi(x-\Delta x)-\psi(x+2\Delta x)+\psi(x-2\Delta x)}{12\Delta x}\\&=\psi'(x)+E_1\Delta x^4+\ldots\end{aligned} \tag{7.4}$$

is fourth-order. Alford *et al.* also found that these fourth-order methods would allow useful difference computations on coarse grids.

Possibly unaware of the Alford *et al.* results, Walkington and Eversman used several different second-order finite difference algorithms to compute the solution to one-dimensional shocked acoustic waves in ducts.[85,86] They found that their results agreed with the finite amplitude acoustic solution of Blackstock for an initially sinusoidal wave. One aspect of their work that is particularly interesting is their use of an artificial viscosity factor. The purpose of this artificial viscosity is to attenuate the high frequencies not well resolved by their finite difference grid. These high frequencies are generated by the finite amplitude nonlinear effects.

The most highly developed finite difference solution to nonlinear acoustic equations has been introduced by Maestrello, Bayliss and Turkel.[87-91] They used fourth-order finite difference schemes to model the two-dimensional nonlinear interaction of sound with the shear layer of a jet. The particular technique they employed was a fourth-order in space, second-order in time version of the MacCormack finite

difference method derived by Gottlieb and Turkel.[92] Because of the completeness of the work of Maestrello, Bayliss, and Turkel, the remainder of this dissertation will use many of their techniques. S. I. Hariharan also studied nonlinear acoustic propagation in air proceeding similarly to Maestrello, Bayliss, and Turkel.[93] His methods are highly mathematical and are not as straightforward as the Maestrello, Bayliss, and Turkel techniques, however, so the latter group's methods will be followed.

7.2 The Finite Difference Method

For simplicity this research uses a regular discretization in both the d and z directions. For any of the variables the notation

$$\psi(t, d, z) = \psi(n\Delta t, i\Delta x, j\Delta x) = \psi_{i,j}^{n} \tag{7.5}$$

represents discretizing in time in steps of Δt and in space in steps of Δx.

The Maestrello, Bayliss, and Turkel procedure begins by splitting Equation (4.39),

$$w_t + F_d + G_z = SF + SG \tag{7.6}$$

into the two equations

$$w_t + F_d = SF \tag{7.7}$$

and

$$w_t + G_z = SG \ . \tag{7.8}$$

One may solve each split equation straightforwardly by finite difference schemes. Call $L_d(\Delta t)$ and $L_z(\Delta t)$ finite difference solution operators which advances the solution of (7.7) and (7.8) one step, i.e., $w(t + \Delta t) = L_d(\Delta t)w(t)$ for (7.7) and

$w(t+\Delta t) = L_z(\Delta t)w(t)$ for (7.8). Then the Strang splitting method gives the solution to (7.6) as

$$w(t+2\Delta t) = L_d(\Delta t)L_z(\Delta t)L_z(\Delta t)L_d(\Delta t)w(t) \tag{7.9}$$

where both $L_d(\Delta t)$ and $L_z(\Delta t)$ have been applied twice, in a symmetrical order.[94] Splitting is not exact, but is merely another finite difference numerical approximation. The symmetry in (7.9) is necessary to keep the finite difference approximations high-order.

The operator $L_d(\Delta t)$ is given by two versions, the first of which is

$$\begin{aligned} w_i^{\tilde{n}} &= w_i^n + (\frac{\Delta t}{6\Delta x})(7F_i^n - 8F_{i+1}^n + F_{i+2}^n) + \Delta t\, SF_i^n \\ w_i^{n+1} &= \frac{1}{2}\left[w_i^n + w_i^{\tilde{n}} - (\frac{\Delta t}{6\Delta x})(7F_i^{\tilde{n}} - 8F_{i-1}^{\tilde{n}} + F_{i-2}^{\tilde{n}}) + \Delta t\, SF_i^{\tilde{n}}\right] \end{aligned} \tag{7.10}$$

which is a two-step method, fourth-order accurate in Δx and second-order accurate in Δt. Here $w^{\tilde{n}}$ denotes a temporary value in time, and $F^{\tilde{n}}$ is the value of F at that temporary time. The other version of $L_d(\Delta t)$ is

$$\begin{aligned} w_i^{\tilde{n}} &= w_i^n - (\frac{\Delta t}{6\Delta x})(7F_i^n - 8F_{i-1}^n + F_{i-2}^n) + \Delta t\, SF_i^n \\ w_i^{n+1} &= \frac{1}{2}\left[w_i^n + w_i^{\tilde{n}} + (\frac{\Delta t}{6\Delta x})(7F_i^{\tilde{n}} - 8F_{i+1}^{\tilde{n}} + F_{i+2}^{\tilde{n}}) + \Delta t\, SF_i^{\tilde{n}}\right]. \end{aligned} \tag{7.11}$$

In using $L_d(\Delta t)$, it is necessary to alternate the use of (7.10) and (7.11) to retain accuracy.[95] The operator $L_z(\Delta t)$ is similarly given in two variants

$$
\begin{aligned}
w_j^{\tilde{n}} &= w_j^n + (\frac{\Delta t}{6\Delta x})(7G_j^n - 8G_{j+1}^n + G_{j+2}^n) + \Delta t\, SG_j^n \\
w_j^{n+1} &= \frac{1}{2}\left[w_j^n + w_j^{\tilde{n}} - (\frac{\Delta t}{6\Delta x})(7G_j^{\tilde{n}} - 8G_{j-1}^{\tilde{n}} + G_{j-2}^{\tilde{n}}) + \Delta t\, SG_j^{\tilde{n}}\right]
\end{aligned}
\tag{7.12}
$$

and

$$
\begin{aligned}
w_j^{\tilde{n}} &= w_j^n - (\frac{\Delta t}{6\Delta x})(7G_j^n - 8G_{j-1}^n + G_{j-2}^n) + \Delta t\, SG_j^n \\
w_j^{n+1} &= \frac{1}{2}\left[w_j^n + w_j^{\tilde{n}} + (\frac{\Delta t}{6\Delta x})(7G_j^{\tilde{n}} - 8G_{j+1}^{\tilde{n}} + G_{j+2}^{\tilde{n}}) + \Delta t\, SG_j^{\tilde{n}}\right].
\end{aligned}
\tag{7.13}
$$

These fourth-order in Δx schemes are not applicable everywhere on a finite domain, however. The operator $L_d(\Delta t)$ needs variable values at spatial points $i-2$, $i-1$, i, $i+1$, and $i+2$ to advance from time n to $n+1$. If i runs from 1 to I, the above routines are not applicable at points 1, 2, $I-1$, and I. The points 1 and I are boundary points, and numerical boundary conditions given in Chapter 8 will advance their values from time n to time $n+1$.

For the variable values at points $i = 2$ and $i = I-1$ the second-order in Δt and Δx versions of $L_d(\Delta t)$ were used in this research. Just as with the fourth-order in Δx schemes, the second-order $L_d(\Delta t)$ has two variants

$$
\begin{aligned}
w_i^{\tilde{n}} &= w_i^n + \frac{\Delta t}{\Delta x}(F_i^n - F_{i+1}^n) + \Delta t\, SF_i^n \\
w_i^{n+1} &= \frac{1}{2}\left[w_i^n + w_i^{\tilde{n}} - \frac{\Delta t}{\Delta x}(F_i^{\tilde{n}} - F_{i-1}^{\tilde{n}}) + \Delta t\, SF_i^{\tilde{n}}\right]
\end{aligned}
\tag{7.14}
$$

and

$$
\begin{aligned}
w_i^{\tilde{n}} &= w_i^n - \frac{\Delta t}{\Delta x}(F_i^n - F_{i-1}^n) + \Delta t\, SF_i^n \\
w_i^{n+1} &= \frac{1}{2}\left[w_i^n + w_i^{\tilde{n}} + \frac{\Delta t}{\Delta x}(F_i^{\tilde{n}} - F_{i+1}^{\tilde{n}}) + \Delta t\, SF_i^{\tilde{n}}\right]
\end{aligned}
\tag{7.15}
$$

which one should alternate. Similarly at $j = 2$ and $j = J-1$ for $1 \leq j \leq J$, the second-order $L_z(\Delta t)$ schemes are

$$\begin{aligned} w_j^{\tilde{n}} &= w_j^n + \frac{\Delta t}{\Delta x}(G_j^n - G_{j+1}^n) + \Delta t\, SG_j^n \\ w_j^{n+1} &= \frac{1}{2}\left[w_j^n + w_j^{\tilde{n}} - \frac{\Delta t}{\Delta x}(G_j^{\tilde{n}} - G_{j-1}^{\tilde{n}}) + \Delta t\, SG_j^{\tilde{n}}\right] \end{aligned} \tag{7.16}$$

and

$$\begin{aligned} w_j^{\tilde{n}} &= w_j^n - \frac{\Delta t}{\Delta x}(G_j^n - G_{j-1}^n) + \Delta t\, SG_j^n \\ w_j^{n+1} &= \frac{1}{2}\left[w_j^n + w_j^{\tilde{n}} + \frac{\Delta t}{\Delta x}(G_j^{\tilde{n}} - G_{j+1}^{\tilde{n}}) + \Delta t\, SG_j^{\tilde{n}}\right]. \end{aligned} \tag{7.17}$$

In the future it might be possible to find some higher-order schemes which apply at $i = 2$ and $i = I-1$ and $j = 2$ and $j = J-1$, but the second-order schemes work well.

7.3 Phase Dispersion and Artificial Viscosity

Note the reason that the fourth-order schemes are better for wave propagation than the second-order schemes is because the former have minimal phase dispersion. The one way model equation $\frac{\partial p}{\partial t} + c_o \frac{\partial p}{\partial x} = 0$ will serve as an example. If one substitutes the harmonic solution $p(t,x) = \exp[i(\omega t - kx)]$, the model equation reduces to the dispersion relation $\omega = c_o k$.

However, if one substitutes the same time harmonic solution into a finite difference approximation to the model equation, a dispersion relation $\omega = c_o k + ET$ results where ET are error terms. For example the second-order in Δx and Δt MacCormack method applied to the model equation gives

$$p_l^{n+1} = p_l^n - \frac{c_o}{2}\frac{\Delta t}{\Delta x}(p_{l+1}^n - p_{l-1}^n) + \frac{1}{2}\left[\frac{c_o \Delta t}{\Delta x}\right]^2 (p_{l+1}^n - 2p_l^n + p_{l-1}^n) , \tag{7.18}$$

which turns out to be a well known finite difference method, the Lax-Wendroff scheme. If the substitution $p(l\Delta x, n\Delta t) = \exp[i(\omega n\Delta t - kl\Delta x)]$ is made, the exact dispersion relation for second-order MacCormack is

$$-i(e^{i\omega\Delta t} - 1) = c_o \frac{\Delta t}{\Delta x}\sin(k\Delta x) + 2i\left[c_o \frac{\Delta t}{\Delta x}\right]^2 \sin^2(k\Delta x/2) . \tag{7.19}$$

Similarly the fourth-order MacCormack method applied to the model equation gives

$$p_l^{n+1} = p_l^n + \frac{1}{12}c_o\frac{\Delta t}{\Delta x}(p_{l+2}^n - 8p_{l+1}^n + 8p_{l-1}^n - p_{l-2}^n) - \frac{1}{72}\left[c_o \frac{\Delta t}{\Delta x}\right]^2 (7p_{l+2}^n - 64p_{l+1}^n + 114p_l^n - 64p_{l-1}^n + 7p_{l-2}^n) \tag{7.20}$$

which has an exact dispersion relation

$$-i(e^{i\omega\Delta t} - 1) = \frac{c_o}{6}\frac{\Delta t}{\Delta x}\left[8\sin(k\Delta x) - \sin(2k\Delta x)\right] + \frac{i}{18}\left[c_o \frac{\Delta t}{\Delta x}\right]^2 \left[64\sin^2(k\Delta x/2) - 7\sin^2(k\Delta x)\right]. \tag{7.21}$$

The derivation is straightforward. Notice that both Equations (7.19) and (7.21) approach $\omega = c_o k$ as Δt and Δx approach zero.

These dispersion relation expressions were expanded in Taylor series for $\sin(k\Delta x)$ and $\exp[i\omega\Delta t]$ with the symbolic manipulation program, **Mathematica**.[96] Using these Taylor series expansions, the expressions for the error terms ET in the dispersion relations $\omega = c_o k + ET$ were found for both the second-order and

fourth-order finite difference schemes. Figure 7.1 plots the relative magnitude of ET for the two cases using constants appropriate for electric spark pulses, $c_o = 343$ m/s, $\Delta x = 250 \times 10^{-6}$ s , and $\Delta t = 200 \times 10^{-9}$ s. Note that the values of $|ET|$ for the fourth-order scheme are less than those for the second-order scheme for all wavenumbers, and that the difference between the two errors increases with increasing wavenumber. The idea for plotting the errors of dispersion relations was taken from the dispersion relation plots in the Ph. D. thesis of Trefethen.[97,98]

The improvement from the second to the fourth-order methods is possible only because the ratio $c_o \Delta t/\Delta x$ is nearly 0.25. If one uses much higher or lower values of $c_o \Delta t/\Delta x$, the fourth-order method will lose accuracy since it is fourth-order in Δx but only second-order in Δt. By keeping $c_o \Delta t$ small in a relative sense to Δx, the errors associated with Δt^2 will not dominate the errors associated with Δx^4. See the Turkel reference for the details on this criterion.

Even with the fourth-order in Δx MacCormack method, the nonlinearities in the finite amplitude equations produce high frequencies that the finite difference methods cannot well resolve. Such inaccuracies will be evident near discontinuities such as a shock front, where the variables will change quickly over a few spatial steps. High frequency dispersion can be minimized by the use of an artificial viscosity. As mentioned earlier in this chapter, Walkington and Eversman have used a fourth-order artificial viscosity. Their method takes the form

$$\psi_i^{n+1}\Big|_{\text{new}} = \psi_i^{n+1}\Big|_{\text{old}} - \nu\left[\psi_{i+2}^n - 4\psi_{i+1}^n + 6\psi_i^n - 4\psi_{i-1}^n + \psi_{i-2}^n\right] \qquad (7.22)$$

where ν is small. One way of thinking about this process is that a low pass filter is

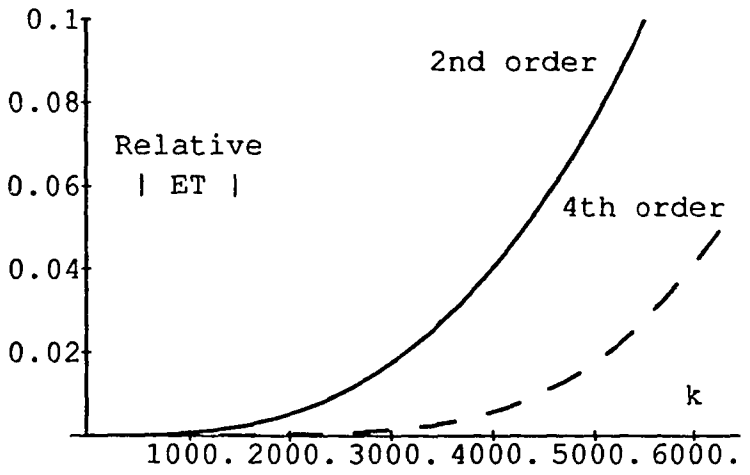

Figure 7.1. The relative magnitudes of the error terms *ET* versus wavenumber for two finite difference schemes. The second-order MacCormack method is represented by the solid line, and the fourth-order in space and second-order in time MacCormack method is given by the dashed line.

run on the variable ψ after each time step. More correctly, note that the above effect is equivalent to adding an artificial viscosity to the model equation $\frac{\partial \psi}{\partial t} + c_o \frac{\partial \psi}{\partial x} = 0$ to obtain

$$\frac{\partial \psi}{\partial t} + c_o \frac{\partial \psi}{\partial x} = -\mu_{\text{art}} \frac{\partial^4 \psi}{\partial x^4} \tag{7.23}$$

where

$$\mu_{\text{art}} = \nu \frac{\Delta x^4}{\Delta t} . \tag{7.24}$$

One usually incorporates classical shear viscosity into the model equation as

$$\frac{\partial \psi}{\partial t} + c_o \frac{\partial \psi}{\partial x} = \mu \frac{\partial^2 \psi}{\partial t^2} . \tag{7.25}$$

It is well known that absorption in (7.25) is proportional to ω^2. Similarly one can show with the assumptions ω close to $c_o k$ and $\mu_{\text{art}} \omega^3 / {c_o}^4 << 1$, that $\exp[i(\omega t - kx)]$ substituted into (7.22) yields $k \doteq k_o - i\alpha_{\text{art}}$ where $\alpha_{\text{art}} = \mu_{\text{art}} \omega^4 / {c_o}^5$. Hence, adding a fourth-order artificial viscosity adds absorption which is proportional to ω^4. By picking μ_{art} carefully, one should be able to dissipate the high frequencies not well resolved by the spatial grid, while leaving the lower frequencies nearly unaffected.

To implement the viscosity technique, Equation (7.22) was used on those points in the computational domain that were calculated using the fourth-order in Δx MacCormack scheme. The method was employed every time step in the following four places: in the first and second components of Equation (7.7) and in the first and third components of Equation (7.8). This procedure applies the artificial viscos-

ity to both of the split components of the continuity equation and to each of the particle velocity equations. Chapter 10 will provide some specific values of ν that were used during calculations.

7.4 Dissipation, High Frequency Resolution, and Implementation

Another advantage of using the MacCormack finite difference schemes is that these methods inherently contain their own dissipative terms, which under usual circumstances are completely ignored. This dissipation is extremely useful in killing parasitic, nonphysical waves that can be launched by the interface of a difference scheme and any boundary condition, which can be absorbing, hard or porous. Such waves often take the form of $(-1)^n$, $(-1)^i$, and $(-1)^j$ and can quickly swamp a valid numerical solution by exponential growth. Trefethen investigated such waves in detail. Sparrow's previous attempt to solve acoustical equations was beset by problems of this nature. That investigation used the Leapfrog finite difference scheme, a simple and standard numerical method.[99] But Leapfrog is inherently nondissipative, which renders it useless for realistic computations involving absorbing and surface boundary conditions.

In using the high-order in space finite difference schemes of the preceding paragraphs, it may not be clear how well the high frequencies will be resolved. As a rule of thumb, one should always use at least 10 to 12 spatial grid points for one wavelength of the highest frequency. Once the spatial grid size Δx has been set using this rule, the time step Δt is then known from the necessity of keeping $c_0 \Delta t / \Delta x$ at about 0.25, as was discussed previously.

Now examine the requirements for resolving the high frequencies involved in the initial near discontinuity of a blast pulse. Suppose a blast wave contains a near discontinuity which has a rise time of $rt = 1\times10^{-4}$ s, with frequencies up to 10 times the $1/(rt)$ frequency. Frequency resolution up to 100 kHz is required to model this wave. For a sound speed of 343 m/s, the wavelength of 100 kHz is 3.43×10^{-3} m, and Δx should be no larger than 3.43×10^{-4} m.

In the results of Chapters 10 and 11, the high frequencies contained in the spark and blast pulses will not be well resolved due to computer memory limitations, so the solutions will not be accurate in the vicinity of the near discontinuities. With the present computer program one cannot practically perform numerous high frequency rise time calculations in two dimensions over large spatial grids.

The above algorithms have been incorporated into a highly vectorized computer program in Fortran. The rectangular symmetry of the spatial grid and the two step fourth-order difference schemes are ideal for parallel implementation on modern supercomputers. Computationally this program requires up to 4 to 5 megawords (million floating point numbers) of continuous memory usage and up to 20 minutes of CPU time on a CRAY-2 for medium sized runs. If one halves the spatial grid size to better resolve high frequencies, one needs 4 times the memory, since this is spatially a 2-D program, and $2 \times 4 = 8$ times the CPU time. If one is interested in propagation primarily in the d direction, the program can window a pulse moving in that direction. This feature has already cut the memory usage of the simulation drastically. However, adaptive grids or different difference schemes may allow one to reduce this memory burden in the future.

Another important point is that in a typical run, the program will generate literally millions of numbers. Public domain software written at the National Center for Supercomputing Applications (NCSA) was used to translate these numbers into color images for interpretation on videotape and color graphics terminals.[100] In addition, the program allows the user to place "numerical receivers" anywhere throughout the spatial domain. These receivers can record the pressure waveforms at the specified spatial points for the duration of a run. The present code is over 5000 lines long, and Appendix B describes it in detail.

8. NUMERICAL ABSORBING BOUNDARY CONDITIONS

This chapter describes the numerical absorbing boundary conditions that are used in this dissertation. First, some background on these conditions is given. The radiation conditions used in this research to correctly model outgoing waves are then detailed. Where radiation conditions are inappropriate, characteristic conditions are used, and these are described also. One might use the characteristic conditions for radiation conditions, but it is shown that the ones first given in this chapter are superior.

Figure 8.1 shows the computational domain used in this thesis. It is bounded by the four sides $z = z_{\min}$, $z = z_{\max}$, $d = d_{\min}$, and $d = d_{\max}$ in the (d,z) plane. The source of sound is assumed to be at the origin $(d = 0, z = 0)$. For free field propagation, radiation conditions are used for all of the boundaries except $d = d_{\min}$ where the characteristic condition is used. For the blast modeling of Chapter 11, the boundary condition along $z = z_{\min}$ is changed from radiation to either that for a hard or a porous ground surface.

8.1 Development of Absorbing Boundary Conditions

First of all, what are absorbing, or radiation, boundary conditions? The solution to acoustical equations using finite differences is restricted to a finite domain since computers have limited memory. Often a larger domain is modeled, however, and boundary conditions on the finite computational domain must be used which allow waves to pass out of the computational domain without reflections.

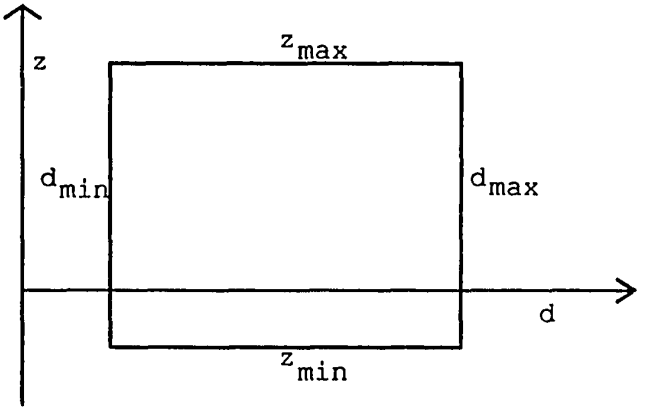

Figure 8.1. Computational domain in the (d,z) plane.

The simulation of nearly reflectionless boundaries has been of recent interest in many fields. The two approaches used are the placement of an absorbing region surrounding the computational domain to slowly "eat up" the waves which impinge on it or the use of an absorbing or radiation condition which is local in space at the edge of the domain and which exactly satisfies an outgoing condition. The approach taken in this thesis focuses on this latter method since the former requires more computer memory.

The problem of false reflections from absorbing boundaries has been overcome in recent years for scalar plane wave propagation. Researchers have been able to develop nearly reflectionless conditions for model equations such as

$$\rho'_{tt} + c_o^2(\rho'_{xx} + \rho'_{yy}) = 0 \tag{8.1}$$

for plane waves with arbitrary angles of incidence on the boundary. Here again ρ' is the acoustic density deviation. Higdon[101,102] has proposed difference approximations to the boundary condition

$$\prod_{j=1}^{p}(\cos\alpha_j \frac{\partial}{\partial t} - c_o \frac{\partial}{\partial x})\rho' = 0 \tag{8.2}$$

which is reflectionless for the $2p$ plane waves at angles $\pm\alpha_j$. Similar, less developed conditions have been given by Keys.[103] Higdon has shown that the often cited boundary conditions of Engquist and Majda[104,105] are actually those in (8.2) with $\alpha_j = 0$ for all j, i.e., they exactly satisfy plane waves only at normal incidence.

These results, however, are not sufficient to find an exact condition for a spherical wave propagating in the system of equations

$$\rho'_t + \rho_o(u_d + v_z + \frac{u}{d}) = 0 \tag{8.3}$$

$$\rho_o u_t + c_o^2 \rho'_d = 0 \tag{8.4}$$

$$\rho_o v_t + c_o^2 \rho'_z = 0 \,. \tag{8.5}$$

These are the resulting two-dimensional linear lossless equations presented in Chapter 4 with the equation of state substituted into (8.4) and (8.5). Gottlieb *et al.*[106] have demonstrated that the scalar results can be used in the case of a hyperbolic system if the boundary conditions are applied to the characteristic variables of the system, instead of to the natural variables such as ρ, u, and v in (8.3), (8.4), and (8.5). Characteristic variables are those variables which decouple, or nearly decouple, the equations in a system of equations from each other. Coughran[107] also has stated that one should base boundary conditions on characteristic variables whenever possible. But the Gottlieb *et al.* result which extends the conditions for scalar equations to systems of equations yields reflectionless boundary conditions only for the case of plane waves, not spherical waves. Additional insight into the complex problem present in finding boundary conditions for hyperbolic systems can be gained from Higdon.[108]

Bayliss and Turkel have examined absorbing boundary conditions for spherical waves in a hyperbolic system of acoustics equations.[109,110] They propose using a sequence of boundary operators B_n to successively annihilate the first n terms of the expansion

$$p(t,r,\theta,\phi) = \sum_{j=1}^{\infty} f_j(t-r,\theta,\phi)/r^j. \tag{8.6}$$

The B_1 operator is useful for the purpose of this thesis and will be used later. In addition, Hagstrom and Hariharan have developed spherical wave absorbing boundary conditions for the Euler equations,[111] but these are not useful for the particular problem addressed here.

Absorbing boundary conditions must be stable numerically as well as accurate, but finding stable conditions is not straightforward. The recent work of Gustafsson,[112] for example, shows that high-order boundary conditions lead to ill-posed problems (unstable numerical schemes). Therefore, only conditions of order one have been used in this research.

8.2 Radiation Boundary Conditions

To exactly absorb a pulse from a monopole spherical source in Equations (8.3), (8.4), and (8.5), notice that the acoustic density ρ' exactly satisfies the separable wave equation

$$\left(\frac{\partial}{\partial t} - c_o \frac{\partial}{\partial r}\right)\left(\frac{\partial}{\partial t} + c_o \frac{\partial}{\partial r}\right)(r\rho') = 0 \tag{8.7}$$

while u, v, and $v_r = u\sin\theta + v\cos\theta$ do not. Here, v_r is the spherical component of particle velocity in the spherical radial direction r. Because the particle velocities will not satisfy (8.7), the conditions on the density and particle velocities will be different. Taking the outgoing part of (8.7) gives the condition

$$\left(\frac{\partial}{\partial t} + c_o\left(\frac{\partial}{\partial r} + \frac{1}{r}\right)\right)\rho' = 0 \tag{8.8}$$

which is the Bayliss Turkel B_1 condition on the acoustic density. Now look at the

one-dimensional equations similar to (8.3), (8.4), and (8.5) in the spherical coordinate system (r,ϕ,θ) with only r variations,

$$\frac{\partial \rho'}{\partial t} + \rho_o \left[\frac{2v_r}{r} + \frac{\partial v_r}{\partial r} \right] = 0 \tag{8.9}$$

$$\rho_o \frac{\partial v_r}{\partial t} + c_o^2 \frac{\partial \rho'}{\partial r} = 0 \,. \tag{8.10}$$

Equation (8.10) gives the exact condition relating ρ' to the time derivative of v_r.

It is not safe to base a boundary condition on (8.10) explicitly, because it involves v_r which depends on both u and v. For boundaries where z or d are constant, as in Figure 8.1, the boundary conditions should not not involve the variables u and v, respectively. This is one of the results of an important paper by Majda and Osher,[113] and it is important for this thesis since boundaries of the type z or d a constant will be used.

For an upper boundary $z = z_{\max}$ with the interior domain being $z_{\max} < z$, one can insert the geometrical relation $v = v_r \cos\theta$ in (8.10) to produce the equation

$$\frac{\partial v}{\partial t} + \cos\theta \frac{c_o^2}{\rho_o} \frac{\partial \rho'}{\partial r} = 0 \,. \tag{8.11}$$

The term $\frac{\partial \rho'}{\partial r}$ is easily found from

$$\frac{\partial \rho'}{\partial r} = \cos\theta \frac{\partial \rho'}{\partial z} + \sin\theta \frac{\partial \rho'}{\partial d} \,. \tag{8.12}$$

Thus, valid absorbing boundary conditions for $z = z_{\max}$ are (8.8) and (8.11) with the insertion of (8.12). They are stable and exact for a monopole source at the origin. This condition is also correct for a boundary $z = z_{\min}$, except that its imple-

mentation is different. The implementation used for $z_{\max}$ absorbing boundary condition was

$$\frac{v_{i,J}^{n+1} - v_{i,J}^{n}}{\Delta t} + \cos\theta \frac{c_o^2}{\rho_o}\left[\frac{\rho'^{n}_{i,J} - \rho'^{n}_{i-1,J}}{\Delta d}\sin\theta + \frac{\rho'^{n}_{i,J} - \rho'^{n}_{i,J-1}}{\Delta z}\cos\theta\right] = 0 \tag{8.13}$$

for $2 \leq j \leq I$ in the d direction in the domain $1 \leq i \leq I$ in d and $1 \leq j \leq J$ in z. For $z_{\min}$ the implementation was

$$\frac{v_{i,1}^{n+1} - v_{i,1}^{n}}{\Delta t} + \cos\theta \frac{c_o^2}{\rho_o}\left[\frac{\rho'^{n}_{i,1} - \rho'^{n}_{i-1,1}}{\Delta d}\sin\theta + \frac{\rho'^{n}_{i,2} - \rho'^{n}_{i,1}}{\Delta z}\cos\theta\right] = 0\,. \tag{8.14}$$

In the case of an outgoing condition at $d = d_{\max}$, where u is needed instead of v, the relation

$$\frac{\partial u}{\partial t} + \sin\theta \frac{c_o^2}{\rho_o}\frac{\partial \rho'}{\partial r} = 0 \tag{8.15}$$

was similarly obtained from (8.10). Equations (8.15) and (8.8) were used for the absorbing boundary here. The particle velocity condition for $d = d_{\max}$ was implemented as

$$\frac{u_{I,j}^{n+1} - v_{I,j}^{n}}{\Delta t} + \sin\theta \frac{c_o^2}{\rho_o}\left[\frac{\rho'^{n}_{I,j} - \rho'^{n}_{I-1,j}}{\Delta d}\sin\theta + \frac{\rho'^{n}_{I,j} - \rho'^{n}_{I,j-1}}{\Delta z}\cos\theta\right] = 0\,. \tag{8.16}$$

For each of the boundaries $z = z_{max}$, $z = z_{min}$, and $d = d_{max}$, Equation (8.8) was discretized similarly.

All of the boundaries derived in this chapter are for linear lossless conditions. Fortunately, the absorption and nonlinearities present in the air propagation equations are weak. This fact allows the use of the linear conditions specified here to work with the nonlinear lossy equations solved in this thesis.

The conditions here do not account for the variable s_{fr}, the acoustic entropy deviation, however. But since this variable is associated only with the losses in the equations of Chapter 4 and 7, its specification is not critical near absorbing boundaries, but is so near physical surfaces. Near the boundary $d = d_{min}$ and near the radiation boundaries, s_{fr} was updated by simple extrapolations. Chapter 10 will specify boundary conditions on s_{fr}, as well as ρ', u, and v for hard surfaces.

8.3 Characteristic Boundary Conditions

The boundary at $d = d_{min}$ is not a radiation boundary, since in this thesis the sound pulses will be initially placed at $d > d_{min}$ and propagate in the $+d$ direction. The boundary condition implemented along $d = d_{min}$ is called a characteristic boundary since it is based on the concept of characteristic variables, defined in Section 8.1.

Recall the one-dimensional spherically symmetric acoustic equations in density deviation and radial particle velocity, Equations (8.9) and (8.10). It is possible to rewrite these equations in the form

$$\mathbf{w}'_t + \begin{bmatrix} c_o & 0 \\ 0 & -c_o \end{bmatrix} \mathbf{w}'_r + \frac{c_o}{r} \begin{bmatrix} 1 & -1 \\ 1 & -1 \end{bmatrix} \mathbf{w}' = 0 \tag{8.17}$$

where

$$\mathbf{w}' = \begin{bmatrix} \frac{1}{\sqrt{2}} \rho' + \frac{\rho_o}{c_o \sqrt{2}} v_r \\ \frac{1}{\sqrt{2}} \rho' - \frac{\rho_o}{c_o \sqrt{2}} v_r \end{bmatrix} = \begin{bmatrix} w1' \\ w2' \end{bmatrix} \tag{8.18}$$

and where the coefficient matrix of $\mathbf{w}'_r$ is diagonal.

This transformation is made possible by writing (8.9) and (8.10) as the system

$$\mathbf{A}_t + \mathbf{B}\mathbf{A}_r + \mathbf{C}\mathbf{A} = 0 \tag{8.19}$$

where

$$\mathbf{A} = \begin{bmatrix} \rho' \\ v_r \end{bmatrix}, \tag{8.20}$$

$$\mathbf{B} = \begin{bmatrix} 0 & \rho_o \\ \frac{c_o^2}{\rho_o} & 0 \end{bmatrix}, \tag{8.21}$$

$$\mathbf{C} = \begin{bmatrix} 0 & \frac{2\rho_o}{r} \\ 0 & 0 \end{bmatrix}. \tag{8.22}$$

The eigenvalues of $\mathbf{B}$ are easily found as c_o and $-c_o$, and two right eigenvectors associated with these eigenvalues are

$$r_1 = \begin{bmatrix} \frac{1}{\sqrt{2}} \\ \frac{c_o}{\rho_o \sqrt{2}} \end{bmatrix} \tag{8.23}$$

and

$$r_2 = \begin{bmatrix} \frac{1}{\sqrt{2}} \\ -\frac{c_o}{\rho_o \sqrt{2}} \end{bmatrix}, \tag{8.24}$$

respectively. One can also find two left eigenvalues associated with c_o and $-c_o$. They are

$$l_1 = \begin{bmatrix} \frac{1}{\sqrt{2}} & \frac{\rho_o}{c_o \sqrt{2}} \end{bmatrix} \tag{8.25}$$

and

$$l_2 = \begin{bmatrix} \frac{1}{\sqrt{2}} & \frac{-\rho_o}{c_o \sqrt{2}} \end{bmatrix}, \tag{8.26}$$

respectively. Finding such eigenvectors means **B** may be diagonalized through

$$\Lambda = \mathbf{SBS}^{-1} \tag{8.27}$$

where

$$\mathbf{S} = \begin{bmatrix} l_1 \\ l_2 \end{bmatrix} \tag{8.28}$$

and

$$\mathbf{S}^{-1} = \begin{bmatrix} r_1 & r_2 \end{bmatrix}. \tag{8.29}$$

Multiplying (8.19) by **S** from the left and expanding **A** as $\mathbf{A} = \mathbf{S}^{-1}\mathbf{SA} = \mathbf{S}^{-1}\mathbf{w}'$ gives (8.17). Here the variables $\mathbf{w}'$ are related to **A** by

$$\mathbf{w}' = \mathbf{SA} \tag{8.30}$$

and

$$\mathbf{A} = \mathbf{S}^{-1}\mathbf{w}' . \tag{8.31}$$

The variable $w1'$ is called the outgoing characteristic variable of these equations, and $w2'$ is the incoming characteristic variable.

Similarly, one can diagonalize the cylindrical 2-D Equations (8.3), (8.4), and (8.5), with respect to the d direction. The resulting equations are

$$\mathbf{w}_t + \mathbf{D}\mathbf{w}_d + \mathbf{E}_1\mathbf{w}_z + \mathbf{E}_2\mathbf{w} = 0 \tag{8.32}$$

for a diagonal $\mathbf{D}$ matrix where

$$\mathbf{D} = \begin{bmatrix} c_o & 0 & 0 \\ 0 & -c_o & 0 \\ 0 & 0 & 0 \end{bmatrix}, \tag{8.33}$$

$$\mathbf{E}_1 = \begin{bmatrix} 0 & 0 & \frac{\rho_o}{\sqrt{2}} \\ 0 & 0 & \frac{\rho_o}{\sqrt{2}} \\ \frac{c_o^2}{\rho_o\sqrt{2}} & \frac{c_o^2}{\rho_o\sqrt{2}} & 0 \end{bmatrix}, \tag{8.34}$$

$$\mathbf{E}_2 = \begin{bmatrix} \frac{c_o}{2d} & \frac{-c_o}{2d} & 0 \\ \frac{c_o}{2d} & \frac{c_o}{2d} & 0 \\ 0 & 0 & 0 \end{bmatrix}, \tag{8.35}$$

and

$$\mathbf{w} = \begin{bmatrix} \frac{1}{\sqrt{2}}\rho' + \frac{\rho_o}{c_o\sqrt{2}}u \\ \frac{1}{\sqrt{2}}\rho' - \frac{\rho_o}{c_o\sqrt{2}}u \\ v \end{bmatrix} = \begin{bmatrix} w1 \\ w2 \\ w3 \end{bmatrix}. \tag{8.36}$$

Here the characteristic variable with respect to the $+d$ direction is $w1$, the charac-

teristic variable with respect to the $-d$ direction is $w2$, and $w3 = v$ is not a characteristic variable. Examine (8.32) for the case of plane wave propagation in the + or − direction. Here $v = w3 = 0$. For propagation in the $+d$ direction, the density and particle velocity are in phase as $\rho' = \frac{\rho_o}{c_o} u$, which means $w2 = 0$. Similarly, for the $-d$ direction, $\rho' = -\frac{\rho_o}{c_o} u$, so $w1 = 0$.

Because of these properties, the second case $w1 = 0$ was used as the boundary condition nearest the source at $d = d_{\min} > 0$ for this research. Specifying $w1 = 0$ implies that no waves will enter the domain $d > d_{\min}$ in the direction $+d$. To implement holding $w1 = 0$, the variable $w2$ was extrapolated over one Δt in the d direction along the boundary $d = d_{\min}$. In finite difference notation

$$w2_{1,j}^{n+1} = w2_{2,j}^{n} \tag{8.37}$$

for all j implements the method, using the first two components of (8.36) and the first two components of

$$\begin{bmatrix} \rho' \\ u \\ v \end{bmatrix} = \begin{bmatrix} \frac{1}{\sqrt{2}}(w1 + w2) \\ \frac{c_o}{\rho_o \sqrt{2}}(w1 - w2) \\ w3 \end{bmatrix} \tag{8.38}$$

with $w1 = 0$. The variable v is not changed on a $d_{\min}$ boundary update.

Now return to the 1-D spherical Equations (8.17) and (8.18). Unlike the plane wave case, ρ' and v are out of phase except in the very far field. Restated, an outgoing spherical wave contains both an incoming and an outgoing characteristic com-

ponent for finite distances from the source. This fact means that if one sets $w2' = 0$ in (8.17) and (8.18), that the first equation of (8.17) used as an absorbing boundary condition will produce false reflections for outgoing waves. To demonstrate this point, the next section will contain a comparison between the condition $w2' = 0$ as a radiation boundary condition and the conditions derived in Section 8.2.

8.4 Absorbing Boundary Condition Comparison

This section compares three candidates for absorbing boundary conditions to see which has the minimum reflection. The upper radiation boundary condition, $z = z_{\max}$, was the boundary tested.

The equations of Chapter 4 were solved using the methods of Chapter 7 in this comparison, under the stipulations κ, μ, and $\mu_B = 0$, with a peak SPL of 140 dB. This is equivalent to solving a linear lossless system of acoustics equations. The upper boundary was placed at $z_{\max} = 0.03$ m, and the computational domain was $z \leq z_{\max}$.

A spherical spark pulse, of the type described in Chapter 6, was used as an initial condition on ρ', u, and v. Initially the pulse extended to 0.03 m from the origin, with $c_o = 343$ m/sec and $\rho_o = 1.21$ kg/m^3, values appropriate for air.

Four computations were performed with different conditions used along $z = z_{\max}$. In all four calculations values of u were found from the interior equations, since this is not a boundary variable along $z = z_{\max}$. Computations one through four varied in the way ρ' and v, the boundary variables, were calculated.

In case one the spherical characteristic variables of Section 8.3,

$$\frac{\partial w1'}{\partial t} + c_o \frac{\partial w1'}{\partial r} + \frac{c_o}{r}\left(w1' - w2'\right) = 0 \tag{8.39}$$

and $w2' = 0$, were used. Case two used the Bayliss Turkel B_1 boundary condition on the density deviation,

$$\rho'_t + c_o(\rho'_r + \rho'/r) = 0\,, \tag{8.40}$$

and the interior equation on v,

$$\rho_o v_t + c_o^2 \rho'_z = 0\,. \tag{8.41}$$

Case three also used the B_1 condition on ρ', but on v used

$$\rho_o v_t + \cos\theta c_o^2 \rho'_r = 0\,, \tag{8.42}$$

the pair of boundary conditions from Section 8.2. The fourth case, to act as the ideal condition, was implemented by extending the domain beyond $z_{\max}$ in z, so that there would be no upper boundary to reflect off. The computation time for case four was significantly greater than that of the other three cases because of the former's larger domain. The conditions in cases one through three were discretized using simple forward and backward differences.

For the four computations, $\Delta x = \Delta d = \Delta z = 250\times10^{-6}$ m and $\Delta t = 200\times10^{-9}$ s were used making $c_o \Delta t/\Delta x = 0.2744$ which is appropriate for the fourth-order method. The pulse was allowed to propagate for 600 time steps or 120 microseconds from its initial condition. A numerical receiver was placed at ($d =$ 0.04 m, $z = 0.025$ m) to monitor the wave passage. Thus the receiver intercepts

the reflected part of the wave incident on the absorbing boundary at about 50 degrees from normal. The computation was performed on a Cray-2 supercomputer, and each of the four runs took about 180 s on a single CPU.

Figures 8.2, 8.3, and 8.4 are plots of acoustic pressure, $p = c_0^2 \rho'$, at the receiver, comparing the ideal condition with the boundary conditions one through three, respectively. Case four is plotted in each of the three figures with a dashed line, and each of the others is represented by a solid line. Pressure is given in Pascals and time in microseconds. Figures 8.5, 8.6 and 8.7 show the difference between conditions one through three and the ideal condition four. For example, Figure 8.2 shows condition one with a solid line, the ideal condition four with a dashed line, and Figure 8.5 gives their difference.

Each of the computations was identical until about 65 μs when the wave reflected from the artificial boundaries arrived at the receiver. Figures 8.2 and 8.5 show the reflection over much of the trough of the pulse for condition one, which is due to the continual misspecification of the incoming characteristic variable, $w_2' = 0$. Hence, this comparison verifies that in the near field there is an incoming characteristic component for an outgoing spherical wave.

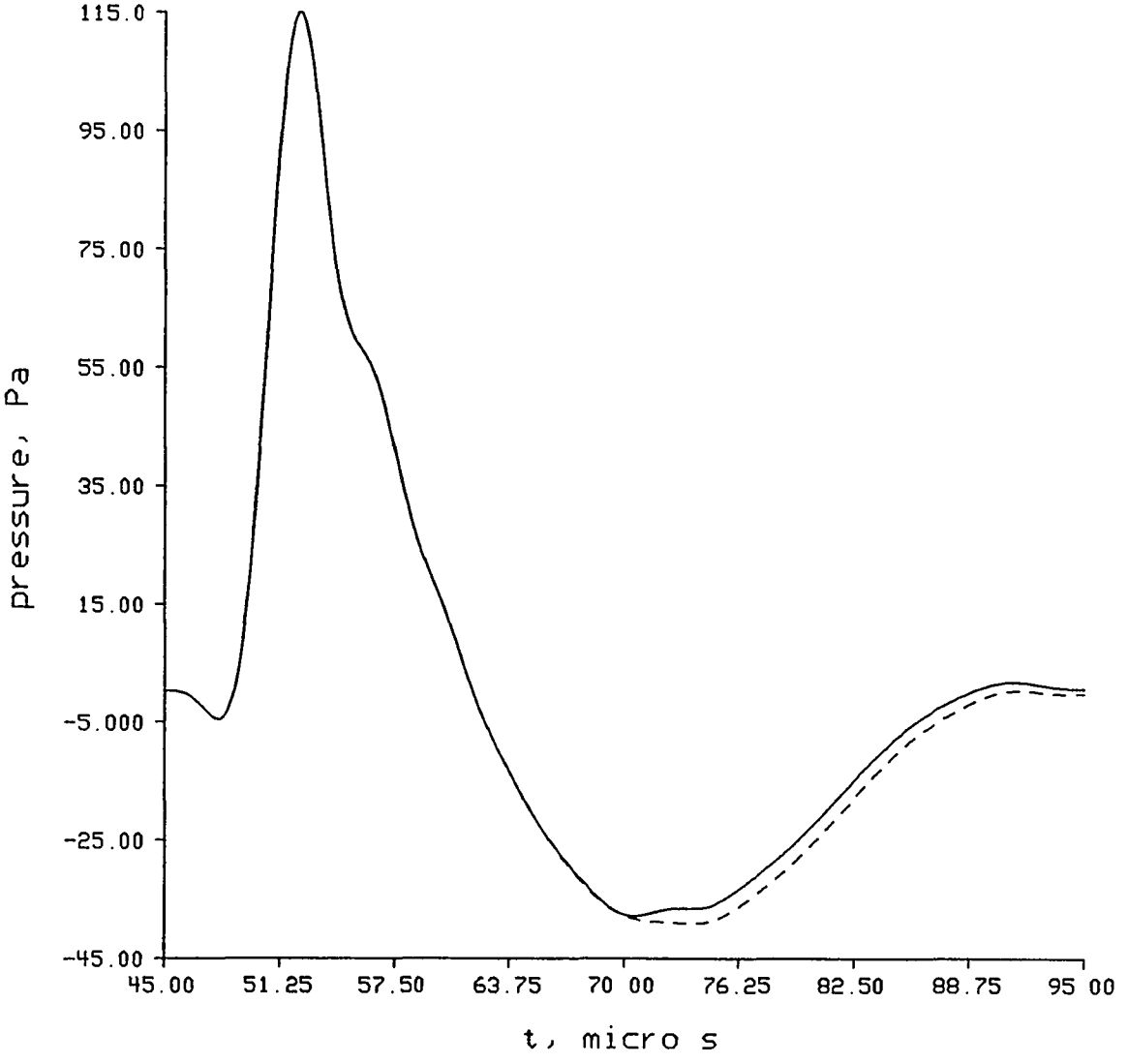

Figure 8.2. Acoustic pressure in Pa versus time at the numerical receiver. Case one is the solid line, and case four, the ideal, is dashed.

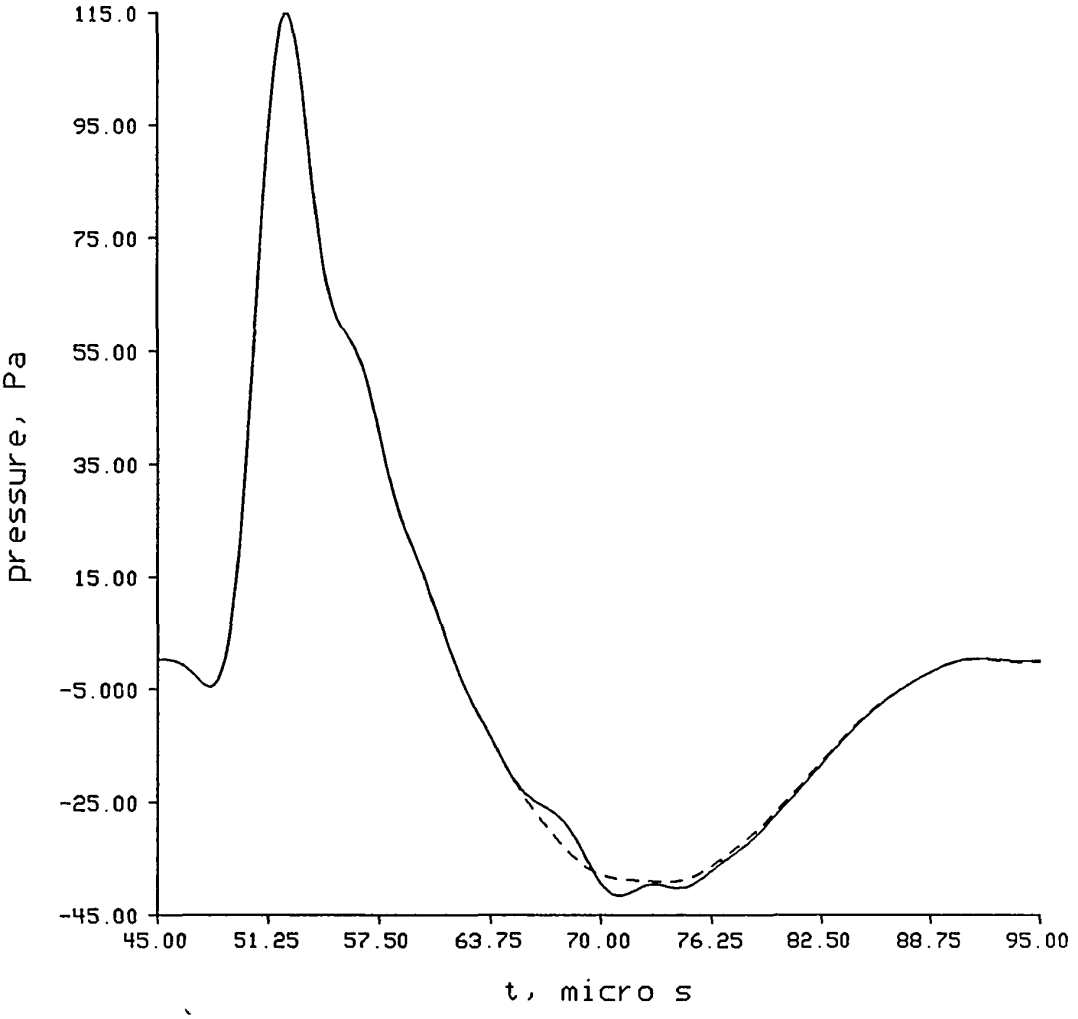

Figure 8.3. Acoustic pressure in Pa versus time at the numerical receiver. Case two is the solid line, and case four, the ideal, is dashed.

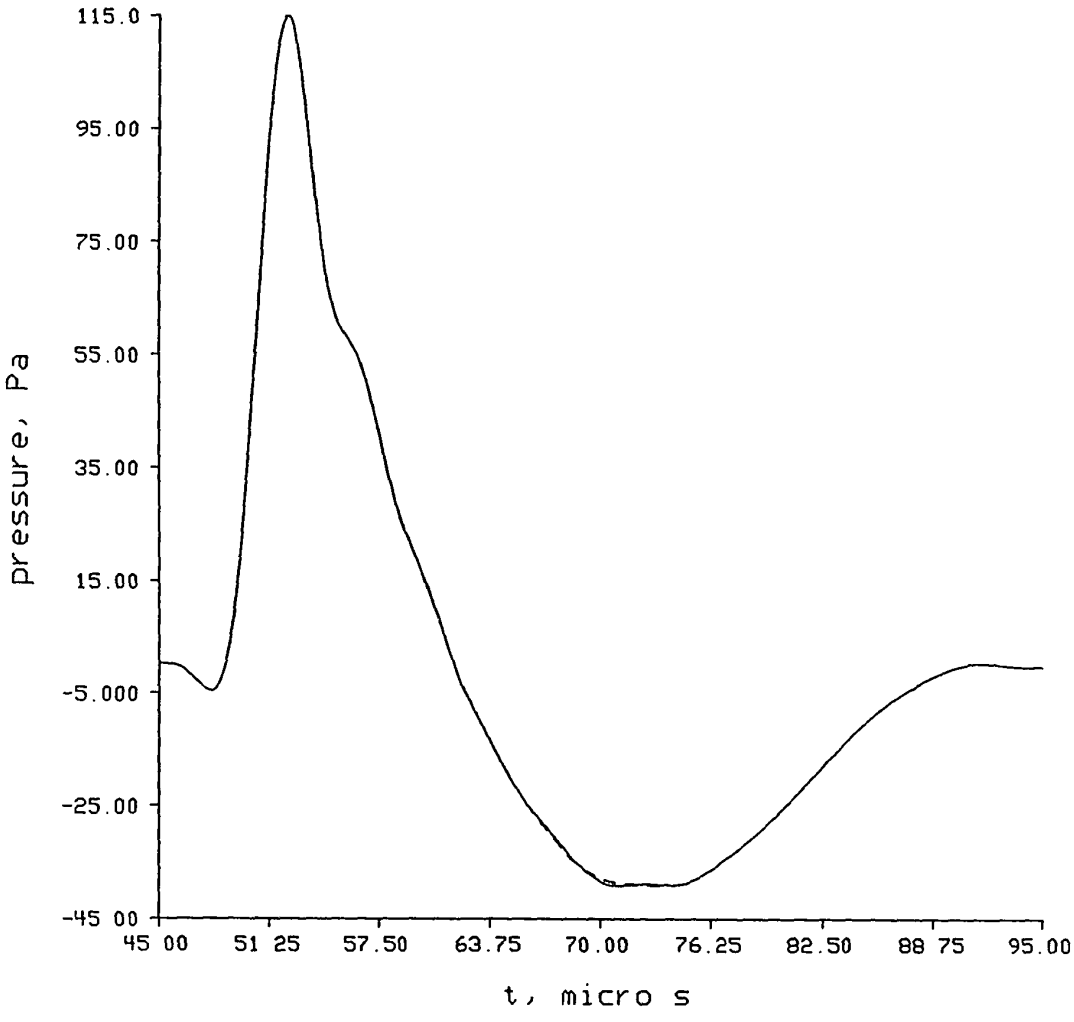

Figure 8.4. Acoustic pressure in Pa versus time at the numerical receiver. Case three is the solid line, and case four, the ideal, is dashed.

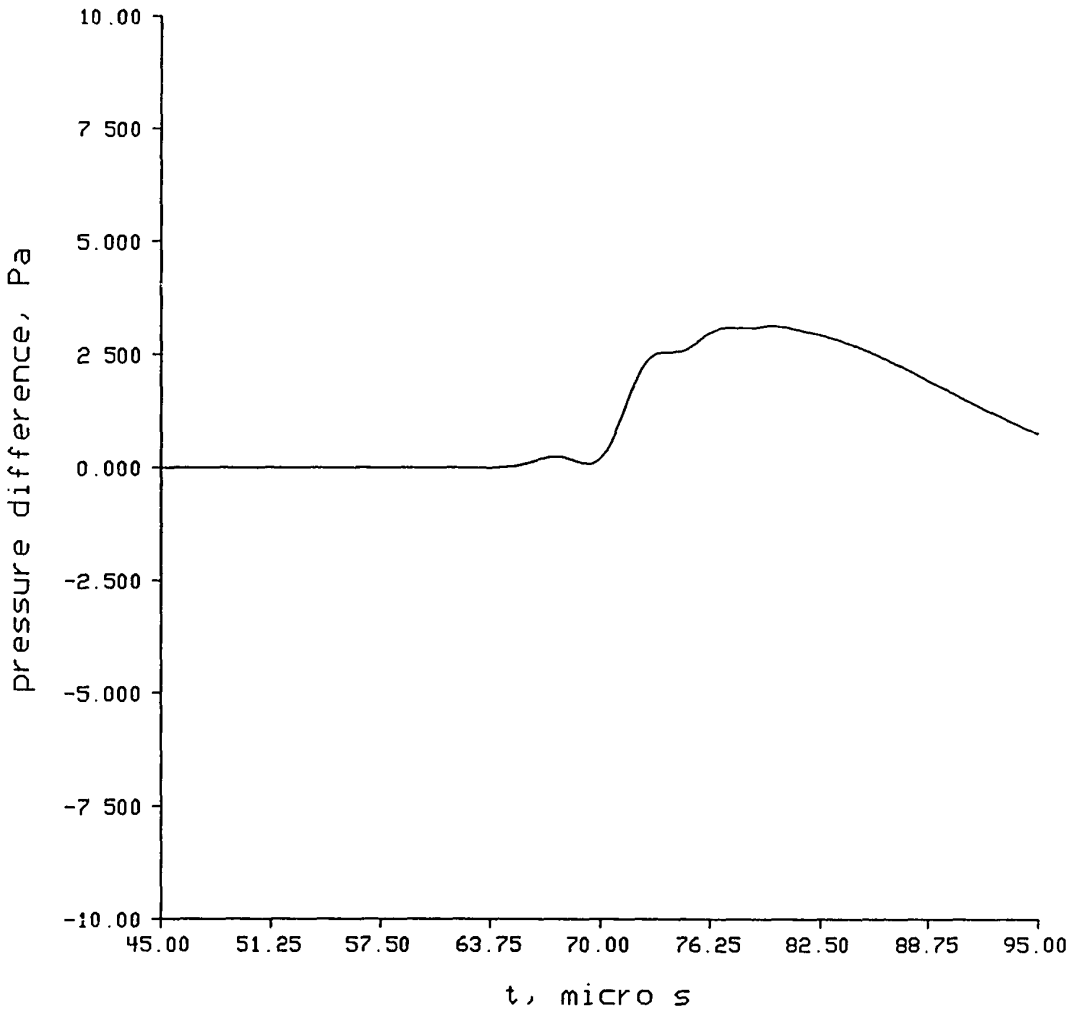

Figure 8.5. Acoustic pressure difference in Pa between cases one and four.

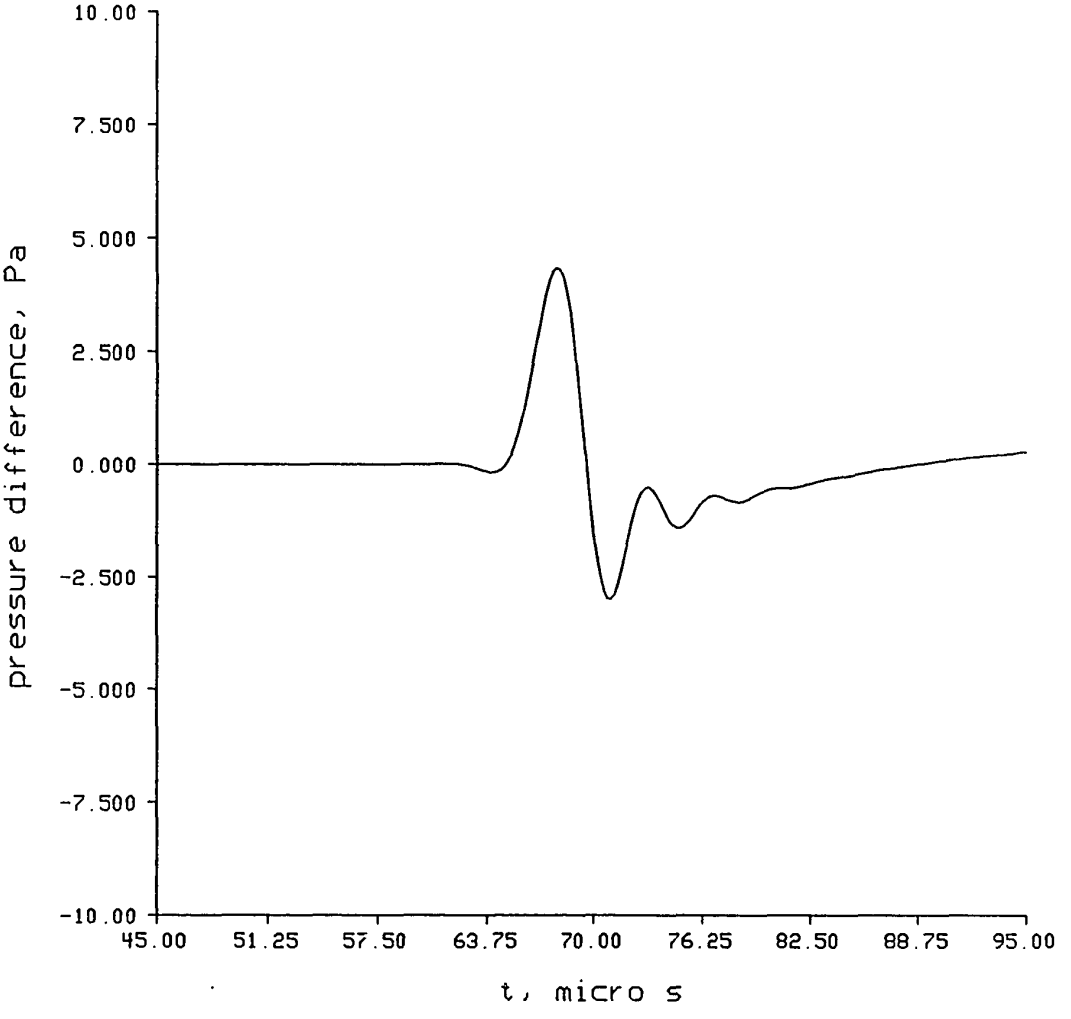

Figure 8.6. Acoustic pressure difference in Pa between cases two and four.

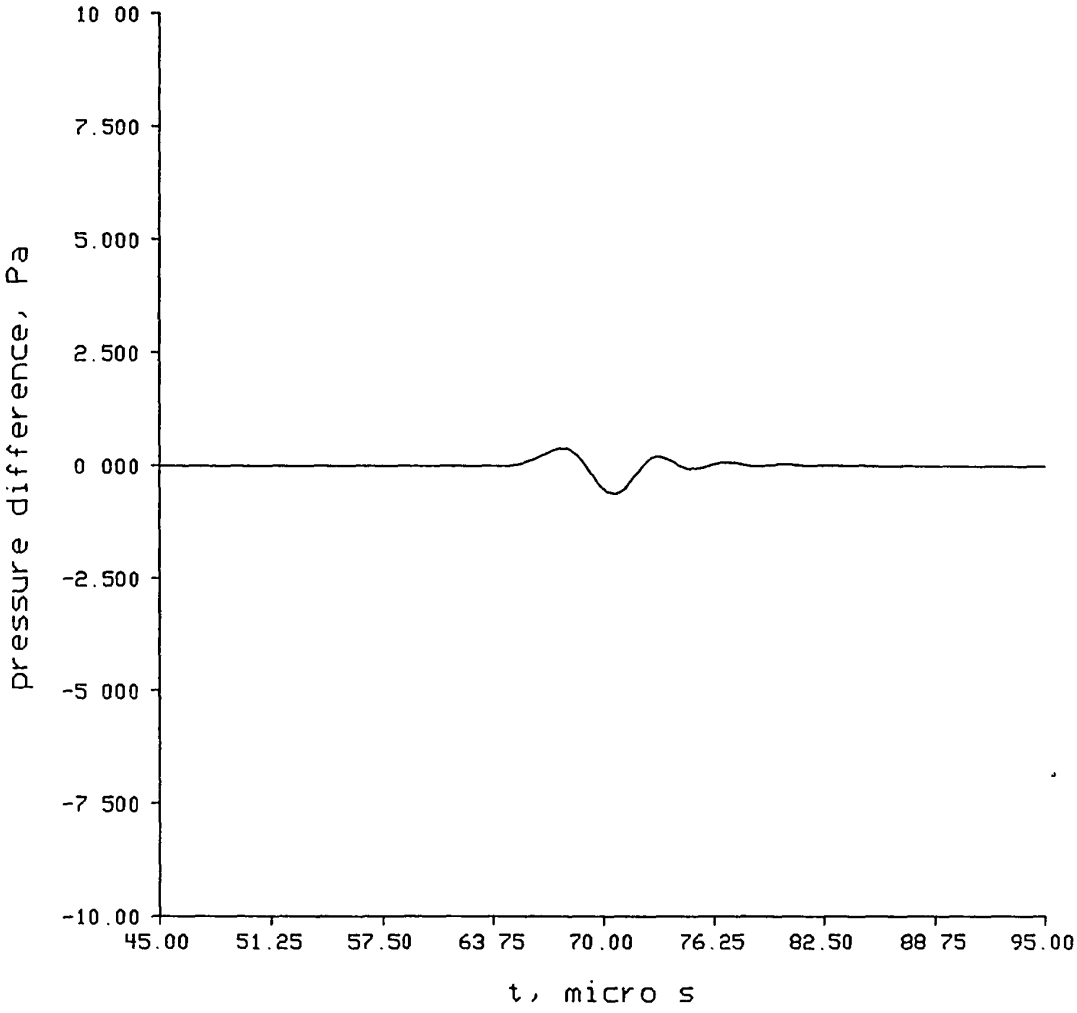

Figure 8.7. Acoustic pressure difference in Pa between cases three and four.

Case two in Figures 8.3 and 8.6 shows a substantial deviation from the ideal which is greatest at the beginning of the reflection, while case three, the conditions of Section 8.2, is nearly identical to the ideal in Figures 8.4 and 8.7. The dips in the waveforms in front and behind the peak of the pulse for all four cases are not due to reflections. They were due solely to numerical dispersion in the interior finite difference method. It is near large waveform gradients that the high frequencies not being well resolved by the grid first manifest themselves.

Not shown in Figures 8.2 through 8.7 is the fact that one could see almost no reflected waves off the numerical boundary for case three in color raster plots of the numerical domain. On the other hand, the case one boundary always showed a strong spherical wave reflection, and the case two boundary showed a stronger reflection the more grazing the angle of incidence was, although for near normal incidence little reflection was present.

9. NUMERICAL SOLUTION TO THE POROUS EQUATIONS

This chapter will present a numerical solution for the time-dependent phenomenological equations for the porous medium described in Chapter 5. This numerical solution will be based on the assumption of local reaction, and all waves propagating into the pores will be assumed to propagate normally to the surface.

Using the linearized version of Attenborough's equations (5.12) to (5.14) with p' eliminated, and assuming one-dimensional propagation in the z direction with z direction particle velocity v, the time-dependent equations to be solved numerically are

$$\Omega \frac{\partial \rho'}{\partial t} + \rho_o \frac{\partial v}{\partial z} = 0 \tag{9.1}$$

$$\rho_o \frac{K}{\Omega} \frac{\partial v}{\partial t} + \Phi v + c_o^2 \frac{\partial \rho'}{\partial z} = 0 \,. \tag{9.2}$$

Recall from the last chapter that the required numerical boundary conditions along the ground boundary were on ρ' and v. In solving the air and porous equations together, the porous surface will lie on $z = z_{\min}$. The obvious boundary conditions for this case are

$$\rho'_{\text{air}} = \rho'_{\text{porous}} \tag{9.3}$$

$$v_{\text{air}} = v_{\text{porous}} \tag{9.4}$$

along the boundary where ρ'_{air} and v_{air} are the variables in Chapter 4 Equations (4.34) and (4.36) and ρ'_{porous} and v_{porous} are the variables in (9.1) and (9.2). Note that although v_{porous} is an average particle velocity and v_{air} is not, that (9.4) is still correct because they are both quantities defined at points in space.

To solve (9.1) and (9.2), one variant of the second-order in space and time MacCormack finite difference method was used, giving

$$\rho'^{\tilde{n}}_j = \rho'^{n}_j - \frac{\rho_o}{\Omega}\frac{\Delta t}{\Delta x}(v^n_{j+1} - v^n_j) \tag{9.5}$$

$$v^{\tilde{n}}_j = v^n_j - \frac{\Omega c_o^2}{\rho_o K}\frac{\Delta t}{\Delta x}(\rho'^{n}_{j+1} - \rho'^{n}_j) - \Delta t\frac{\Omega \Phi}{\rho_o K}v^n_j \tag{9.6}$$

$$\rho'^{n+1}_j = \frac{1}{2}\left[\rho'^{n}_j + \rho'^{\tilde{n}}_j - \frac{\rho_o}{\Omega}\frac{\Delta t}{\Delta x}(v^{\tilde{n}}_j - v^{\tilde{n}}_{j-1})\right] \tag{9.7}$$

$$v^{n+1}_j = \frac{1}{2}\left[v^n_j + v^{\tilde{n}}_j - \frac{\Omega c_o^2}{\rho_o K}\frac{\Delta t}{\Delta x}(\rho'^{\tilde{n}}_j - \rho'^{\tilde{n}}_{j-1}) - \Delta t\frac{\Omega \Phi}{\rho_o K}v^{\tilde{n}}_j\right]. \tag{9.8}$$

This finite difference scheme must follow stricter stability guidelines than did the equations in air, due to the presence of the flow resistivity Φ. One can find the restrictions on the method by the standard, but tedious, procedure of performing a Von Neumann stability analysis.[114] Let

$$\begin{bmatrix}\rho'^{n}_j \\ v^n_j\end{bmatrix} = \begin{bmatrix}A^n \\ B^n\end{bmatrix} e^{ik_z j\Delta z}, \tag{9.9}$$

then one can determine the amplification matrix G where

$$\begin{bmatrix}A^{n+1} \\ B^{n+1}\end{bmatrix} = \mathbf{G}(\Delta t, k_z)\begin{bmatrix}A^n \\ B^n\end{bmatrix} \tag{9.10}$$

by manipulating Equations (9.5) to (9.8). The result for low frequencies, $k_z \rightarrow 0$, is

$$\mathbf{G}(\Delta t, 0) = \begin{bmatrix}1 & 0 \\ 0 & \xi\end{bmatrix} \tag{9.11}$$

where

$$\xi = 1 - \frac{\Omega \Phi \Delta t}{\rho_o K} + \frac{1}{2}\left(\frac{\Omega \Phi \Delta t}{\rho_o K}\right)^2 . \tag{9.12}$$

The eigenvalues of $\mathbf{G}(\Delta t,0)$ are

$$\lambda_{1,2} = \frac{1}{2}\left(1 + \xi \pm \left[(1+\xi)^2 - 4\xi\right]^{1/2}\right) \tag{9.13}$$

from the solution of $\det(\lambda \mathbf{I} - \mathbf{G}(\Delta t,0)) = 0$. The Von Neumann necessary condition for stability states that

$$\left|\lambda_i\right| \leq 1 + O(\Delta t) \tag{9.14}$$

for all i. Under the condition $\Phi \rightarrow 0$, no flow resistance, $\xi = 0$ which implies $\left|\lambda_1\right| = \left|\lambda_2\right| = 1$, and stability is insured. However, for $\Phi \neq 0$ one can see from (9.12) that the time step Δt, relative to $\frac{\Omega \Phi}{\rho_o K}$, determines whether the criterion (9.14) is met. It was found that choosing a Δt too large in the porous medium numerical solution will, in fact, make the numerical solution go unstable.

Since at low frequencies the speed of sound in the air is on the order of 10 times faster than the speed of propagation in a porous medium, the wavelengths are on the order of 10 times shorter in the porous medium than in the air. Because of this difference, the Δx grid spacing in the pores should be on the order of 1/10th of the size of the grid spacing Δx in the air. The question then becomes how the numerical scheme in the air will be mated with the numerical scheme in the pores, considering this difference in grid spacings in the air and pores.

It was chosen to numerically couple the pore solution to the air solution by refining the air grid in the z direction as it comes into contact with the pore grid.

Set $\Delta x_{air} = 10\Delta x_{pores}$, and $\Delta t_{air} = 10\Delta t_{pores}$. Then, referring to Figure 9.1, refine the air between $j=2$ and $j=1$ and $t=(n+1)\Delta t$ and $t=n\Delta t$ by 10. Calculate the $j=2$, $t=(n+1)\Delta t_{air}$ point by the interior scheme using Δx_{air} and Δt_{air} from points $j=1$, 2, and 3 at time $t=n\Delta t_{air}$. Then interpolate in time the values between $t=(n+1)\Delta t_{air}$ and $n\Delta t_{air}$ for $j=2$ to obtain the values by the time increments of Δt_{pores} for $j=2$, indicated by the x's in Figure 9.1. Next calculate the values of air at the spatial points between $j=2$ and $j=1$ and the values of the porous medium at all spatial points less than $z = z_{min}$, using the refined values Δx_{pores} and Δt_{pores}, until the $j=1$ $t=(n+1)\Delta t_{air}$ values are calculated. This is the boundary condition point needed for the next iteration. Thus, air values between $j=1$ and $j=2$ and the pore values are solved ten times as often as the air values in the rest of the air grid.

In 1985 Marsha Berger analyzed this method of interpolating in time and refining in time and space thoroughly for stability.[115] Her analysis is for a model equation solved using the Lax-Wendroff method, very similar to the MacCormack techniques used in this thesis. She found that refining in both time and space by integer multiples was stable. Note that if a nondissipative difference method were used for the computations with this type of grid refinement, the numerical solutions may not be stable.

To test this coupling of the air to the porous ground, computations were performed to estimate the actual surface impedance of the porous model. It is possible to determine impedance using impedance tube techniques.[116,117] Both 50 Hz and 25 Hz linear plane wave sinusoids were sent propagating in the $-z$ direction, normally

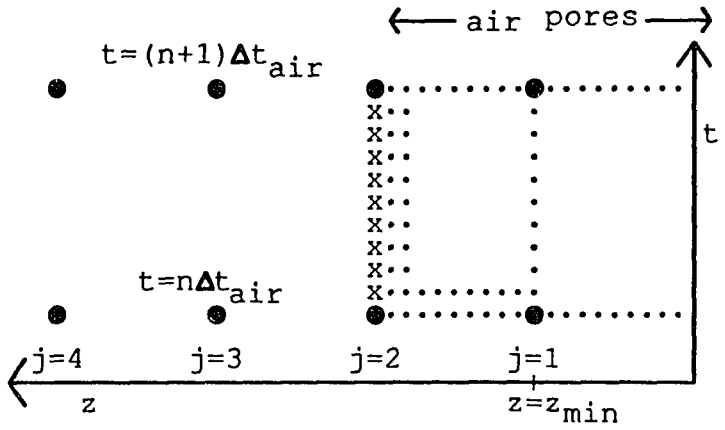

Figure 9.1. Finite difference implementation of the air-porous interface. All the points to the left of $z = z_{min}$ are air and those to the right are porous. The air points between j=2 and j=1, like all the porous points, are refined in z and t by 10 compared to the rest of the air grid.

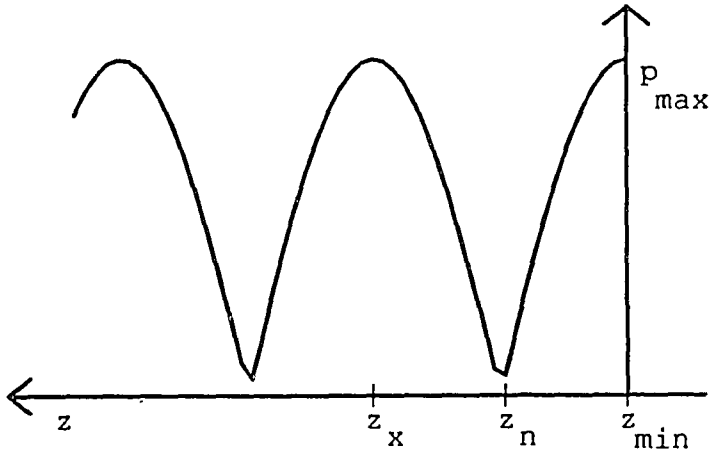

Figure 9.2. Impedance measurement maximum pressure over time as a function of distance from the air-porous interface. The first minimum p_{max} from the interface is at z_n, and the first maximum is at z_x.

onto the porous medium from the air. A standing wave pattern results from the direct wave and the reflected wave superposing. Figure 9.2 plots the maximum pressure over time, p_{max}, as a function of distance from the air-porous boundary at z_{min}. The particular wave envelope shown is typical of the type seen with a large standing wave ratio, characteristic of a high magnitude of impedance. To calculate numerically the impedance, the three numbers needed are the distance $z_n - z_{min}$, the maximum p_{max} at z_x, and the minimum p_{max} at z_n.

The measurements made were difficult and crude since the finite difference grids could not be made fine enough using the two-dimensional program. Finer grids would have resolved the distance of the minimum p_{max} to the air-pore interface more precisely but would have used a tremendous amount of computer time. The value of Δx for both simulations presented here was 0.0625 m, and the peak pressure of the sinusoid was 140 dB, making the wave linear.

For 25 Hz, the measured value of the impedance was $Z/\rho_o c_o = 14.737 + i33.146$, and for 50 Hz, the value was $Z/\rho_o c_o = 11.031 + i36.348$. These impedances are low in magnitude compared to the results of Attenborough's low frequency interpretation of the phenomenological porous model, as seen in Table 5.1. The phases are significantly different also. Unfortunately, it is difficult to tell whether the difference between the values of impedances is due to measurement error, which was a problem, or due to fundamental differences between Attenborough's predictions and the numerical results for the model porous equations.

However, it is clear that the values found by the numerical impedance tube technique used here are certainly close enough so that one can infer that the air-porous boundary is working correctly. Real impedance tube data taken from outdoor measurements have quite a bit of scatter, and the values measured numerically here are within the tolerances seen in such physical experiments.

10. VERIFICATION OF THE NUMERICAL SOLUTION

This chapter demonstrates the validity of the numerical model developed in the preceding chapters. Several different types of tests were performed. First, the results of the numerical solution method described in the preceding chapters are compared to those of the Pestorius algorithm, for the case of one-dimensional propagation of electric spark pulses in the free field. This example will show that the ratio $c_o \Delta t / \Delta x$ must be about 0.25.

Next, spark pulse reflection numerical results are given for both normal and oblique incidence from a hard surface. The normal reflection simulation is compared quantitatively with an analytic result, while the oblique reflection numbers are compared qualitatively with the effects observed for explosions on a larger scale.

In addition, the influence of artificial viscosity on the numerical solutions is addressed, for both the cases of spark pulse and blast modeling. Finally, some comments are made on the value of μ_B used for the blast wave runs of the next chapter.

10.1 Electric Spark Pulses in the Free Field

Spherical spark pulses in air were used to compare one-dimensional free field propagation using the algorithms of this dissertation and the Pestorius algorithm. The absorption parameters of both programs corresponded to the ANSI standard for attenuation in the atmosphere.[118] The particular version of the Pestorius algorithm used was that of Bass, Ezell, and Raspet.[119] Although this program adds the effects of vibrational relaxation dissipation, and the current implementation of the equa-

tions of Chapter 4 does not, the frequencies included in the spark pulse were high enough to not be affected by the O_2 and N_2 relaxation effects. For all the spark calculations, μ_B was set to zero, commonly known as the Stokes assumption.[120]

The values $\rho_o = 1.21$ kg/m^3 and $c_o = 343$ m/s were used with a grid 322 x 322 bounding 0.005 to 0.045 m in d and -0.02 to 0.02 m in z where $\Delta x = 1.25\times10^{-6}$ m in the finite difference program. The constant Δt was picked as $\Delta t = 100\times10^{-9}$ s, giving $c_o \Delta t/\Delta x = 0.2744$, appropriate for the algorithms of Chapter 7. The pulse was started with the initial peak pressure of $\Delta p_o = 20{,}000$ Pa or 180 dB referenced to 20 μPa at 0.03 m from $d = z = 0$. The values of t_+, τ, t_1, t_2, and t_3 were given in Chapter 6, $\tau = 40\times10^{-6}$ s, for example. The pulse was propagated for 400×10^{-6} s, corresponding to $4000\Delta t$.

To follow the pulse, the windowing capability of the program was employed in the d direction. Numerical receivers were placed at $z = 0.0$ and $d = 0.03$, 0.057447, 0.08488, 0.11232, and 0.13976 m to correspond to the placement of the receivers in the Pestorius algorithm. An artificial viscosity coefficient of $\nu = 0.08$ was used, and the simulation took 18.56 min on a Cray-2 supercomputer.

The solid lines in Figures 10.1 to 10.5 show the results of this run while the dashed lines provide the results of the Pestorius algorithm. Figure 10.1 gives the initial conditions. Note that the initial conditions for the two programs are not exactly the same, therefore their propagation should not be exactly alike. As Figures 10.2 to 10.5 show, the pulse shape becomes closer to the letter N as it

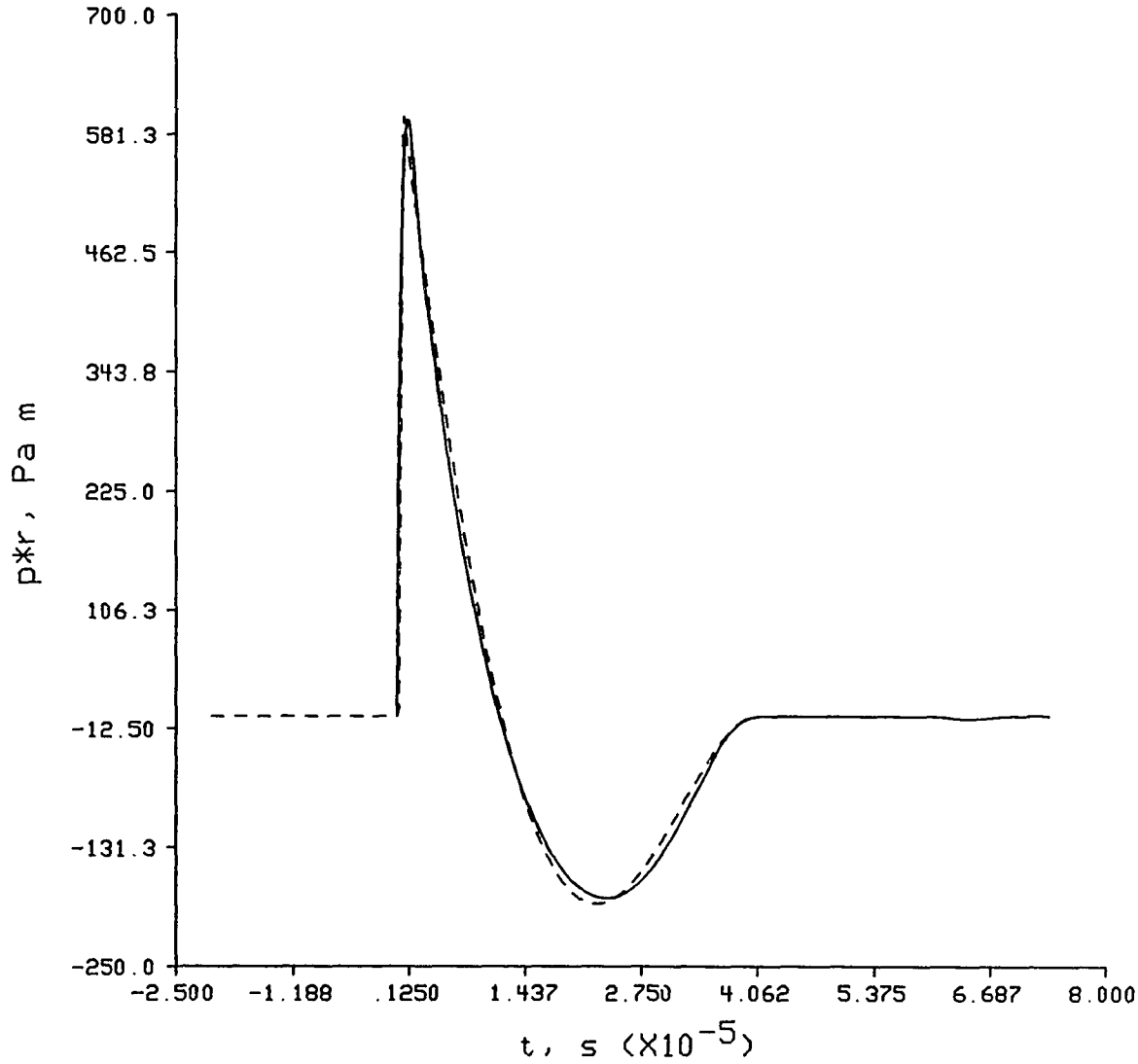

Figure 10.1. A free field spherical spark pulse propagating in air. The solid lines are the finite difference results, and the dashed lines are from the Pestorius algorithm. Time is given relative to a wave traveling at 343 m/s. Initial conditions at d = 0.03 m.

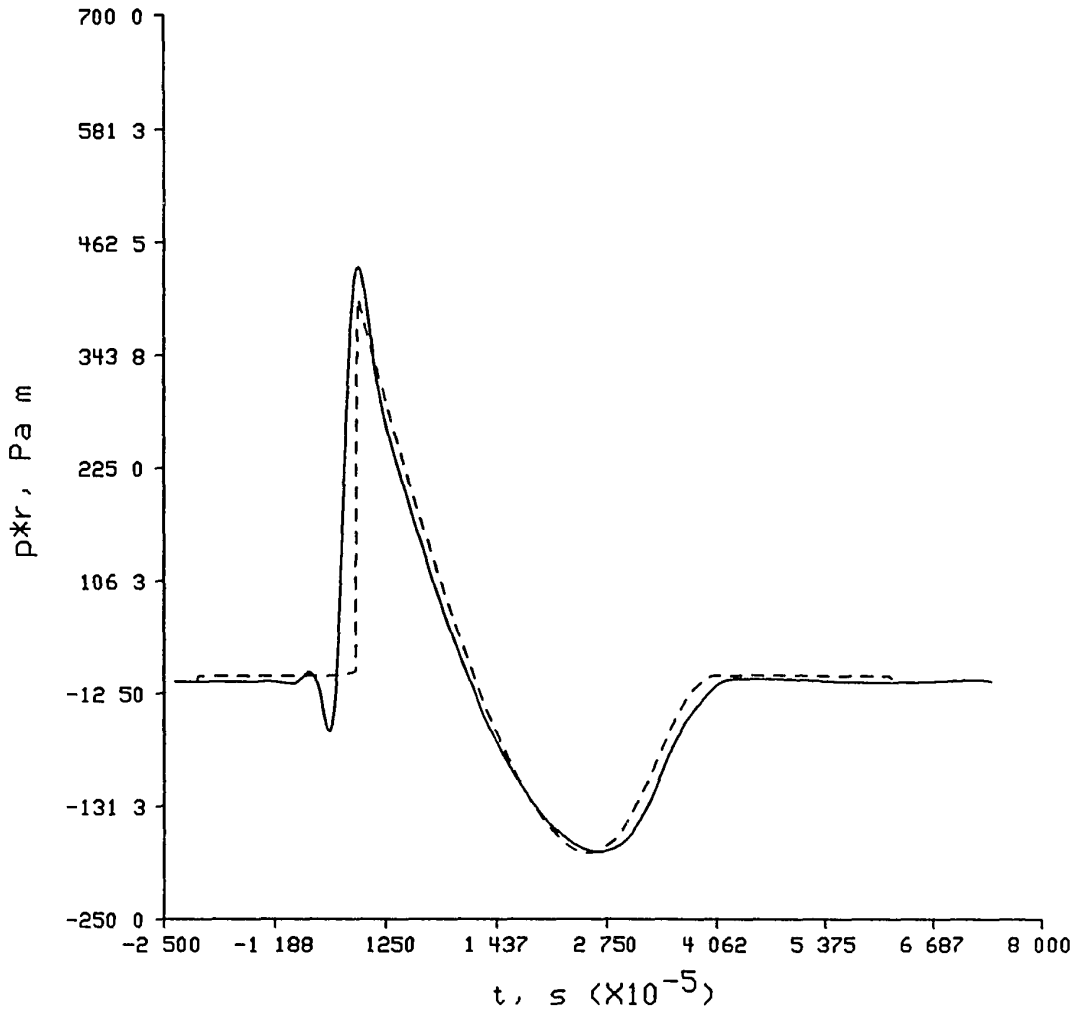

Figure 10.2. Same as Figure 10.1 at $d = 0.05744$ m.

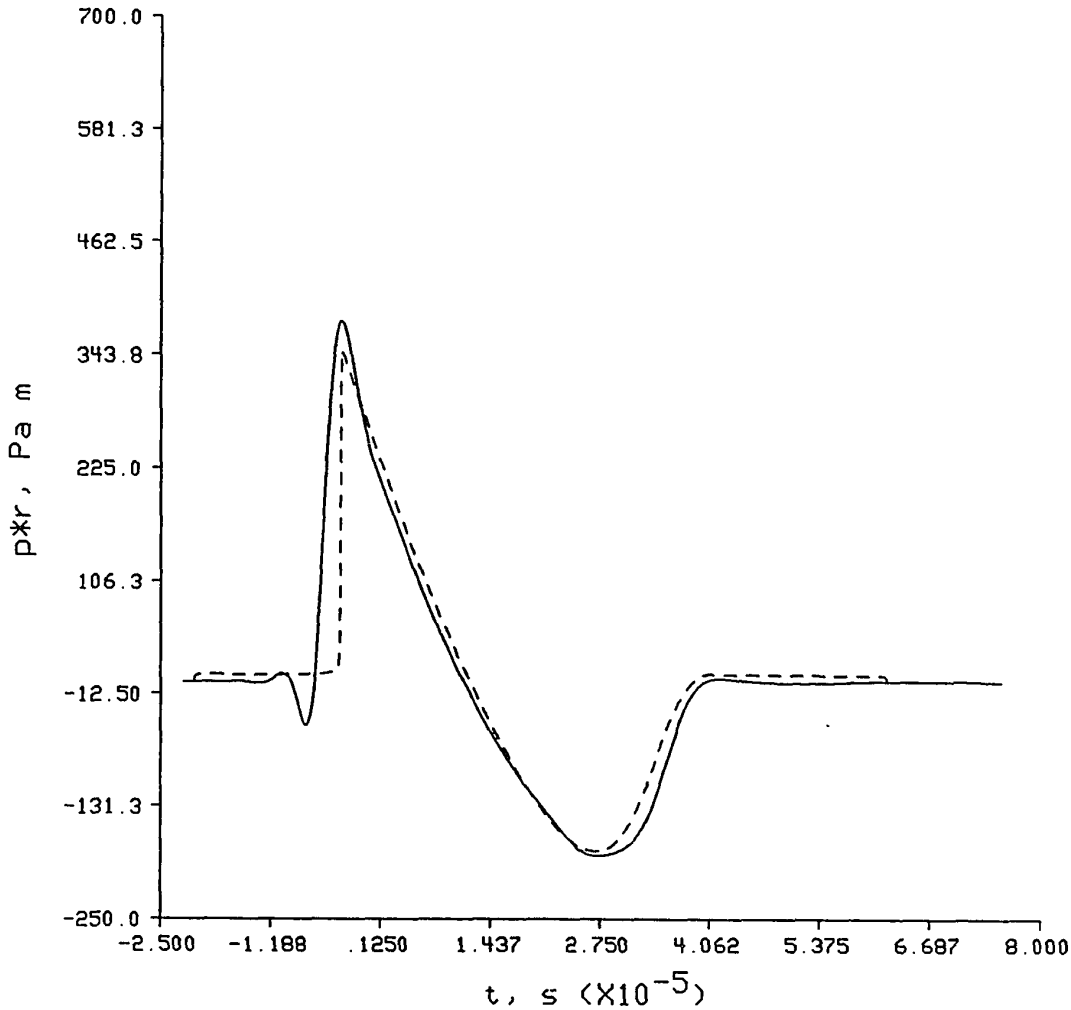

Figure 10.3. Same as Figure 10.1 at $d = 0.08488$ m.

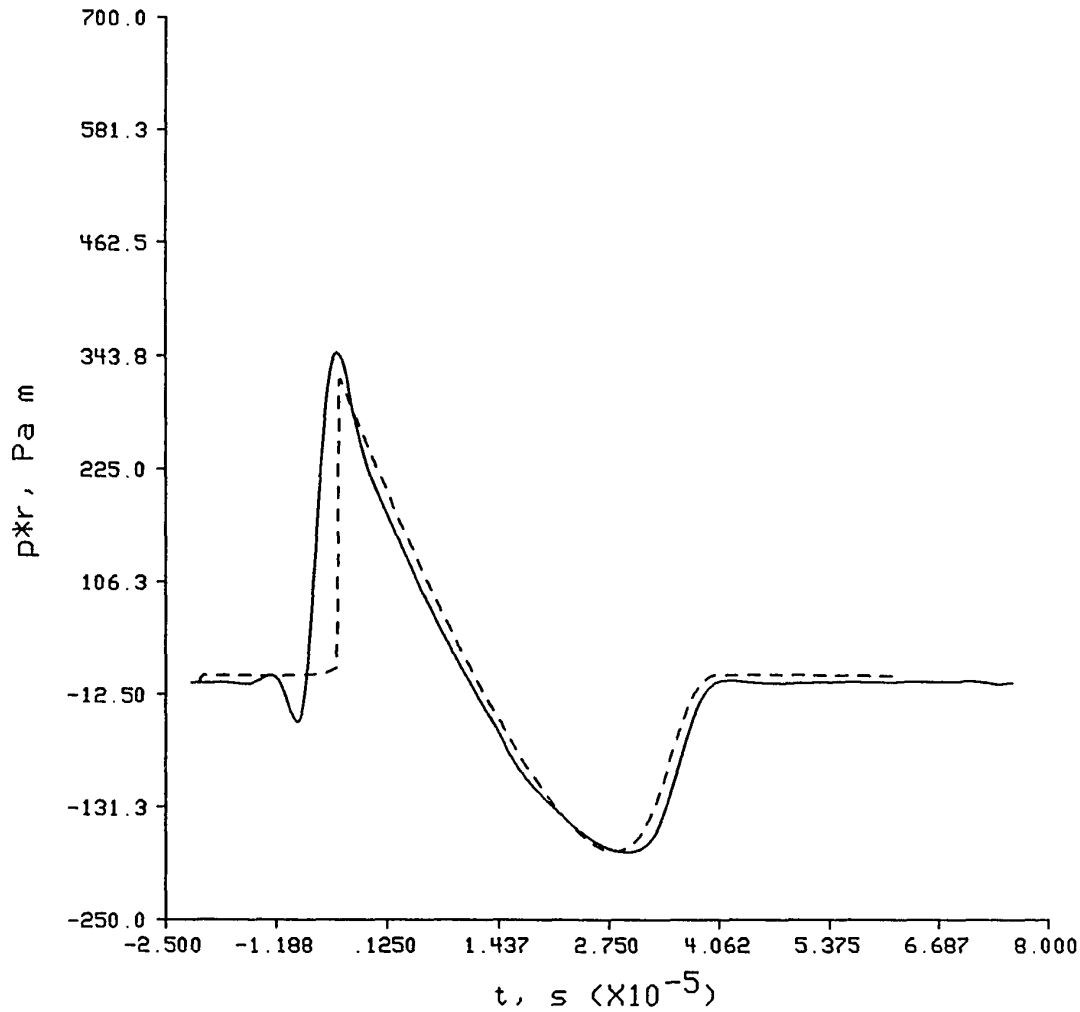

Figure 10.4. Same as Figure 10.1 at $d = 0.11232$ m.

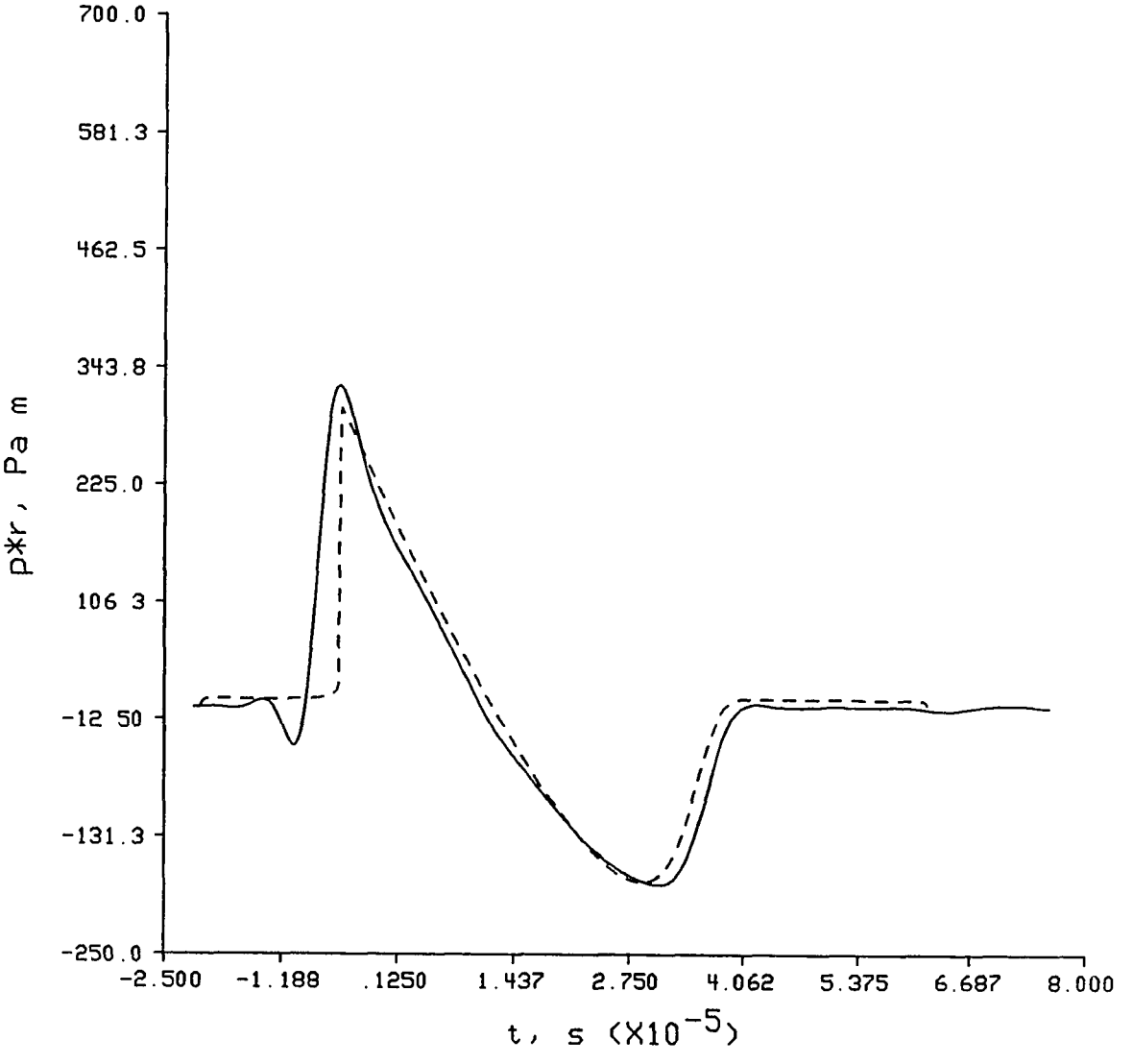

Figure 10.5. Same as Figure 10.1 at $d = 0.13976$ m.

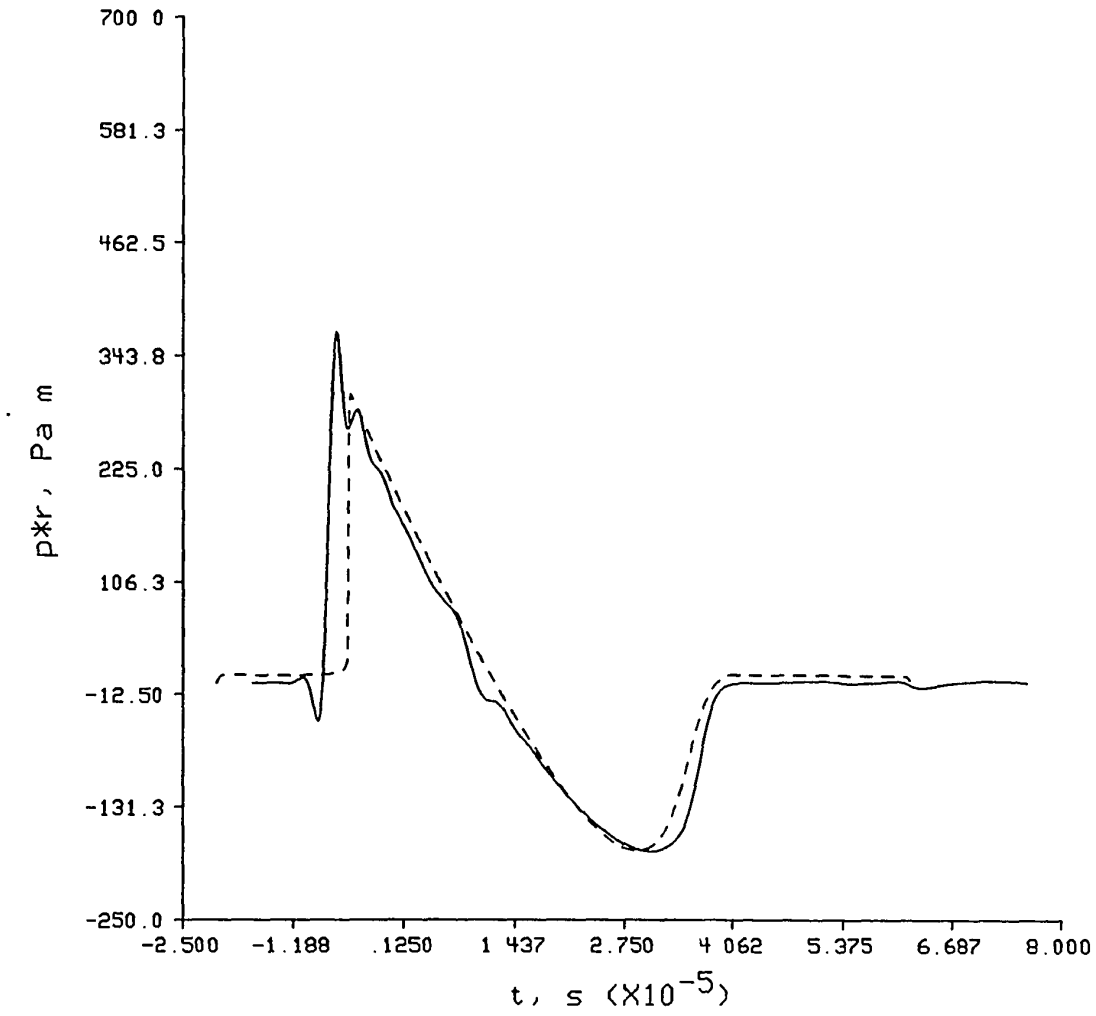

Figure 10.6. Same as Figure 10.1 at $d = 0.13976$ m, with no artificial viscosity.

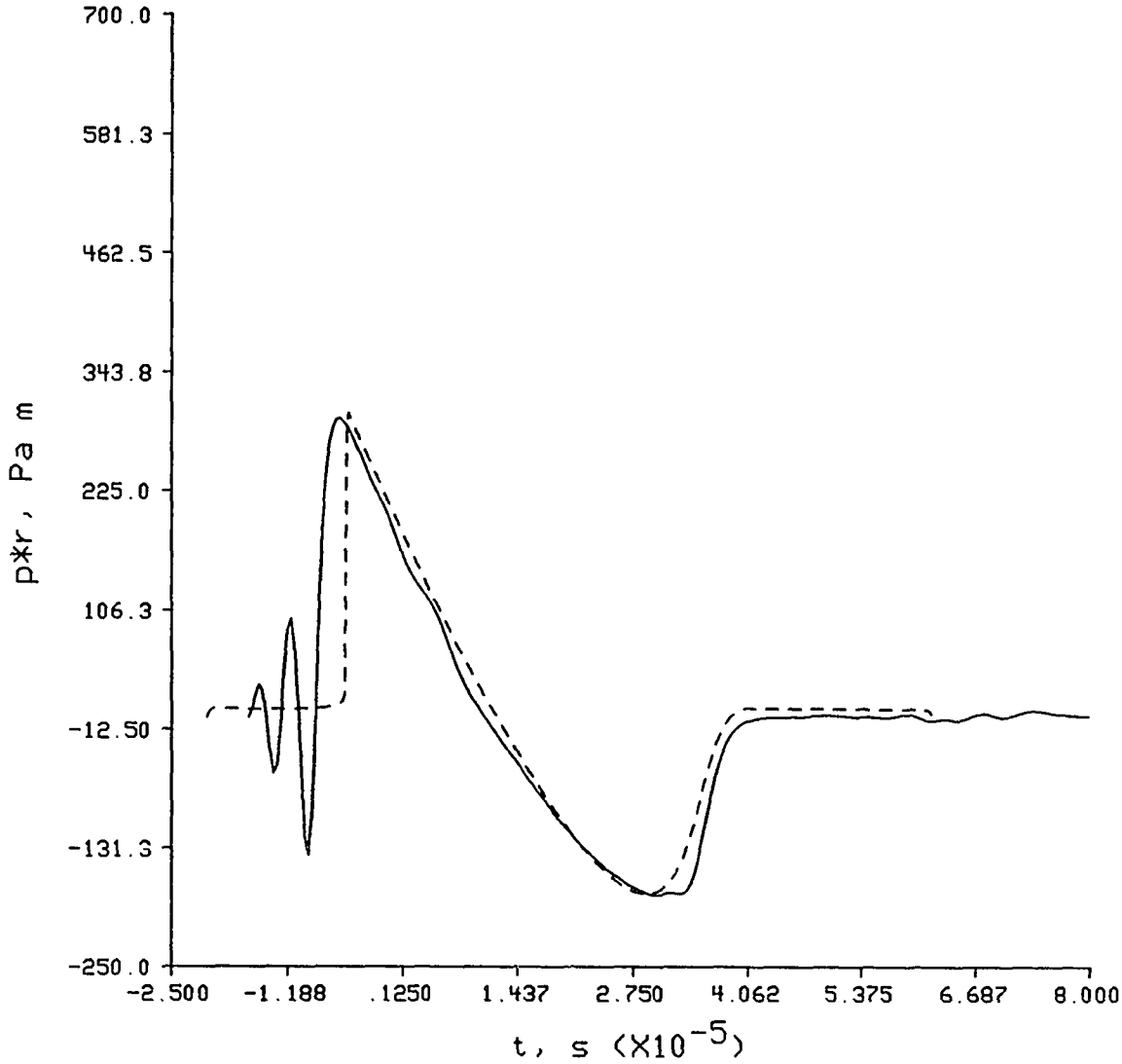

Figure 10.7. Same as Figure 10.1 at $d = 0.13976$ m, with $c_o \Delta t/\Delta x = 0.5488$ and no artificial viscosity.

propagates. This is the well known nonlinear phenomenon of propagation speed being a function of amplitude. The positive acoustic pressures travel faster than the sound speed c_0, while the negative acoustic pressures travel slower than c_0, according to Equation (2.13) of Chapter 2. Most of the nonlinear steepening occurs early in the propagation, since the distortion is a function of amplitude which is falling off as $1/r$.

It is obvious that the agreement between the finite difference program and the Pestorius algorithm is good. The pulses lengthen at about the same rate, and the amplitude dependence is similar. This indicates that the amounts of nonlinearity and absorption seen in the two programs were nearly the same. Notice, however, that the finite difference program takes into account all the second-order nonlinear effects, while the Pestorius algorithm uses only the β plane wave nonlinear effects. Thus, the spherical pulse, started in the free field, should not propagate exactly as the Pestorius algorithm dictates. This may account for some of the difference between the two results. The negative pressure dip before the steep rise in pressure at the front of the pulse in the finite difference program case is a direct result of the phase dispersion mentioned in Chapter 7.

This phase dispersion increases if the artificial viscosity is removed. Figure 10.6 shows the same finite difference result at $d = 0.13976$ m as does Figure 10.5, but with $\nu = 0$. Clearly, phase dispersion produces undesirable ripples. As previously stated, this is due to the nonlinear effects generating frequencies that are too high to be well resolved by the spatial grid.

With ν set to 0, one can also see the effect of having $c_0 \Delta t/\Delta x$ too high. Figure 10.7 gives the results of another run at d = 0.13976 m, with the difference that Δt was doubled while ν = 0. For this value of Δt, $c_0 \Delta t/\Delta x$ is 0.549. The large ripples preceding the front of the spark pulse are due to the errors of the time discretization dominating the errors of the spatial discretization. It was found that artificial viscosity does little to help give a clean solution when $c_0 \Delta t/\Delta x$ is too high.

10.2 Normal Spark Pulse Reflection from a Hard Surface

This section gives the results of the program for finite amplitude electric spark pulse normal reflection from an infinite, flat, hard surface boundary. An analytic result exists for this case which will be used for comparison.

For normal plane reflection from a hard surface, Pfriem has derived the pressure amplification factor

$$a = \frac{\left[\left(\frac{p_i}{p_o}\right)^{1/\chi} - 1\right]^{\chi} - 1}{\frac{p_i}{p_o} - 1} \tag{10.1}$$

where p_o is atmospheric pressure, p_i is the incident total pressure (atmospheric pressure plus acoustic pressure), and $\chi = 2\gamma/(\gamma - 1)$ where γ is the ratio of specific heats.[121] Here a gives the ratio of the acoustic pressure near a hard surface when a wave reflects to the acoustic pressure with the surface absent as the wave passes by. The expression is derived under the assumption of an ideal gas, and is easy to compute since, for air, $\chi = 7$. In the linear limit a equals 2, the familiar result of pressure doubling.

By making two runs of the finite difference program, one with a hard surface and one without, the ratio of pressures was found and a predicted. The program was run in the free field for the initial peak pressures of 154, 160, 168, 174, and 180 dB on the domain $5.005 \leq d \leq 5.085$ and $-0.02 \leq z \leq 0.02$ m. The peak of the pulse was placed 5.03 meters from the origin initially to make the propagation nearly plane. Here, all the computational boundaries used the absorbing or characteristic conditions of Chapter 8. Then, for the same initial conditions, the domain $5.005 \leq d \leq 5.045$ and $-0.02 \leq z \leq 0.02$ meters was used where the boundary $d = d_{\max} = 5.045$ meters was changed to be hard. This hard boundary was implemented in finite difference notation as

$$\rho'^{n}_{i=I,j} = \rho'^{n}_{i=I-1,j} \tag{10.2}$$

$$u^{n}_{i=I,j} = -u^{n}_{i=I-1,j} \tag{10.3}$$

$$v^{n}_{i=I,j} = v^{n}_{i=I-1,j} \tag{10.4}$$

$$s_{fr_{i=I,j}}{}^{n} = s_{fr_{i=I-1,j}}{}^{n} \tag{10.5}$$

for all j where $1 \leq i \leq I$.

Condition (10.2) merely represents the continuity of density, or pressure in the linear limit. Equation (10.3) implies that the hard wall does not move as the wave impinges on it. Equation (10.4) is not required physically, but is required numerically due to the Strang method of splitting in the numerical technique of Chapter 7. Lastly, condition (10.5) represents the continuity of T', from the equations of state (4.9) and (4.10).

Both 162 × 162 ($\Delta x = 250\times10^{-6}$, $\Delta t = 200\times10^{-9}$, and $\nu = 0.01$) and 322 × 322 ($\Delta x = 125\times10^{-6}$, $\Delta t = 100\times10^{-9}$, and $\nu = 0.08$) runs were used in the predictions of α. Figure 10.8 gives the Pfriem result as a solid line showing α as a function of the free field incident peak pressure in dB referenced to 20μ Pa. The filled circles in this figure are the results for the 162×162 runs of the program, and the filled squares are for the 322×322 runs. The programs measured the peak pressures encountered at $z = 0$ and $d = 5.045 - (\Delta x/2)$ m when the hard surface was present or absent, and these numbers were compared to obtain α. Notice that the peak pressures in the free field and hard surface runs do not occur at the same times. The peaks of the finite amplitude waves travel at speeds proportional to their amplitudes, which are different for the two runs.

The agreement between the Pfriem result and the finite amplitude result is generally very good. This is despite the fact that the Pfriem result assumes lossless propagation, and the finite difference calculation accounts for classical absorption effects. The 322×322 predictions seem to deviate from the Pfriem result as the incident peak pressure approaches 180 dB. It is difficult to tell how much of this manifestation is due to the phase dispersion of the numerical scheme and how much is due to the second-order lossy nonlinear equations from Chapter 4 beginning to break down at the high reflected pressures, on the order of 186 dB. If the problem is due to phase dispersion, one should be able to obtain better agreement by adjusting the artificial viscosity and by using a finer grid.

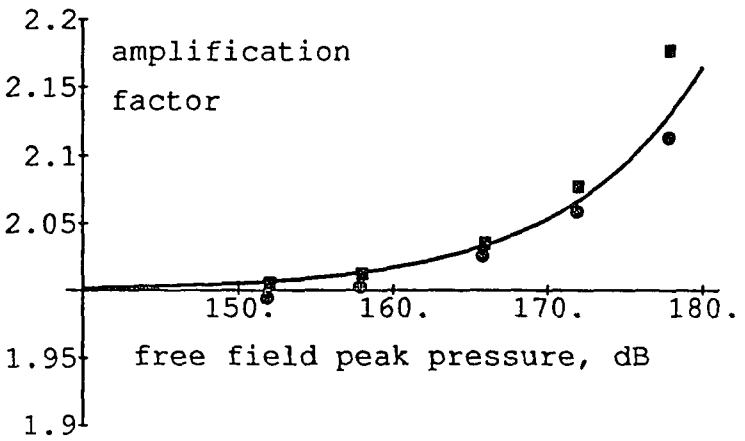

Figure 10.8. Normal reflection amplification factor versus free field incident peak pressure in dB referenced to 20 μPa for sparks. The solid line is the Pfriem result. The circles and squares are the finite difference results for a coarse (162×162) and a finer (322×322) grid run, respectively.

10.3 Oblique Spark Pulse Reflection from a Hard Surface

Notice that the verification calculations presented thus far, free field spherical propagation and plane wave normal reflection, could have been performed with a one-dimensional program. There would have been a significant decrease in CPU time and memory usage for a one-dimensional code. However, a two-dimensional nonlinear effect is now presented, the cumulative interaction of a spherical electric spark pulse obliquely incident on a hard surface, which cannot be computed using a one-dimensional program. There is no analytic solution to compare with the finite difference results in this case, so we will examine the qualitative agreement between the program results and what is expected from physical arguments and explosion data.

In the normal incidence plane wave case, the Pfriem equation and the numerical results gave a ranging from 2.00 to about 2.15 depending on the incident amplitude. For normal reflection, the incident and reflected components of the pulse interact over the pulse transit time. For oblique incidence, however, the incident and reflected components of the pulse can interact over much longer periods of time. Therefore, it is reasonable to expect that for oblique reflection the interacting incident and reflected components of the pulse could produce a larger or smaller than is the case with normal reflection. The amplification factor a would be smaller if the oblique incident and reflected waves destructively interfered with each other more than in the normal incidence case, and a would be larger if they constructively interfered. It also stands to reason that the interference producing deviations in a would be a function of the incident angle.

Researchers have observed this phenomenon experimentally and numerically for spherical explosion blasts incident on natural ground surfaces.[122,123,124] For explosions, a is the normal reflection result for angles near normal, increases to a peak, and then actually decreases below 2 for angles close to grazing incidence. The specific curve of a versus angle depends on the incident peak pressure.

Calculations were made to show that spark pulses have a versus angle curves similar to those for explosions. The program was run for a spherical spark pulse above a hard surface at $z = z_{\min}$ using the finite difference relations

$$\rho'^{n}_{i,j=1} = \rho'^{n}_{i,j=2} \tag{10.6}$$

$$u^{n}_{i,j=1} = u^{n}_{i,j=2} \tag{10.7}$$

$$v^{n}_{i,j=1} = -v^{n}_{i,j=2} \tag{10.8}$$

$$s_{fr_{i,j=1}}{}^{n} = s_{fr_{i,j=2}}{}^{n} \tag{10.9}$$

for all i where $1 \leq i \leq I$. These equations are similar to (10.2) to (10.5).

The spark pulses were always centered around the origin of the coordinate system initially, and the hard surface was located at $z_{\min}$ = -0.0075, -0.01125, -0.015, -0.01875, -0.0225, -0.025, -0.03, and -0.035 m. Corresponding free field runs on a larger domain with the hard surface absent were also made. Numerical receivers were placed along the ground surface or its equivalent to obtain numerical predictions. From one pair of free field and hard surface runs it was possible to obtain one point to put on each plot of a versus incident angle for each constant incident pressure. Thus, the 8 pairs of runs produced up to 8 points on each plot of a versus incident angle for fixed incident pressure.

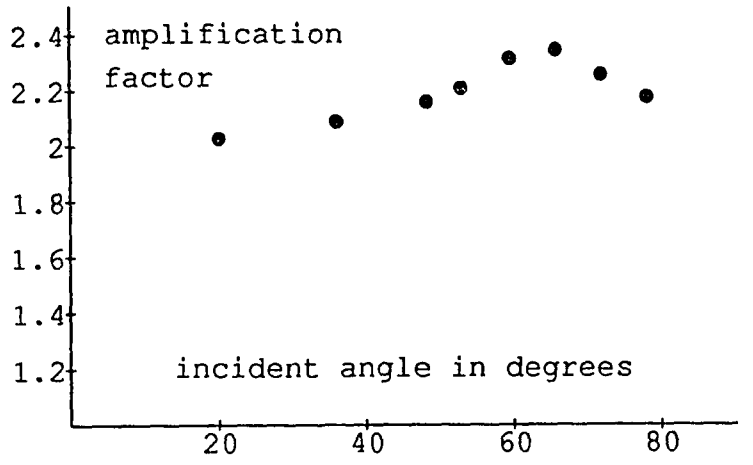

Figure 10.9. Oblique reflection amplification factor versus angle in degrees for a fixed free field incident peak pressure for sparks. When the angle is 0 degrees, the wavefront is locally normally incident, and when the angle is 90 degrees, the wavefront is locally grazing. The free field incident peak pressure is 15.0 kPa, 177.5 dB.

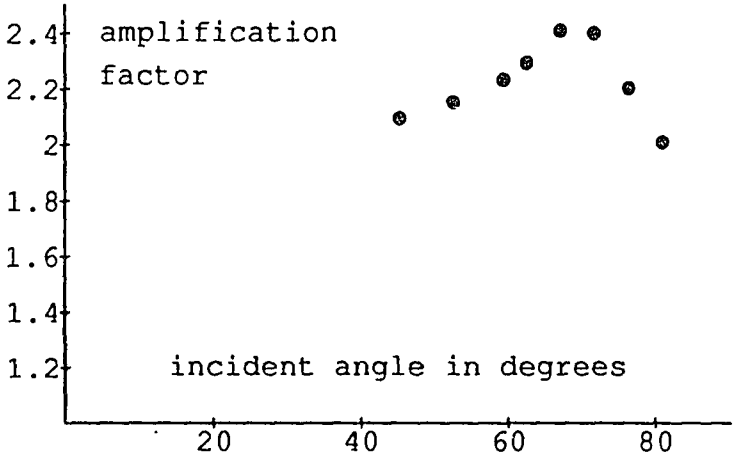

Figure 10.10. Same as Figure 10.9 except the peak pressure is 10.0 kPa, 174 dB.

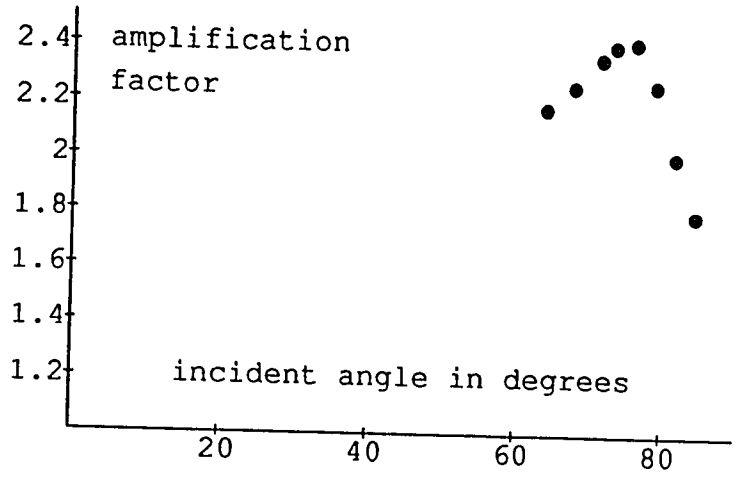

Figure 10.11. Same as Figure 10.9 except the peak pressure is 5.0 kPa, 168 dB.

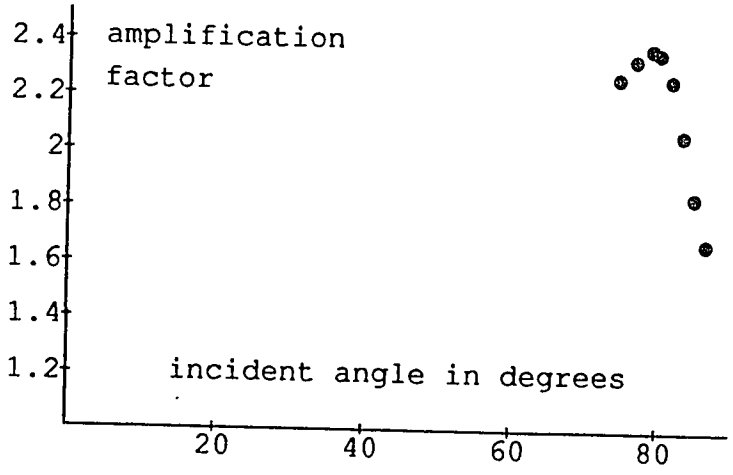

Figure 10.12. Same as Figure 10.9 except the peak pressure is 2.5 kPa, 162 dB.

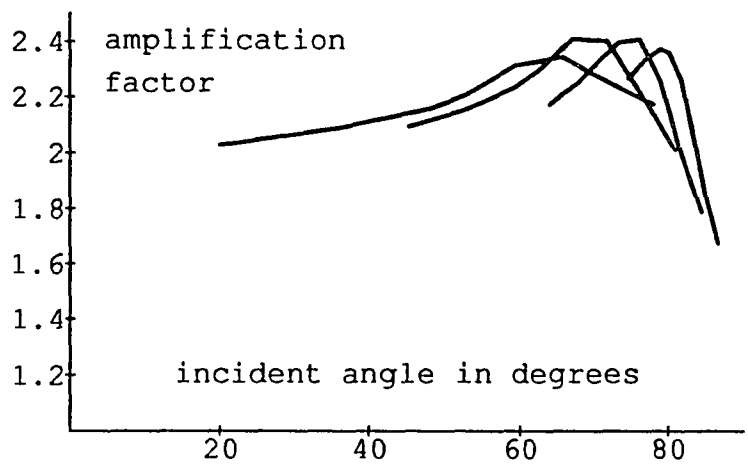

Figure 10.13. A composite of Figures 10.9 to 10.12. Oblique reflection amplification factors versus angle for the four free field incident peak pressures for sparks of 15.0, 10.0, 5.0, and 2.5 kPa.

These simulations used $\Delta x = 250\times10^{-6}$ m, $\Delta t = 200\times10^{-9}$ s, and $\nu = 0.01$ with the initial peak 0.03 m from the origin at a pressure of 180 dB. Each of the 16 runs needed between 2.34 and 5.76 min of CPU time on a Cray-2.

The individual data points in Figures 10.9 to 10.12 present the results of these runs, corresponding to peak incident pressures of 15000 Pa (177.5 dB), 10000 Pa (174 dB), 5000 Pa (168 dB), and 2500 Pa (162 dB). Figure 10.13 joins each of the numerical data points in Figures 10.9 to 10.12 and plots these curves for comparison. The results confirm the assertion that a should be a function of incident angle for each constant incident pressure. As can be seen for the 5000 Pa numbers (Figure 10.11), a is near the Pfriem normal incidence result for most small angles of incidence. The amplification factor a increases to 2.41 as the incident angle increases, and then it decreases below 2 to 1.78 or less as the angle becomes closer to grazing.

These curves are similar to those seen from explosions on a larger scale as given in the Glasstone, Kinney and Graham, and Heaps *et al.* references. This qualitative agreement between the spark and blast oblique incidence a versus incident angle curves is intuitively satisfying, but some laboratory work should be performed in the future to experimentally verify these spark oblique curves. No references to this type of experimental data have been found in the literature.

10.4 Artificial Viscosity and Bulk Viscosity Values for Blasts

Recall that $\nu = 0.08$ was used for the free field spark simulations to produce Figures 10.1 to 10.5. This value was found by trial and error, increasing and decreasing ν, until the best result was obtained. The goal was to have the minimum ν

which would still reduce the ripples produced by the phase dispersion.

Numerous calculations were made with idealized blast pulses of approximate length $\tau \approx 40\times10^{-3}$ s and various peak pressures. Computations were performed repeatedly to find optimum values of ν. It was deemed that a value of ν was good when it was the minimum value such that the drop from peak pressure to the zero crossing was monotonic, when no two values of time between the peak and the zero crossing were associated with the same value of pressure. The values that were found for $\Delta t = 200\times10^{-6}$ s and $c_0 \Delta t/\Delta x = 0.2744$ are given in Table 10.1, and the values for $\Delta t = 100\times10^{-6}$ with the same $c_0 \Delta t/\Delta x$ in Table 10.2.

These tables demonstrate that the amount of artificial viscosity needed generally increases as the peak amplitudes increase. This makes sense, since more high frequencies that the grid cannot well resolve are generated as the amplitude increases. More nonlinearity means more high frequencies, so a higher ν is needed

Table 10.1. Coarse grid minimum artificial viscosities for blasts.

Δp_o, Pa	Δp_o, dB	minimum ν
200	140	$< 1\times10^{-5}$
2000	160	1×10^{-5}
5000	168	1×10^{-5}
10,000	174	1×10^{-3}
20,000	180	5×10^{-3}

Table 10.2. Fine grid minimum artificial viscosities for blasts.

Δp_o, Pa	Δp_o, dB	minimum ν
200	140	1×10^{-4}
2000	160	2×10^{-3}
5000	168	4×10^{-3}
10,000	174	4×10^{-3}
20,000	180	1×10^{-2}

for higher amplitudes. The fact that a higher ν is needed for the finer grid also makes sense from Equation (7.24) of Chapter 7. That relationship, however, is not exactly followed, so other effects not directly considered here may be involved.

Finally, the values of μ_B used in the blast runs above should be discussed. The lossy second-order nonlinear model of Chapter 4 currently does not include the effects of molecular relaxation dissipation. Relaxation is not important for spark pulses due to their high frequency content, so μ_B was assumed negligible and set to zero for sparks. For the lower frequencies involved with blasts, however, one can increase μ_B to account for some of the energy lost by relaxation processes.

It is possible to derive an expression for the absorption due to a relaxation process in the low frequency limit, as an increment to μ_B, $\Delta\mu_B$. The expression is

$$\Delta\mu_B = \frac{2\rho_o {c_o}^2 \tau_i}{\pi} (\alpha_i \lambda)_m \tag{10.10}$$

where τ_i is the ith relaxation time and $(\alpha_i\lambda)_m$ is the maximum absorption per wavelength associated with the ith relaxation process.[125]

If one looks at a chart of absorption coefficient α versus f for air such as Figure 10-13 in Pierce's book, it is obvious that two relaxation processes in air, O_2 and N_2, primarily control absorption at low frequencies. Unfortunately, using the low frequency limit for both these processes would make the absorption too high for frequencies in the range 100 to 1000 Hz. Using too high an absorption would severely affect the peak sound pressure levels observed at long ranges.

The finite difference numerical method described in Chapter 7 already has some intrinsic dissipation, to which an artificial fourth-order viscosity was added. To keep the peak sound pressure levels as accurate as possible, the minimum additional bulk viscosity was sought. Such peak levels are dominated by the high frequency absorption. If the low frequency limit of the O_2 relaxation process alone is used, the absorption for the high frequencies in the blast pulse turns out to be about right, and this technique was employed. Oxygen has a relaxation frequency at f_i = 12,500 Hz.

For the O_2 bulk relaxation effect $(\alpha_i \lambda)_m$ is 0.0011 and $\tau_i = 1/(2\pi f_i) = 12.732 \times 10^{-6}$ and $\Delta\mu_B$ is 1.27×10^{-3} using $c_o = 343$ and $\rho_o = 1.21$. Although μ_B is usually assumed zero, experimental evidence has shown it to have the value $\mu_B = 0.6\mu$ for air. To this value $\Delta\mu_B$ was added, giving $\mu_B = 0.6\mu + \Delta\mu_B = 1.281 \times 10^{-3}$, which is about 70 μ.

11. FINITE AMPLITUDE BLAST PREDICTIONS

This section presents the findings of this dissertation on the propagation of finite amplitude blast sounds outdoors. Throughout, the emphasis is on the oblique reflection of blast sounds from hard surfaces and from the porous medium model of a ground surface presented in Chapters 5 and 9. For a particular charge size and geometry three runs were made. The first run was in the free field with no reflective surface present. The second run introduced the hard surface ground, while the third used the porous medium ground. This chapter will first give the results for a wide variety of angles of incidence, corresponding to one charge at various heights. Then, to investigate propagation near the ground, the geometry will be held fixed for differently sized charges.

11.1 A Fixed Charge Weight at Various Heights.

Numerous runs at various heights were made that would have had a peak free field pressure of 180 dB at 30 m from the source. Looking at Table 6.1, a 180 dB pulse at 30 m is 183.89 ms long in time, or equivalently, approximately 63 m in space. This spatial dimension implies that for the initial conditions of this dissertation the wave cannot be within 63 m of the origin. For the runs made here, the initial condition used was a spherical 183.89 ms pulse that had a peak of 8,571.4 Pa 70 m from the origin. This new peak makes the gross linear assumption that between 30 m and 70 m, the wave fell off as $1/r$ and did not distort. These calculations were made with different domains, depending on the heights of the sources. For each run the artificial viscosity used was $\nu = 5\times10^{-3}$ with a coarse grid of $\Delta t = 200\times10^{-6}$

s and $\Delta x = 0.250$ m. The three programs each took approximately 19 to 30 min on a Cray-2 for each height investigated.

Graphs were developed giving the amplification factor a as a function of incident angle for a fixed incident pressure. As in the last chapter, a is the ratio of the acoustic pressure received near the reflection surface to the pressure at the same receiver with the reflection surface removed. The source heights used to obtain the numerical predictions were 1, 11, 21, 31, 41, 51, and 61 m. Figures 11.1, 11.2, 11.3, and 11.4 give the resulting hard surface amplification factor versus angle plots for the fixed incident free field peak pressures of 9000, 5000, 2500, and 1250 Pa, respectively. Figure 11.5 presents composite graphs when all the discrete data points from Figures 11.1 to 11.4 are joined by lines.

These hard surface amplification factor versus incident angle plots show two major results. First, the amplification factors are up to 2.65 for the blast runs, whereas they were up to only 2.4 for the hard oblique runs of electric spark reflections in the last chapter. Secondly, the hard surface curves of a versus incident angle are also more peaked for the blasts in Figure 11.5 than for the sparks in Figure 10.13. This difference in hard oblique incidence amplification factors between sparks and blasts indicates that these reflections do not scale simply.

Similarly, the oblique porous run results for amplification factors appear in Figures 11.6 to 11.10. In general, these results are more peaked and the peaks are more toward grazing incidence compared to the hard cases. It is unwise to directly

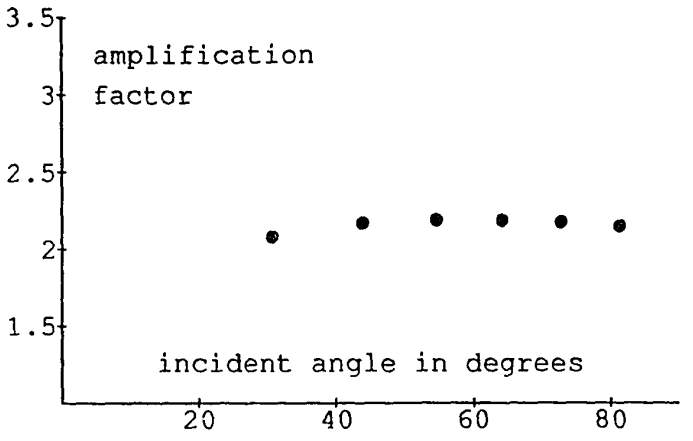

Figure 11.1. Oblique hard reflection amplification factor versus angle in degrees for a fixed free field incident peak pressure for blasts. When the angle is 0 degrees, the wavefront is locally normally incident, and when the angle is 90 degrees, the wavefront is locally grazing. The free field incident peak pressure is 9.0 kPa, 173 dB.

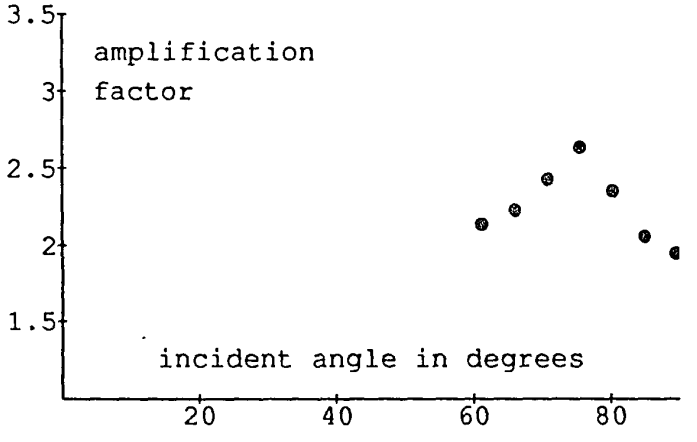

Figure 11.2. Same as Figure 11.1 except the peak pressure is 5.0 kPa, 168 dB.

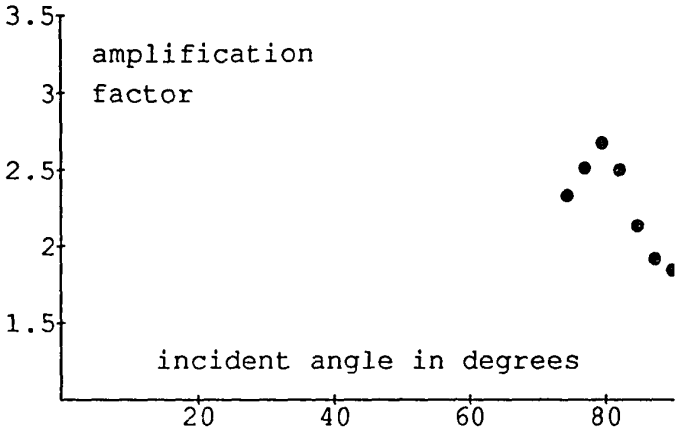

Figure 11.3. Same as Figure 11.1 except the peak pressure is 2.5 kPa, 162 dB.

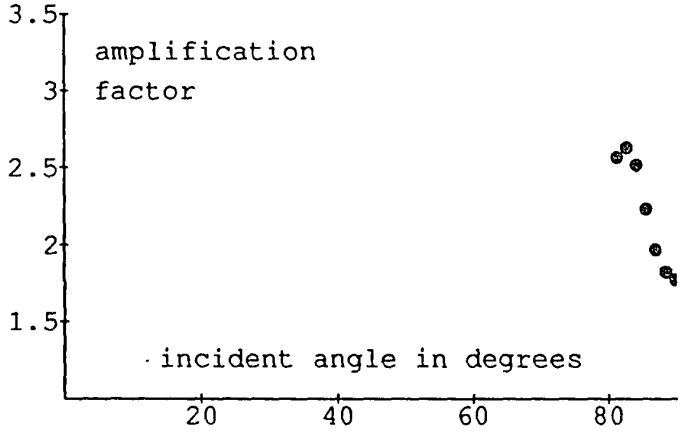

Figure 11.4. Same as Figure 11.1 except the peak pressure is 1.25 kPa, 156 dB.

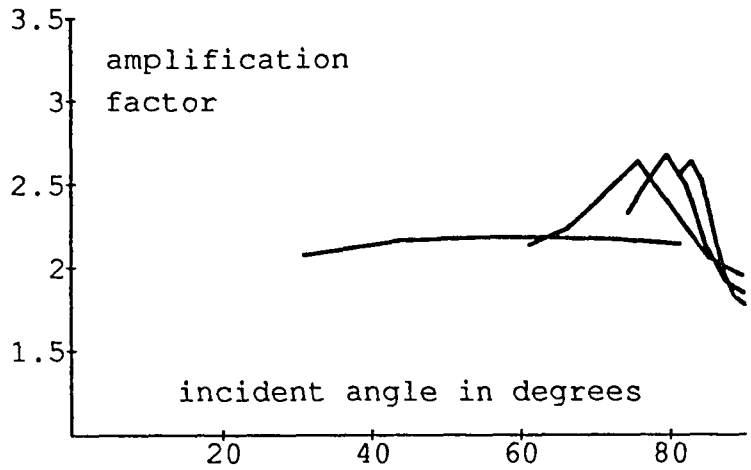

Figure 11.5. A composite of Figures 11.1 to 11.4. Oblique hard reflection amplification factors versus angle for the four free field incident peak pressures for blasts of 10.0, 5.0, 2.5, and 1.25 kPa.

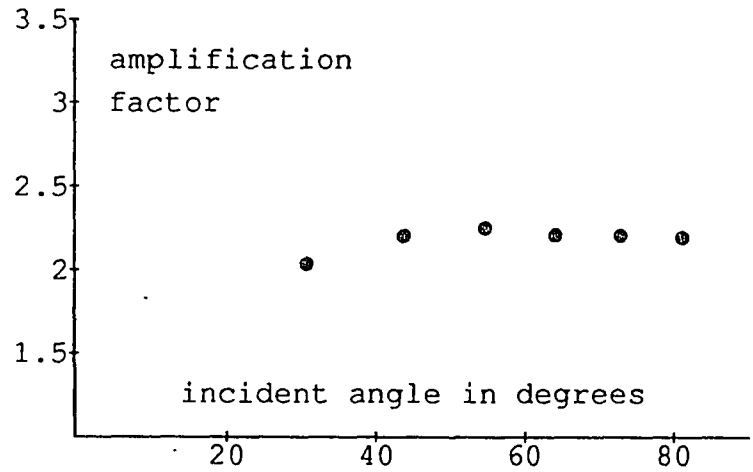

Figure 11.6. Oblique porous reflection amplification factor versus angle in degrees for a fixed free field incident peak pressure for blasts. When the angle is 0 degrees, the wavefront is locally normally incident, and when the angle is 90 degrees, the wavefront is locally grazing. The free field incident peak pressure is 9.0 kPa, 173 dB.

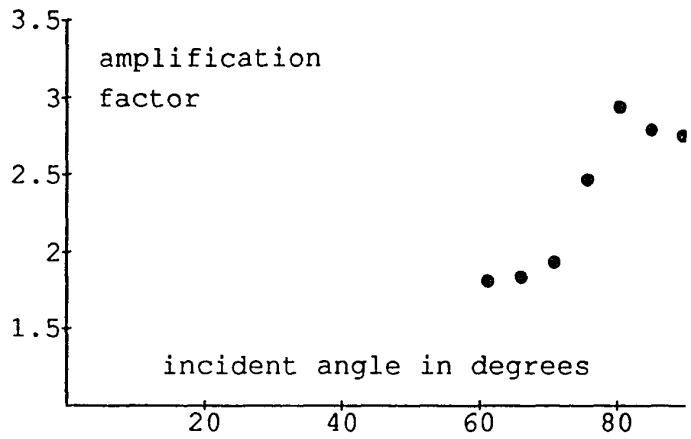

Figure 11.7. Same as Figure 11.6 except the peak pressure is 5.0 kPa, 168 dB.

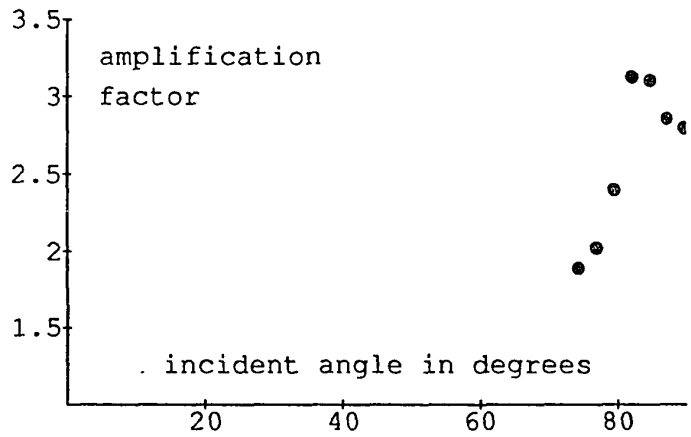

Figure 11.8. Same as Figure 11.6 except the peak pressure is 2.5 kPa, 162 dB.

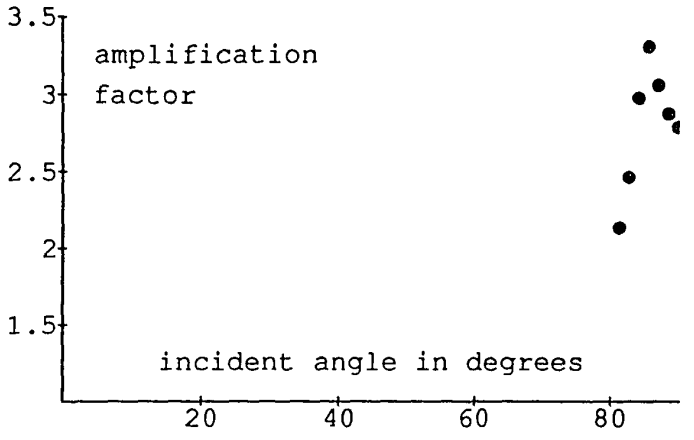

Figure 11.9. Same as Figure 11.6 except the peak pressure is 1.25 kPa, 156 dB.

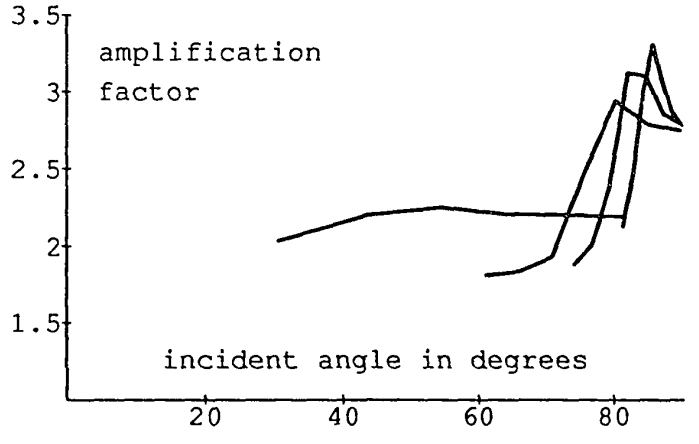

Figure 11.10. A composite of Figures 11.6 to 11.9. Oblique porous reflection amplification factors versus angle for the four free field incident peak pressures for blasts of 10.0, 5.0, 2.5, and 1.25 kPa.

compare the actual amplification factors between the hard and porous cases, however, since the initial conditions for the two cases are approximate.

The a versus angle curves developed here are similar to the strong shock calculation results of Heaps *et al.* and the curves in Glasstone's work, *The Effect of Nuclear Weapons*. These authors do not use the notation used in this thesis, however. For comparison Heaps *et al.* call a the reflected overpressure/P, while Glasstone merely refers to it as the reflected overpressure ratio $\bar{P}_r/\bar{P}_s$ where $\bar{P}_s$ is given in atmospheres. The similarity of the curves presented in this thesis to the curves of the Heaps *et al.* and Glasstone references shows that the numerical method of this thesis is accurately predicting the oblique incidence of blast waves.

11.2 Different Charge Sizes at Near Grazing Incidence.

Many runs were made with source heights of 1 m with various initial peak pressures to see the effect of a varying charge size for a fixed geometry. Runs with initial peak pressures corresponding to 180, 174, 168, 162, 156, and 150 dB at 30 m were carried out. The 180 dB and 174 dB cases were performed using initial peaks of 8,571.4 Pa at 70 m and 7,500 Pa at 40 m, respectively, since these larger blasts could not be started at 30 m. The pulse initial durations and corresponding charge sizes of C-4 plastic explosive are listed in Table 5.1.

Receivers at 30, 45, 60, 90, 120, 180, 240, 360, 480, 720, and 960 m from the source at heights of 0, 1, 2, and 5 m recorded the waves as they propagated, as well as all maximum pressures encountered near the ground. These free field, hard surface, and porous surface runs were made using the artificial viscosities of Table

10.2, or interpolated values thereof, with $\Delta t = 100 \times 10^{-6}$ s and $c_0 \Delta t / \Delta x = 0.2744$. The 150 dB, 156 dB, and 162 dB peak runs were propagated for 0.4 or 0.2 s. The 168 dB run modeled propagation for 0.8 s, the 174 dB run for 1.6 s, and the 180 dB run for 3.2 s. The shorter programs took about 20 min on a Cray-2, while the largest programs took 5 h or more of Cray-2 CPU time apiece. The 180 dB runs were particularly expensive computationally because of the large physical size the blast pulse occupied, and their computation would not be possible using something other than a state of the art supercomputer (as of 1990).

The resulting 150, 162, and 174 dB peak SPL versus range plots for propagation near the hard surface are presented in Figures 11.11 to 11.13, respectively. In these figures the 0 m receiver height peaks are given by the solid lines, the 1 m receivers by the short dashed lines, and the 5 m receivers by the long dashed lines. The 156, 168, and 180 dB results were similar. The curves show that although the peak sound pressure levels are initially different at the different heights, this goes away quickly, and there is no difference in level as a function of height further out. The peak levels all fall off near the rate of $r^{-1.2}$, 7.23 dB per doubling of distance, which is given on these figures as a solid line denoted by "ref." This $r^{-1.2}$ reference line is started at 170 dB at 20 m and extends to 640 m.

This decay rate of approximately $r^{-1.2}$ agrees with the empirical relation given by Reed for weak shocks in the far field of a strong blast.[126] The finite difference simulation, therefore, is making predictions consistent with the weak shock region of a strong shock calculation.

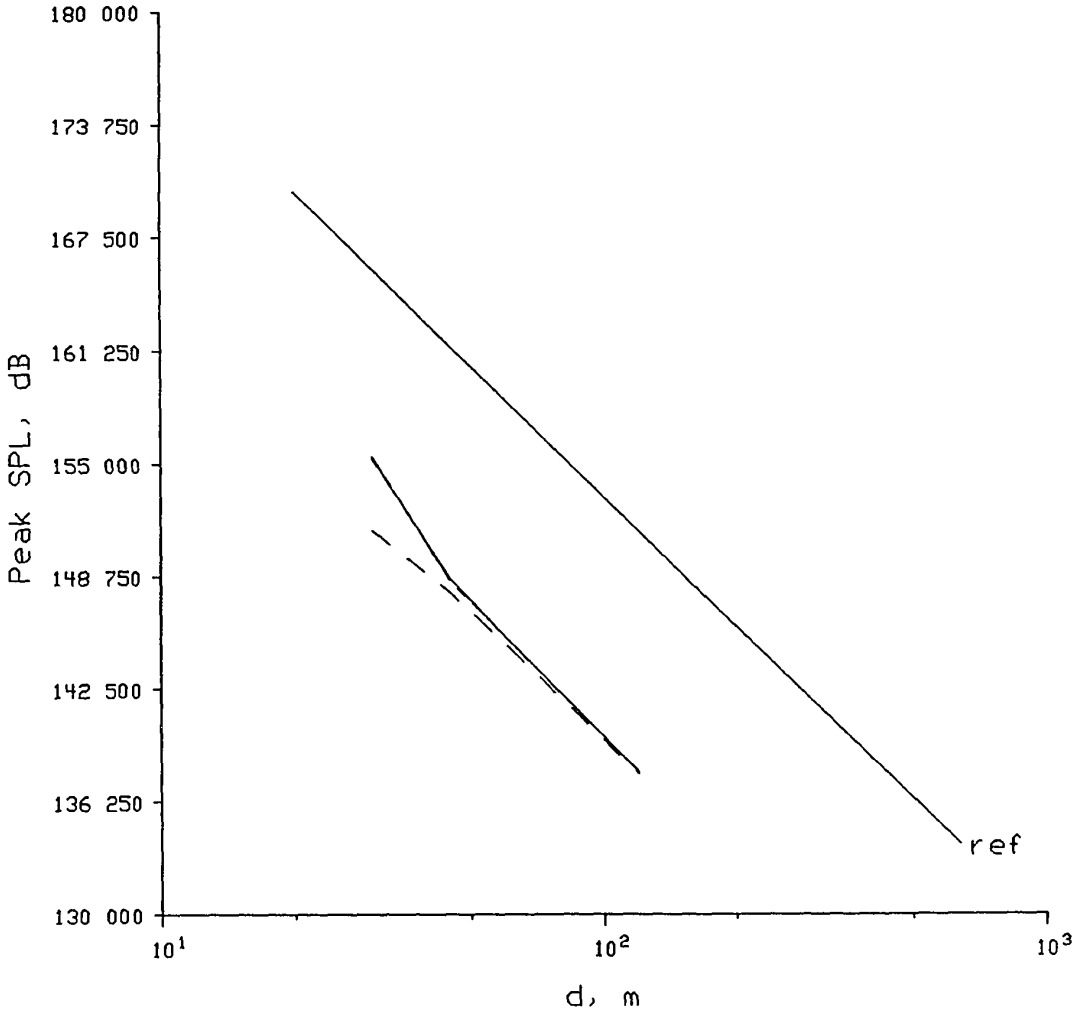

Figure 11.11. 150 dB initial peak pressure SPL versus range for hard surface propagation. The 0 m receiver height is given by the solid line, the 1 m height by the short dashed line, and the 5 m height by the long dashed line. The solid line ending with the label "ref." shows a decay of $r^{-1.2}$ for reference.

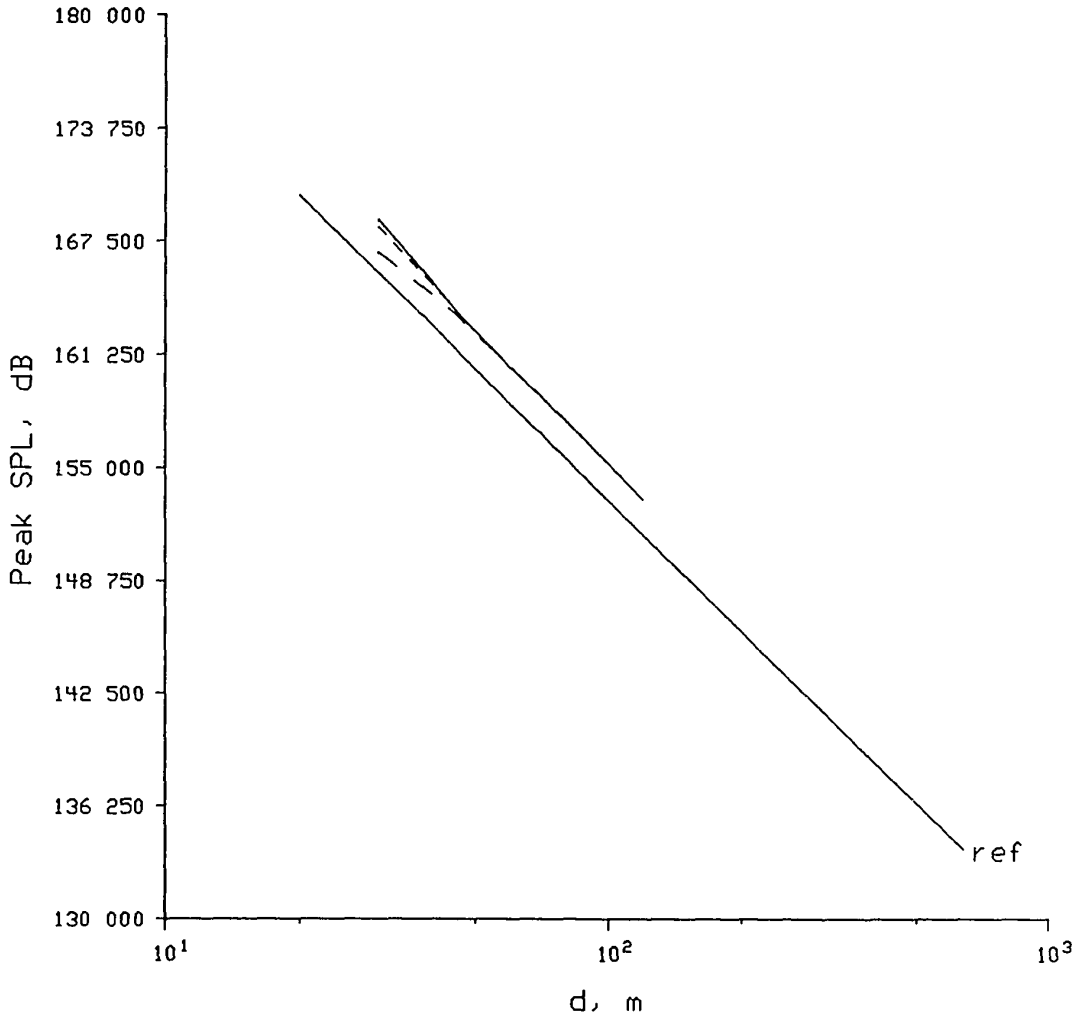

Figure 11.12. 162 dB initial peak pressure SPL versus range for hard surface propagation. The 0 m receiver height is given by the solid line, the 1 m height by the short dashed line, and the 5 m height by the long dashed line. The solid line ending with the label "ref." shows a decay of $r^{-1.2}$ for reference.

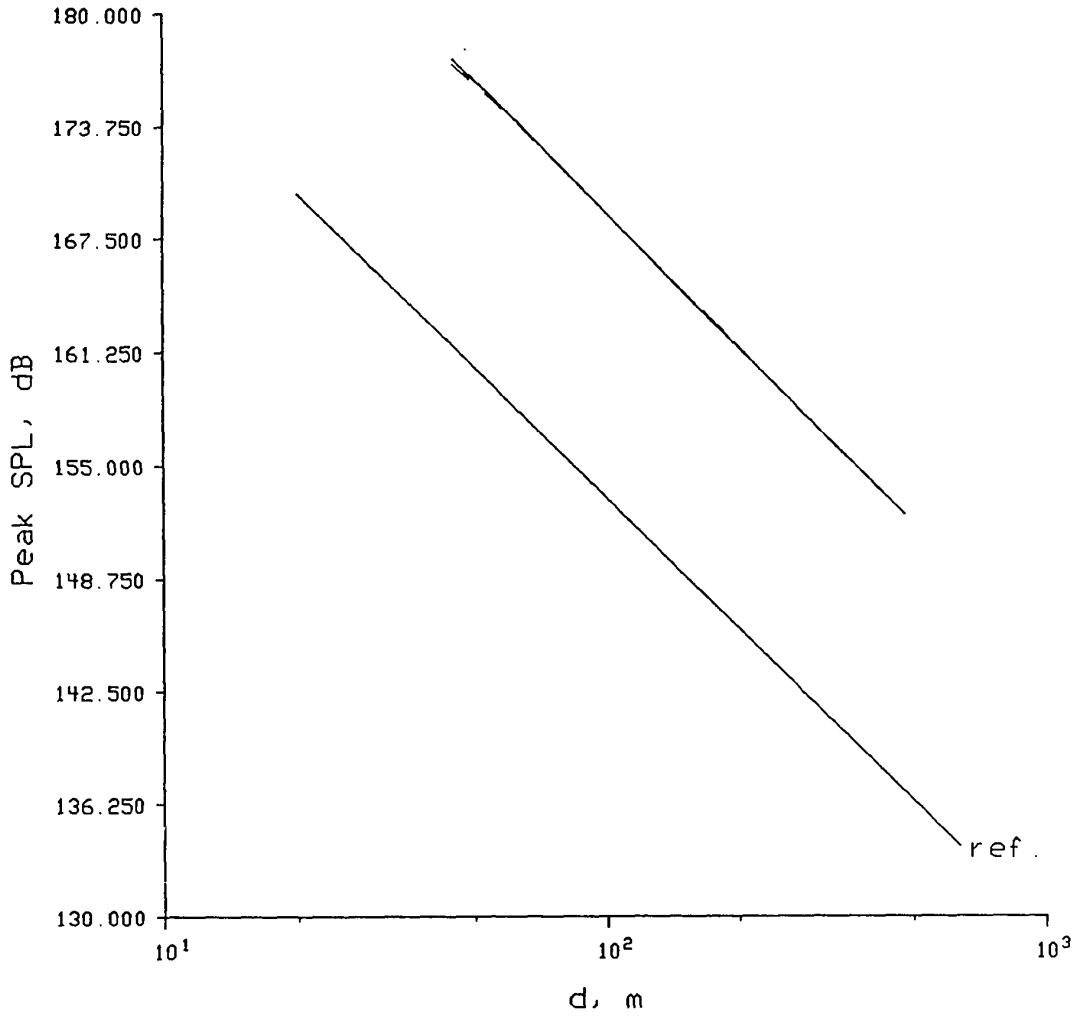

Figure 11.13. 174 dB initial peak pressure SPL versus range for hard surface propagation. The 0 m receiver height is given by the solid line, the 1 m height by the short dashed line, and the 5 m height by the long dashed line. The solid line ending with the label "ref." shows a decay of $r^{-1.2}$ for reference.

Figures 11.14 to 11.19 show the hard ground numerical receiver pressure versus time curves at 120 m range for a 150 dB peak free field initial pressure at a 0 m height, 150 dB peak at 5 m, 162 dB peak at 0 m, 162 dB peak at 5 m, 174 dB peak at 0 m, and 174 dB peak at a 5 m height, respectively. The 150 dB plots show much dispersion and absorption, while the 162 dB plots show less, and the 174 dB even less than that. As is expected the "shock" is more pronounced at the higher amplitudes. Little difference is seen in the waveforms between when the numerical receiver is near ground level and when the receiver is at a 5 m height.

The porous simulation peak SPL versus range plots for 150, 162, and 174 dB are given in Figures 11.20 to 11.22. Again, the results for 156, 168, and 180 dB peak sound pressure levels were similar. For this porous case the plots show a marked difference in peak levels as a function of height, compared to the hard simulations which showed little difference. The peak sound pressure levels were always the greatest near the porous surface. This effect may seem counterintuitive, but is due to the near grazing geometry used here and the particular impedance of the porous surface, i.e., a high magnitude impedance with phase angle of $\pi/4$.

For the 0 m receiver height the porous peak levels decayed at about $r^{-1.2}$, except for the 150 dB initial peak run which fell off faster. This rate of $r^{-1.2}$ is what was seen for the hard surface runs. However, for increasing initial peak pressure, the sound pressure levels at the 5 m height decayed at a rate less than $r^{-1.2}$ and those at the 1 m height even less than that. Comparing Figure 11.13 (174 dB, hard) to Figure 11.22 (174 dB, porous) after the simulation settles down, it is clear that the slopes of the curves for the 0 m height cases are nearly identical.

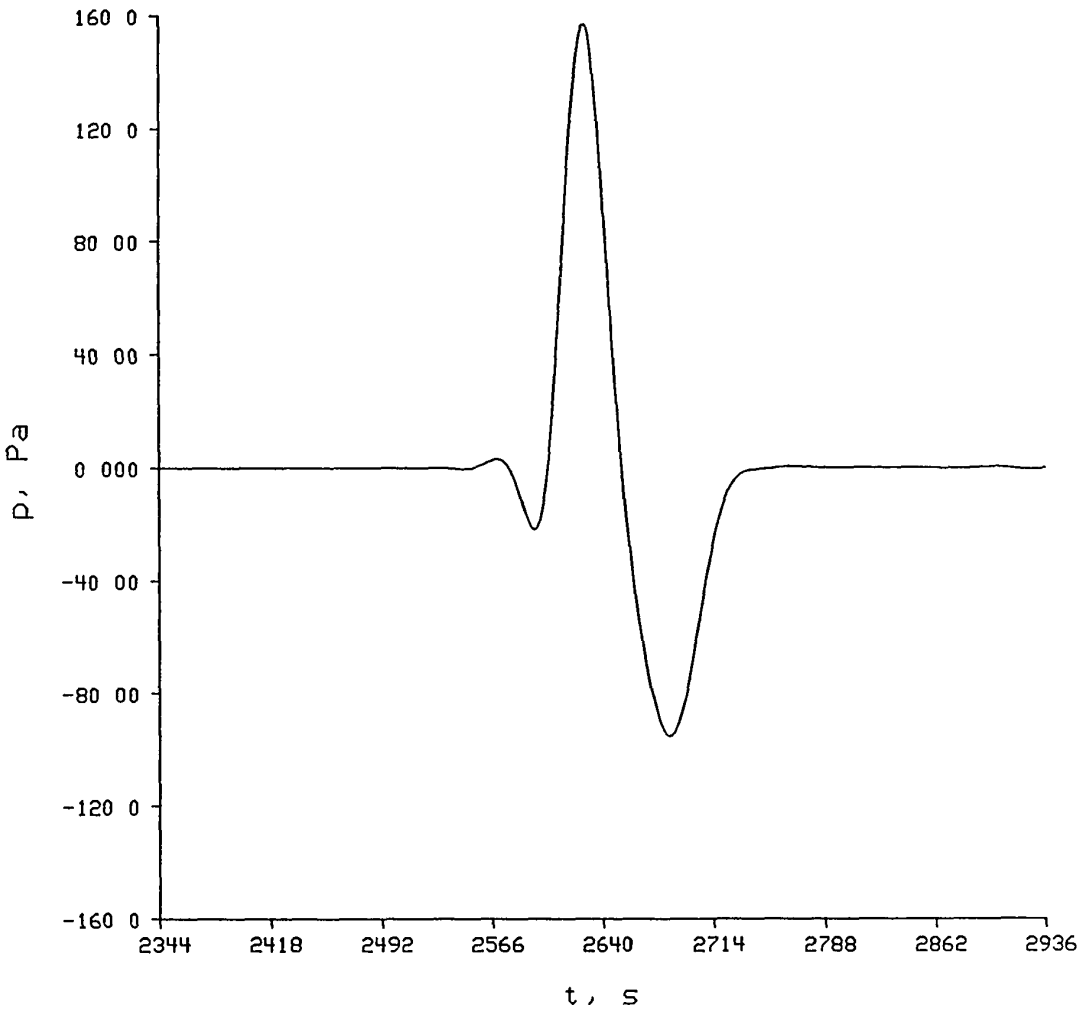

Figure 11.14. Pressure versus time at the 120 m range and the 0 m receiver height for a 150 dB initial peak blast propagating over the hard surface.

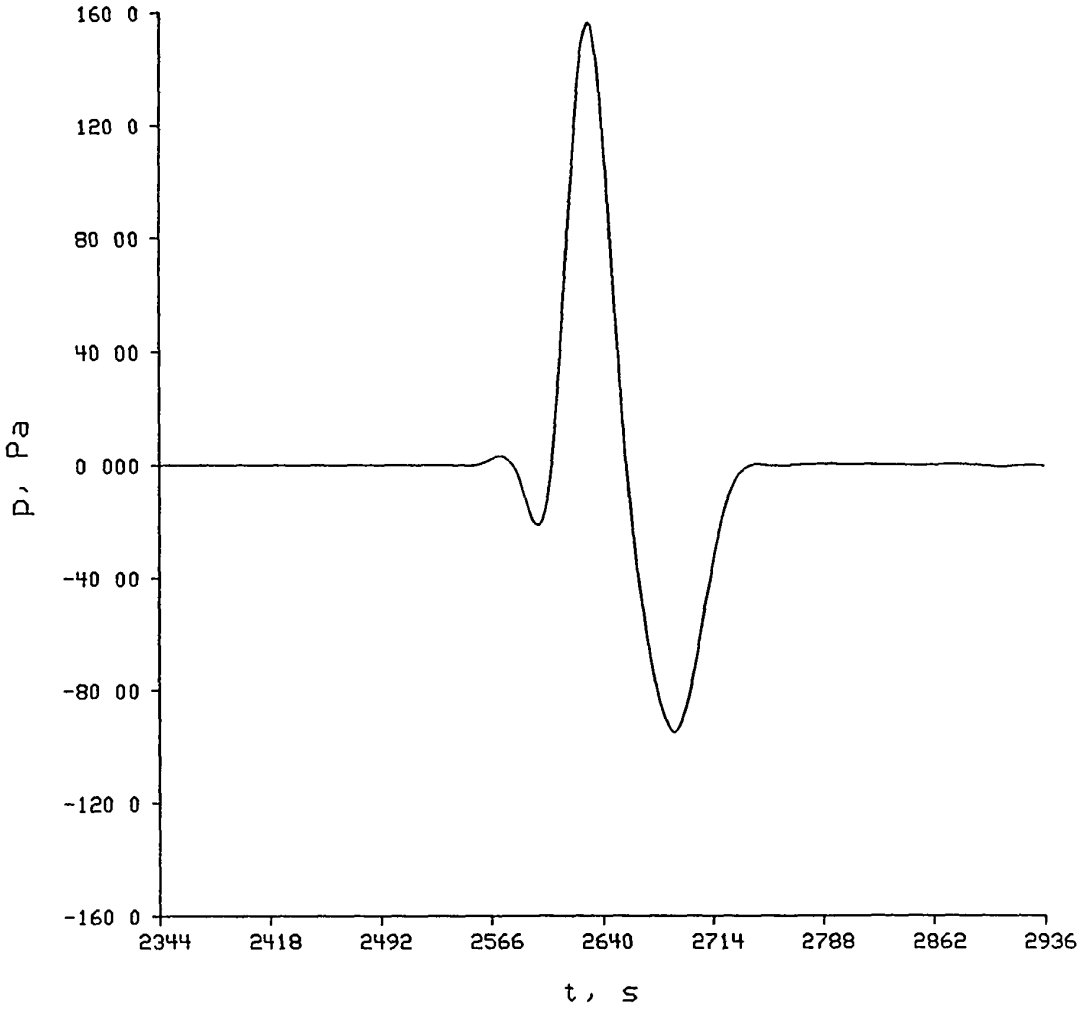

Figure 11.15. Pressure versus time at the 120 m range and the 5 m receiver height for a 150 dB initial peak blast propagating over the hard surface.

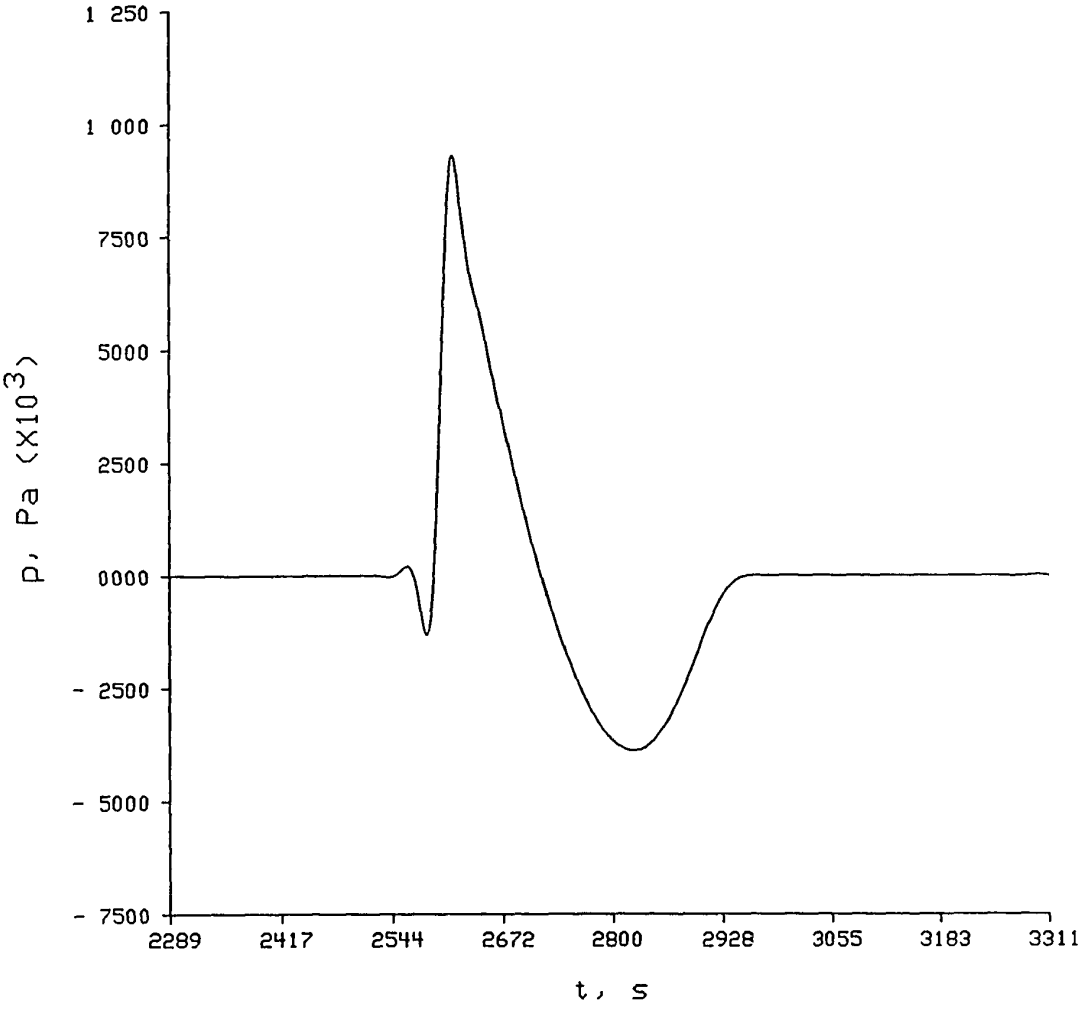

Figure 11.16. Pressure versus time at the 120 m range and the 0 m receiver height for a 162 dB initial peak blast propagating over the hard surface.

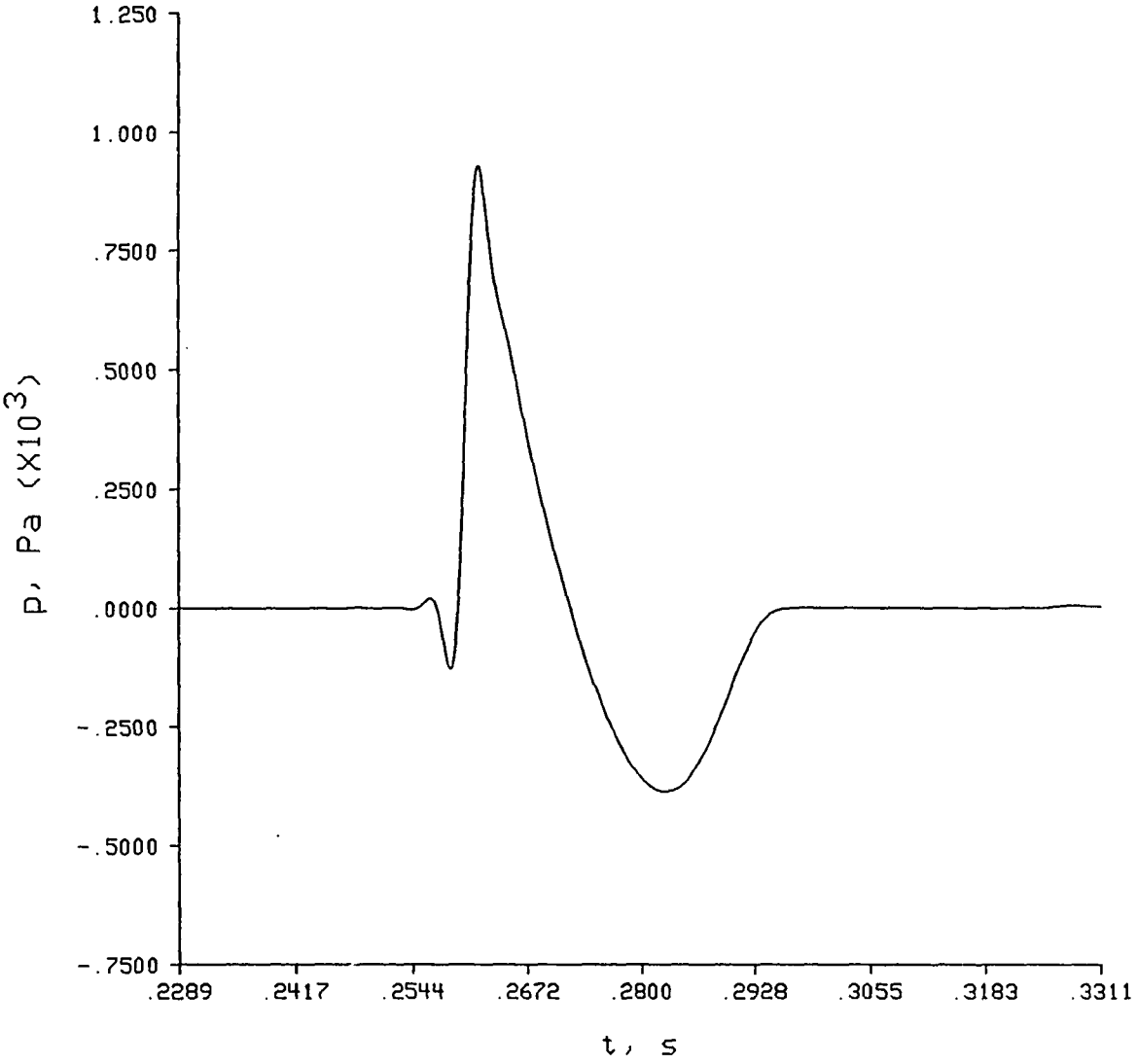

Figure 11.17. Pressure versus time at the 120 m range and the 5 m receiver height for a 162 dB initial peak blast propagating over the hard surface.

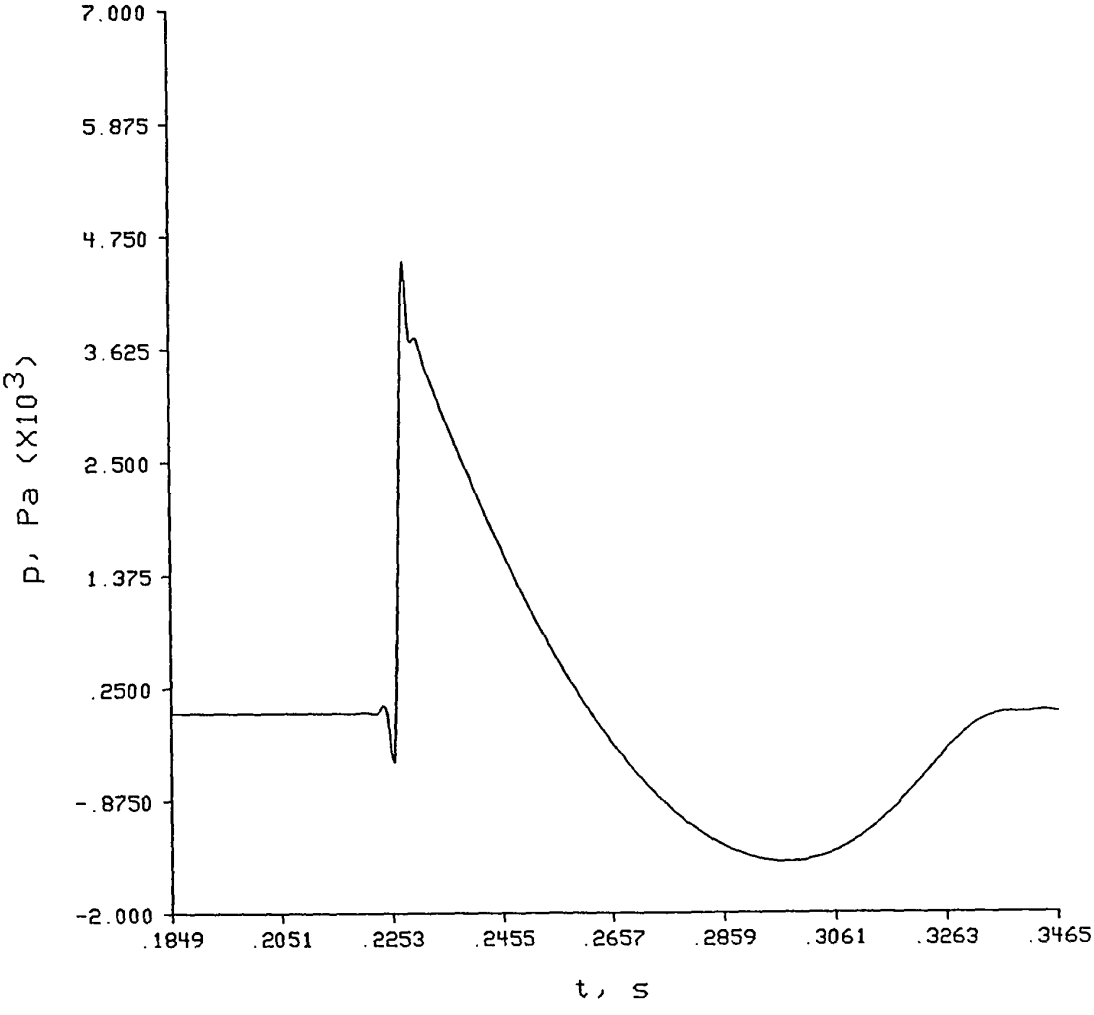

Figure 11.18. Pressure versus time at the 120 m range and the 0 m receiver height for a 174 dB initial peak blast propagating over the hard surface.

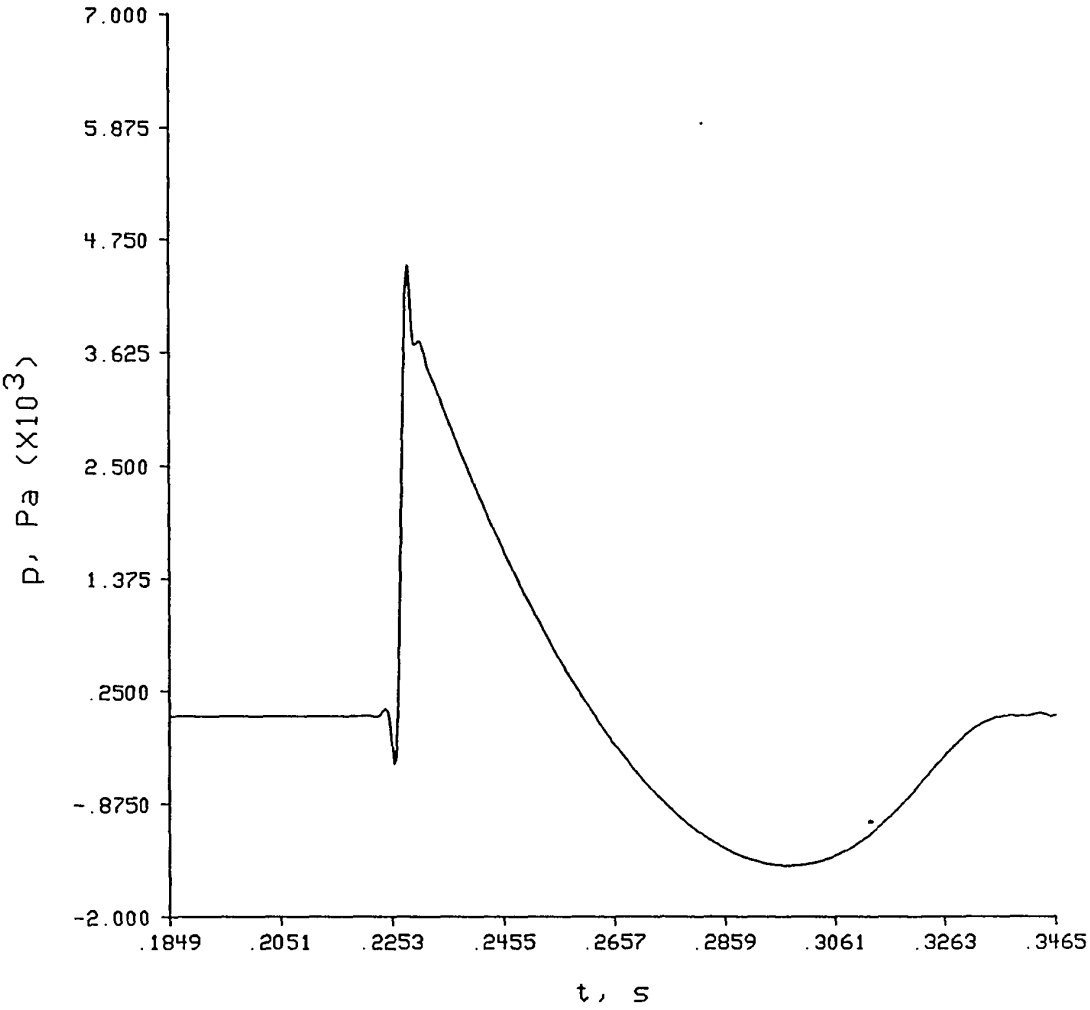

Figure 11.19. Pressure versus time at the 120 m range and the 5 m receiver height for a 174 dB initial peak blast propagating over the hard surface.

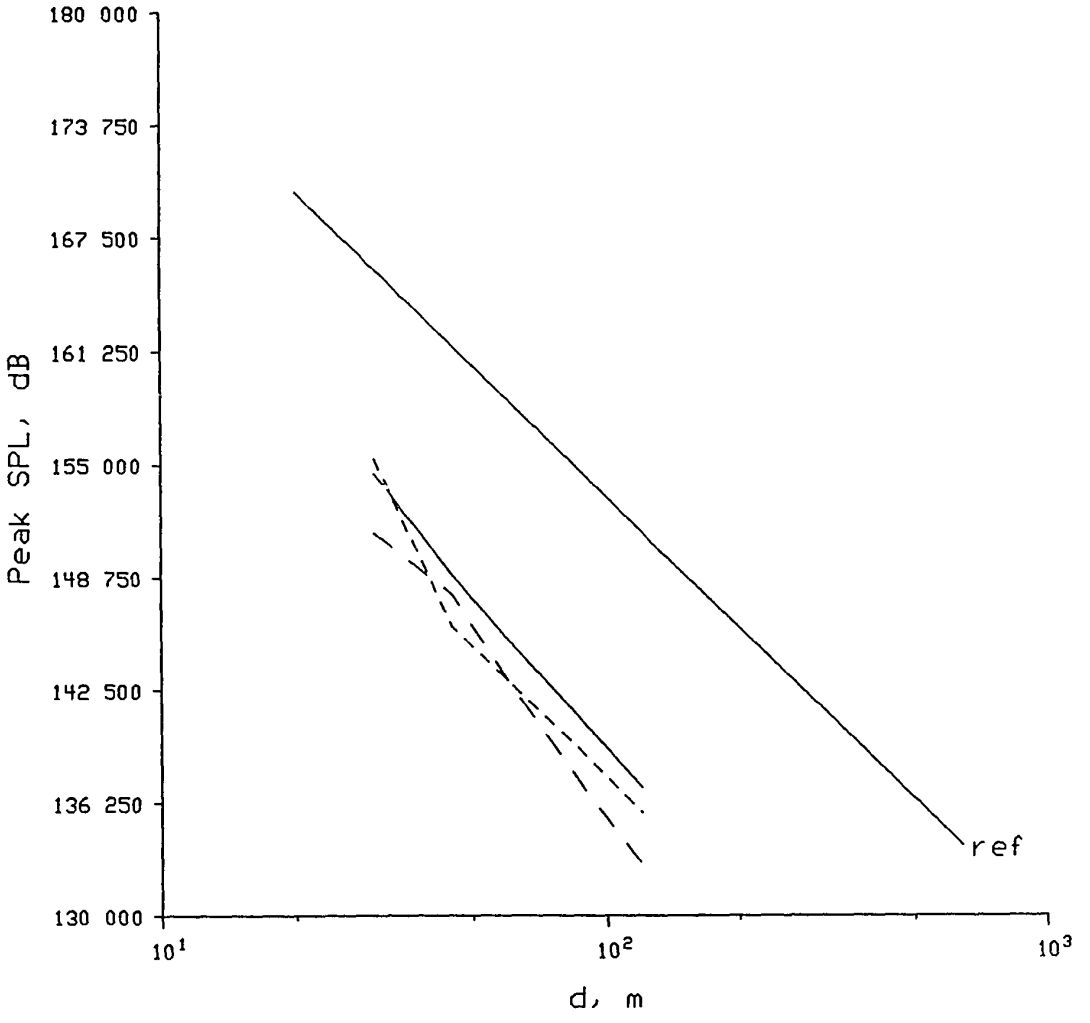

Figure 11.20. 150 dB initial peak pressure SPL versus range for porous surface propagation. The 0 m receiver height is given by the solid line, the 1 m height by the short dashed line, and the 5 m height by the long dashed line. The solid line ending with the label "ref." shows a decay of $r^{-1.2}$ for reference.

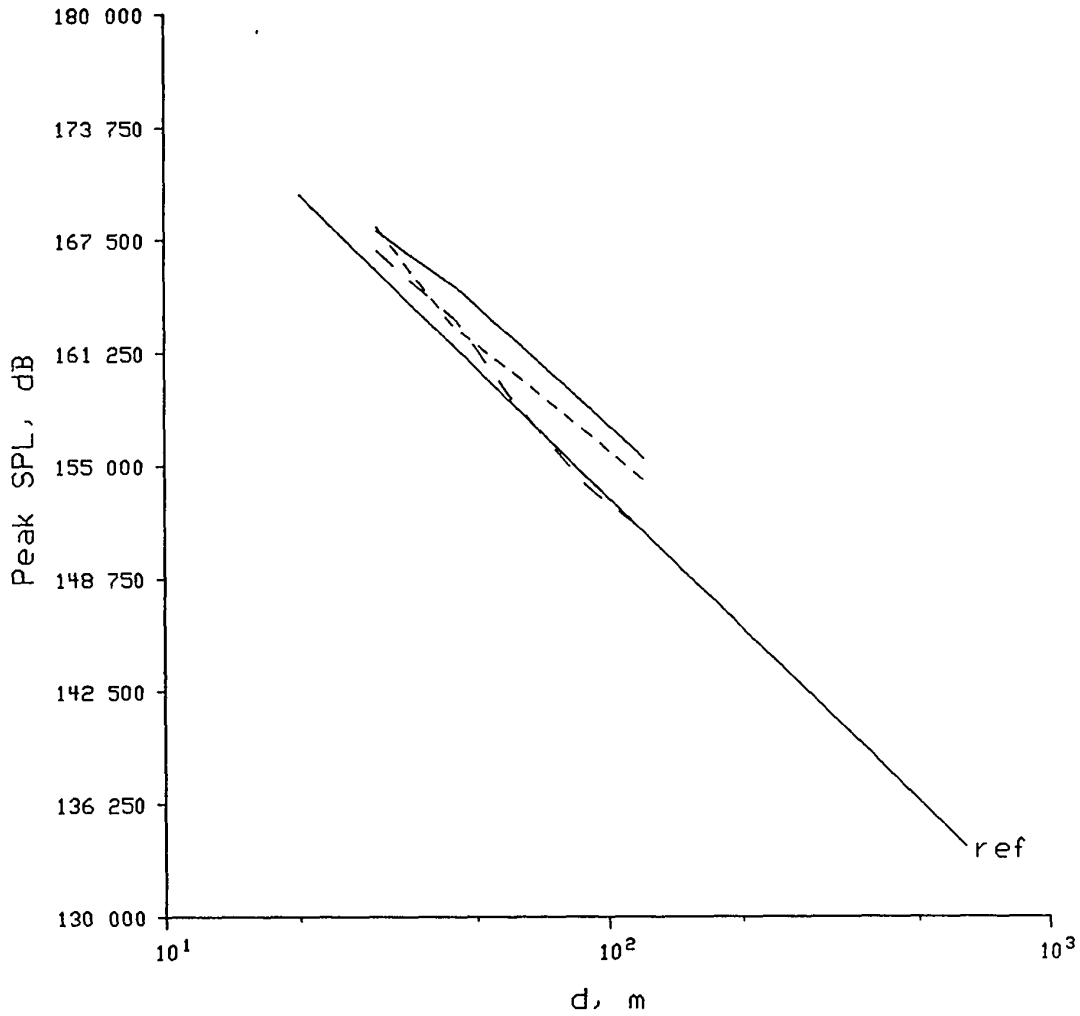

Figure 11.21. 162 dB initial peak pressure SPL versus range for porous surface propagation. The 0 m receiver height is given by the solid line, the 1 m height by the short dashed line, and the 5 m height by the long dashed line. The solid line ending with the label "ref." shows a decay of $r^{-1.2}$ for reference.

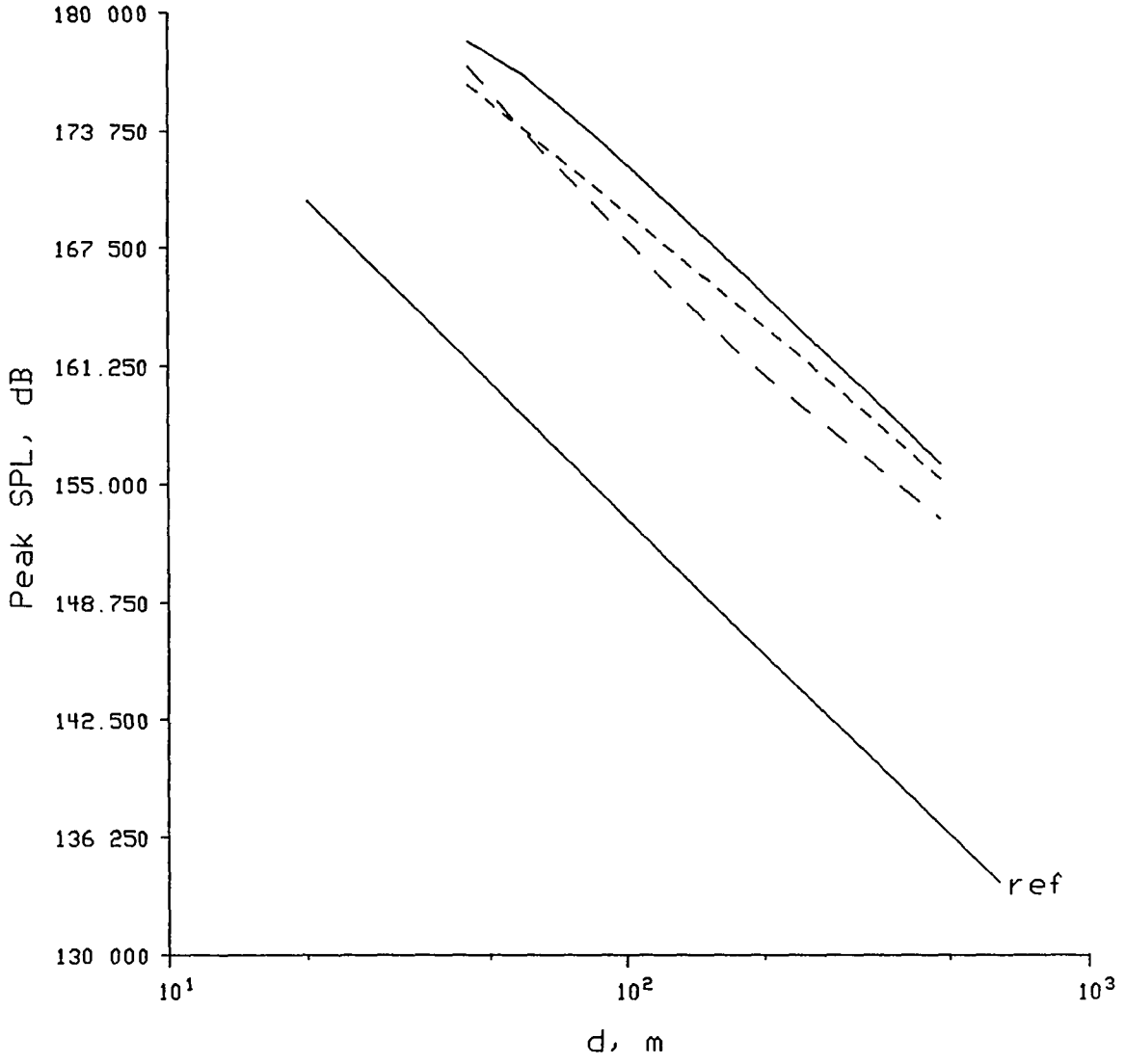

Figure 11.22. 174 dB initial peak pressure SPL versus range for porous surface propagation. The 0 m receiver height is given by the solid line, the 1 m height by the short dashed line, and the 5 m height by the long dashed line. The solid line ending with the label "ref." shows a decay of $r^{-1.2}$ for reference.

Here one also sees that the 1 m height short dashed line is falling off significantly less fast than the solid 0 m height line, and the 5 m height long dashed line slightly less fast.

These results indicate that the peak amplitudes are decaying less fast for increased charge sizes for receivers not on the porous ground surface. Larger charge size blasts, hence, seem to undergo less attenuation due to ground impedance than do smaller charge size blasts. Larger blasts have higher initial peak levels to increase the nonlinear effects, but also are longer and have an increased low frequency content. Since both frequency content and peak amplitudes are being changed for different size charges, the decrease in "excess attenuation" for larger charges clearly cannot be attributable solely to the increased finite amplitude effects.

The pressure versus time plots for the porous runs are shown in Figures 11.23 to 11.28. Here the 150 dB initial free field peak plots at heights 0 m and 5 m, Figures 11.23 and 11.24, respectively, show that the amplitude magnitudes of both the peak and rarefaction are significantly larger near the ground. This is quite different than for the hard surface case where virtually no amplitude difference was detected as a function of height. For the larger initial peak amplitude cases in Figures 11.25 to 11.28, however, only the peak of the blast waves showed a significant increase in pressure near the ground. Here the "trough" shapes and magnitudes of the pulses seem to be unchanged as a function of height, for both 162 and 174 dB.

These findings agree with time harmonic linear theory for the particular geometry and complex impedance used here. Single frequency waves were run in a homogeneous atmosphere sound propagation program based on the work of

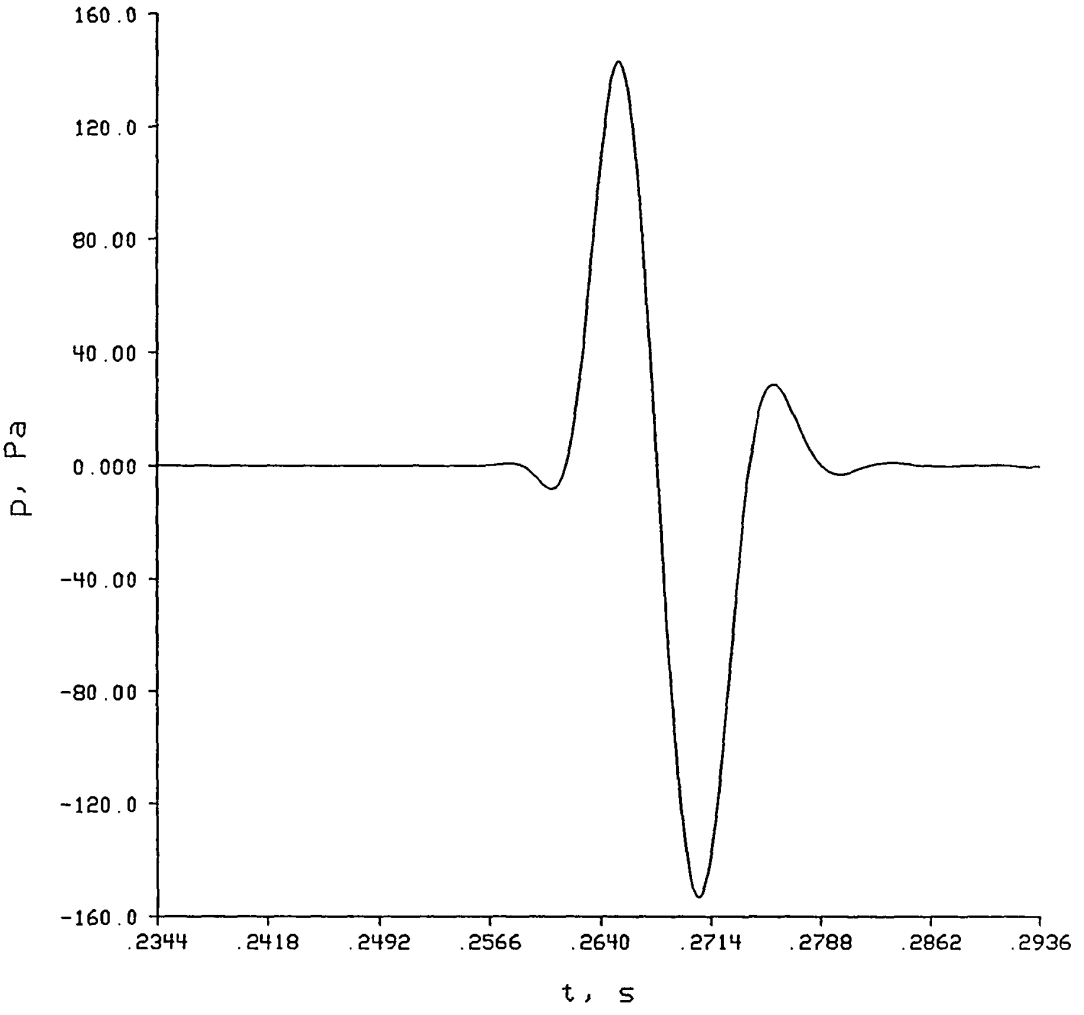

Figure 11.23. Pressure versus time at the 120 m range and the 0 m receiver height for a 150 dB initial peak blast propagating over the porous surface.

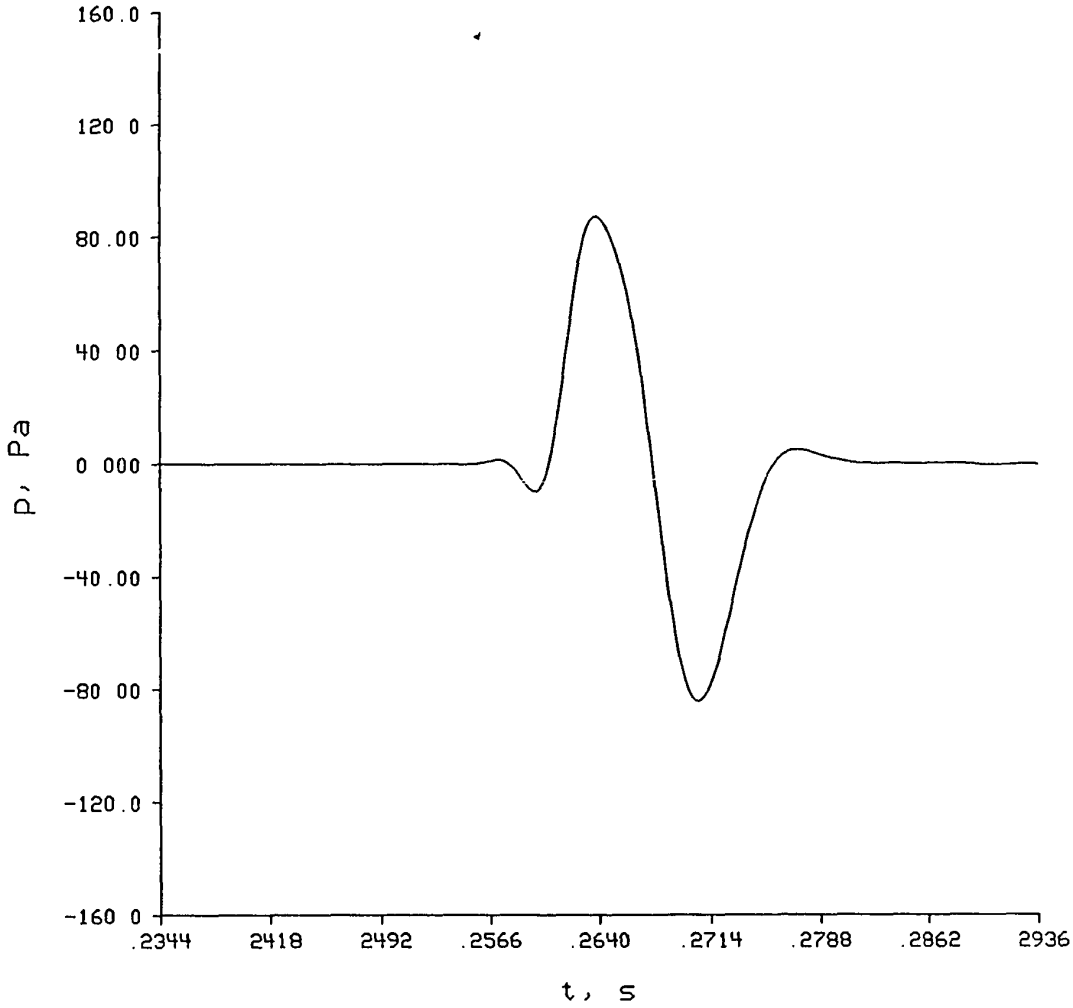

Figure 11.24. Pressure versus time at the 120 m range and the 5 m receiver height for a 150 dB initial peak blast propagating over the porous surface.

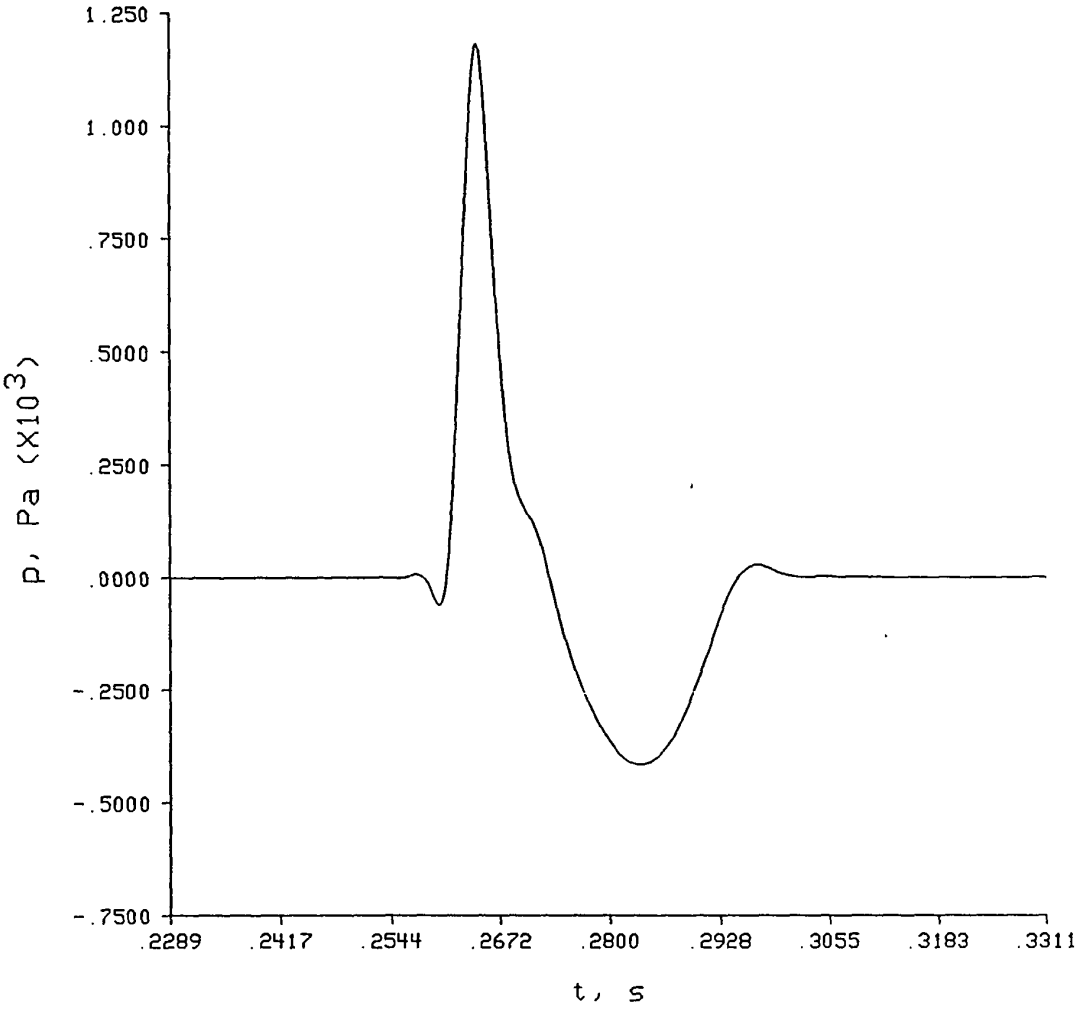

Figure 11.25. Pressure versus time at the 120 m range and the 0 m receiver height for a 162 dB initial peak blast propagating over the porous surface.

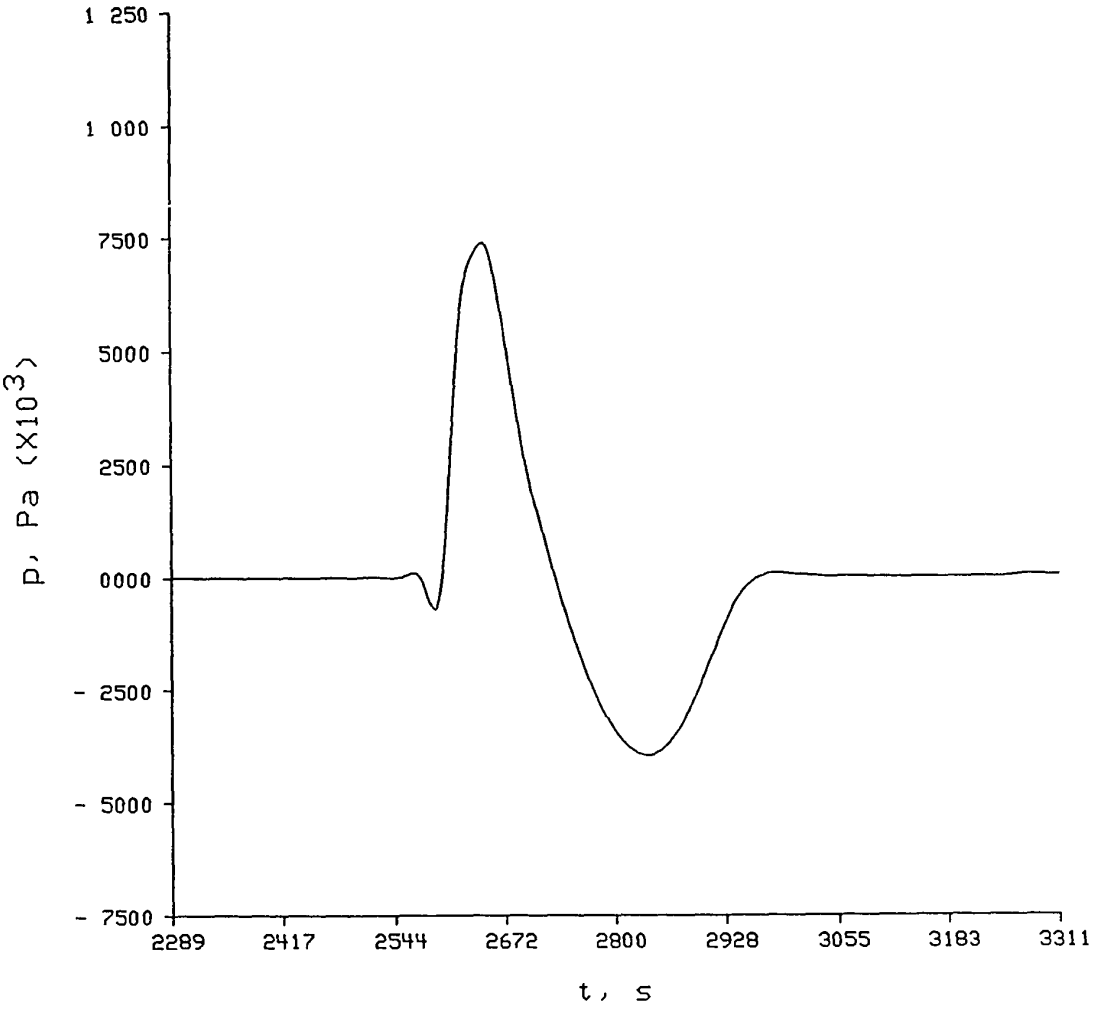

Figure 11.26. Pressure versus time at the 120 m range and the 5 m receiver height for a 162 dB initial peak blast propagating over the porous surface.

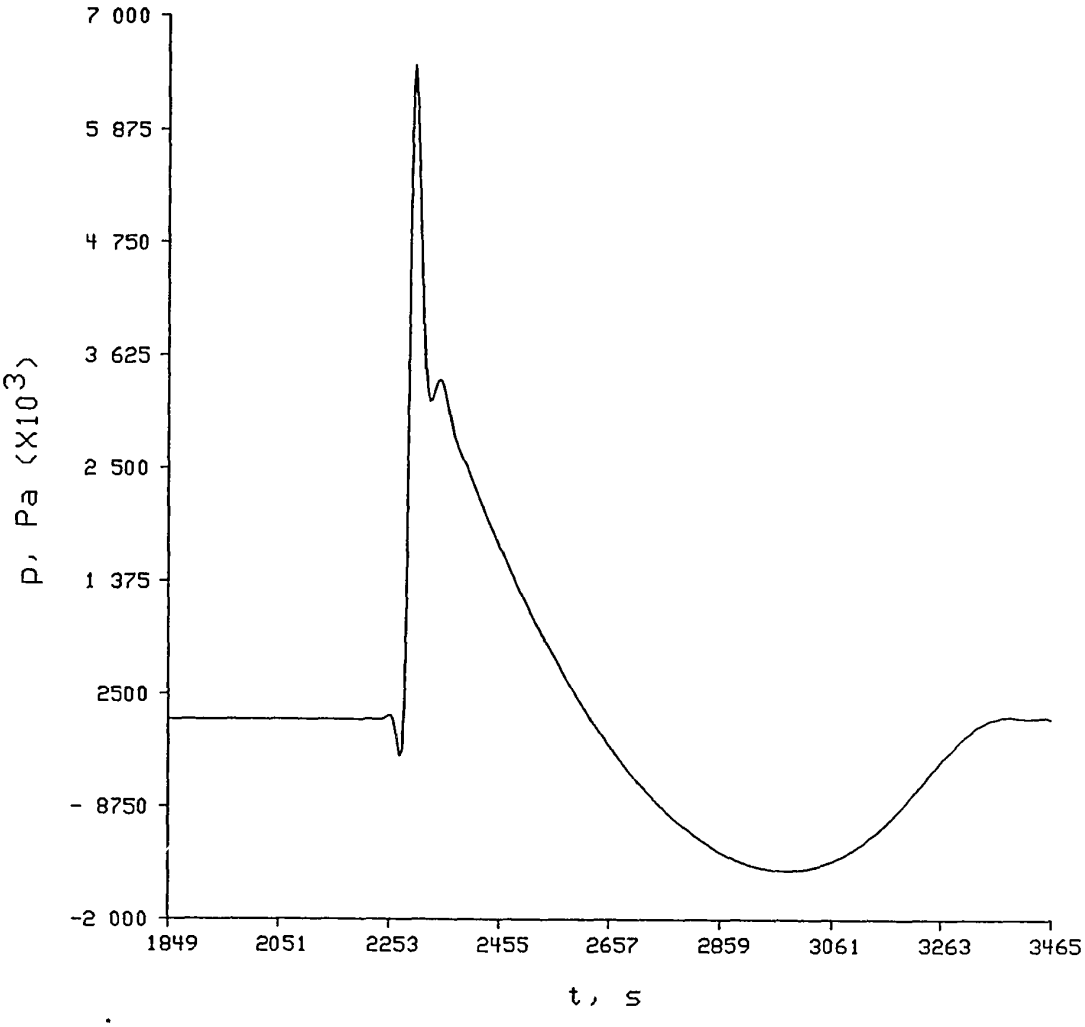

Figure 11.27. Pressure versus time at the 120 m range and the 0 m receiver height for a 174 dB initial peak blast propagating over the porous surface.

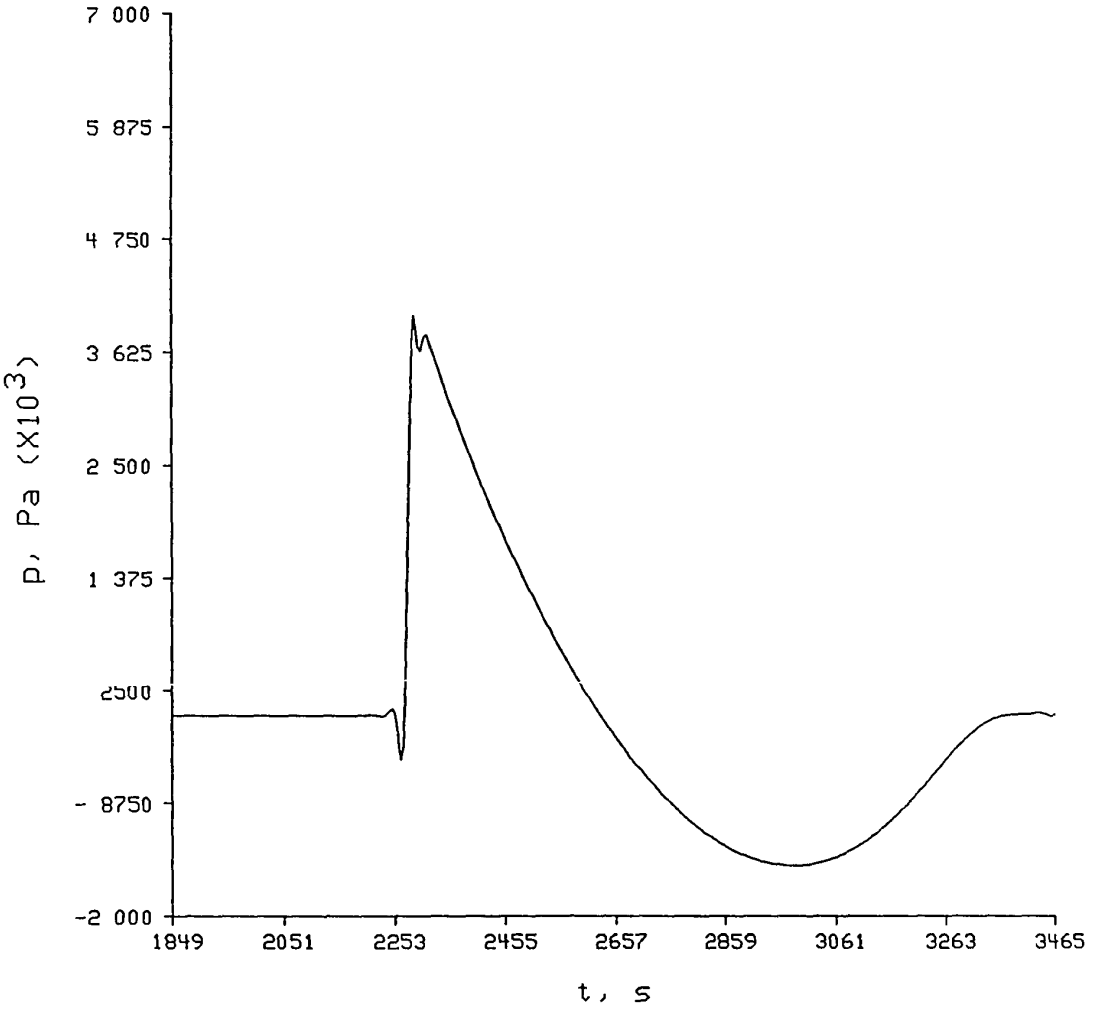

Figure 11.28. Pressure versus time at the 120 m range and the 5 m receiver height for a 174 dB initial peak blast propagating over the porous surface.

Nobile and Hayek.[40,127] In the program the values of impedance from Table 5.1 were used, as a function of frequency. This Nobile and Hayek calculation indicated that there was little difference in levels as a function of height for low frequency waves, but a significant difference as a function of height for high frequencies.

In Figures 11.23 to 11.28 the 150 dB initial peak pulse contains more high frequency energy relative to higher amplitude blasts which allows both the peak and trough of the pulse to be greater in magnitude at the 0 m height than at the 5 m height. For the larger amplitude waves, however, the high frequencies manifest themselves near the "shock" fronts of the pulses and it is here that the amplitude difference is seen between the two heights. Another contributor to the peaks being increased is certainly finite difference phase dispersion. This numerical effect would enhance the peaks also, particularly for the highest runs made at 174 and 180 dB initial free field pressures.

Porous and hard ground runs were also made with the source heights of 3 m instead of 1 m. These values will not be reported in detail here for brevity's sake, since the values were close to those for the 1 m height blasts. No difference was seen in the far field for either the hard or porous cases, and near field differences were only 1 to 2 dB.

12. CONCLUSIONS AND FUTURE WORK

This dissertation has described a finite difference numerical model for the propagation of finite amplitude acoustic blast waves in a homogeneous lossy atmosphere. The nonlinear air propagation equations included classical dissipative effects and may easily be extended to include molecular relaxation effects. The model also accounts for both hard and simple porous media ground surfaces. A time-dependent locally reacting formulation of Morse and Ingard's phenomenological model of a porous medium has been developed to represent the porous ground. The propagation of finite amplitude pulses such as electric spark and blast waves has served to validate the computer algorithms.

The model agrees with the results of free field propagation of sparks using the Pestorius algorithm. It further agrees with the analytic predictions of the pressure amplification factor a for the case of normal plane reflection. The blast computations of a versus angle for various fixed incident peak pressures also give similar results to those models currently in use for strong shock waves. The finite difference program computes slightly different a versus angle curves when the bounding surface is changed from hard to porous.

For different charge sizes detonated near the hard ground surface, the simulated peak sound pressure levels decayed very closely to the power law $r^{-1.2}$ which has been observed in physical experiments. It was found that the larger the charge size, the less the peak levels above the ground are affected by finite ground impedance excess attenuation. This is an important result, not predicted by linear theory propagation codes.

The interaction between finite ground impedance and finite amplitude effects seems to be significant, but not straightforward. The assumption of a first-order additive combination of ground impedance and nonlinear effects should not predict, in general, the correct decay rates of peak sound pressure levels with distance. Such an additive interaction between finite amplitude sound and ground impedance was proposed by Raspet, Bass, and Ezell, for example.[128]

The computer program may be easily extended to increase its accuracy and usefulness. The first obvious extension to the code is to add molecular relaxation effects as described in Chapter 4. Using such relaxation effects in a one-dimensional code would allow the user to calculate blast wave rise times. This one-dimensional program would be fast compared with the two-dimensional version and would run on small mainframe computers instead of on a supercomputer. Another useful extension would be to permit ρ_o and c_o to vary with space. This addition would allow the modeling of nonlinear propagation in a refractive atmosphere.

It would also be desirable to use a 1-D program to further test the impedance of the air-ground interface presented in this thesis, over a wide variety of frequencies. Recall that computation expense made surface impedance measurements difficult for the 2-D program. Since the amplitudes of the waves in the air are finite, it also makes sense that a better porous model would account for nonlinear effects. One might use the nonlinear flow resistance as developed by Blackstock *et al.* for this modification. Another avenue to pursue to give a more realistic porous medium model would be to make the porosity of the medium vary with depth.

The newly developed numerical techniques called ENO for Essentially Non Oscillatory and TVD for Totally Variational Diminishing might be better numerical techniques for solving the equations of this research.[129,130] The ENO methods have only recently been used successfully in more than one dimension, and questions remain on how TVD might work in multidimensions. For a 1-D code these methods should eliminate almost all of the phase dispersion seen with the MacCormack schemes.

Another area that merits further research is the development of absorbing boundary conditions. It would be useful if an absorbing boundary not only exactly absorbed energy from one isolated source, but also from a source and its images. The recent work of Gustaffson provides some insight into possible implementations. In addition, this dissertation contains linear lossless boundary conditions which were applied to a system of lossy nonlinear equations. One should derive the absorbing boundaries for the lossy nonlinear system itself and provide a mathematical stability proof for the resulting conditions.

Finally, this thesis has centered solely on the propagation of sound in air outdoors. The equations developed, however, are applicable to other fluid acoustic media also, such as water. There is great promise in using this type of numerical solution in biomedical ultrasonics, for example, lithotripsy, diagnostic ultrasound, and hyperthermia modeling. Applying the finite difference methods in the time domain to underwater acoustics, such as in simulating parametric arrays, should be possible also.

APPENDIX A.

FINITE AMPLITUDE ACOUSTICS AND THE 1812 OVERTURE

There are few outdoor musical events which compare to a live performance of Peter Ilyich Tchaikovsky's *Overture 1812* with cannons. This Opus No. 49, universal in its appeal, has packed audiences for orchestras all over the world since its first performance in 1882. The score calls for not only cannons, but also the pealing of church bells and a brass band *ad libitum*.

This appendix will explore some of the aspects of *1812* performances with cannons as they relate to the subject matter of this dissertation, the propagation of finite amplitude waves outdoors. For example, are the cannon sounds loud enough to exhibit finite amplitude behavior? Could the amplitudes produced be high enough to change the propagation time of the cannon blast sounds, interfering with a clean performance of the music? Or could the peak pressures be so loud as to cause pain for certain individuals?

This work is 420 measures long and runs approximately 15 minutes, if no cuts are made to the score. Sixteen cannon blasts were specified by the composer in the piece, 5 shots in measures 328 to 332, and 11 from measures 388 to 404. Conductors often take substantial liberties with the composer's score, however. The author has heard some performances where a single shot is put in on the first beat of measure 36. Other performances omit Tchaikovsky's first group of 5 shots entirely due to their difficult syncopated rhythm, and/or continue to blast away between measures 405 and the end.[131]

Getting the blasts right on the beat in time with the orchestra is a major difficulty, as one might expect. A chain of command between a conductor and some national guardsmen firing blanks from howitzers probably will not get the job done. The composer originally hoped that electrical ignition could be used, a conductor having 16 switches to flip at the appropriate moments.[132] A technique similar to this has been used for several years now by J. Paul Barnett of South Bend Replicas, Inc. Mr Barnett, a builder of firable antique cannons for museums and historic landmarks, has developed an electronic system where he will fire 16 Lyle guns for an orchestra safely and on the beat. These guns originally were used to shoot life saving lines from shore to ships in distress.

The author was allowed to observe and record one of Mr. Barnett's 12 or so concerts per summer, a performance with the Chicago Symphony Orchestra at the Ravinia Summer Music Festival in Highland Park, Illinois on August 13, 1989. A 0.0064 m Larson Davis microphone was mounted 0.91 m above the ground, 12.2 m from the closest gun and 16.2 m from the furthest gun. The guns were in two rows, all facing away from the recording apparatus. The microphone signal was preamplified and fed into an Nagra DJ reel-to-reel recorder at 0.38 m/s speed. The recording apparatus was calibrated with a Bruel and Kjaer Pistonphone with a reference level of 123.9 dB sound pressure level. Mr. Barnett used 0.092 kg black powder charges, wrapped in aluminum foil and plastic wrap. There was a thunderstorm just prior the the concert, and the grassy ground between the recording devices and the guns was water soaked during the performance.

In the laboratory the blasts were analyzed using a Hewlett Packard 1727A Storage Oscilloscope. Based on the voltage waveforms from the blasts, referenced to the pistonphone source, the following peak sound pressure levels in dB were found for the 16 shots in the order they were fired: 141.8, 138.5, 136.5, 137.9, 139.6, 135.0, 138.5, 139.0, 136.9, 140.5, 139.0, 139.8, 138.5, 138.5, 141.0, and 141.0. In most of the blasts two peaks were observed, an initial large direct wave peak (SPL just given) and a smaller peak occurring later due to some reflection. The blast wave forms including reflection were 24 ms to 32 ms in length.

With these data in hand, it is possible to speculate on whether finite amplitude propagation effects have a significant impact on these *1812* pulses. Considering that the sound was roughly falling off as $1/r$, it is clear that finite amplitude nonlinear effects should be important only in the near field of the guns. If the level has already fallen to a 141 dB maximum at a minimum distance of 12.192 m, no significant change in the speed of propagation would be noticed. Adding a few dB to account for the receiving equipment being behind the gun would make little difference. One can predict that using slightly more black powder for larger charges would not change this hypothesis.

On the other hand, since many individuals' threshold of pain is below 140 dB, the peak pressures from Barnett's Lyle guns could be uncomfortably loud even several hundred feet from them. It is important to remember that in a large crowd of people with no ear protection, some individuals will be more sensitive to the blast noise than others, and that the audience and musicians should be kept a

respectable distance from these guns. At Ravinia, some audience members were approximately 30.5 m from the closest gun, which is probably too close.

APPENDIX B.

COMPUTER PROGRAM DESCRIPTION

This appendix describes the computer program, **mcnalp**, employed in this thesis. The acronym **mcnalp** stands for MacCormack Nonlinear Air-Linear Porous and uses the second-order in time and fourth-order in space MacCormack finite difference schemes for the main part of the nonlinear air equations in two-dimensions and the second-order in time and space MacCormack method for the linear pore equations in one-dimension. The code is over 5000 lines of FORTRAN77 statements and was optimized for the Cray type supercomputers. The language FORTRAN was used since that was the only scientific language available on the Cray other than assembler in the beginning of this research.

The program may be run in its current form to model blast waves propagating outdoors either in the free field or over a hard or a porous model of the ground. One can also make minor modifications to the program to model the propagation of electric spark pulses in air or weak explosions under water.

As it is described here, the program is ready for running in a batch mode Cray environment. All of the subroutines are in one file except for one routine "d8pimg" which physically writes out a National Center for Supercomputing Applications (NCSA) Hierarchical Data Format (HDF) raster image file. The HDF routines are public domain software routines available from NCSA. To change various parameters which control the operation of **mcnalp**, the user must modify the code itself in the main program. At a later date, this drawback will be eliminated by

providing an interactive, user friendly front end. For this description, however, the current batch mode implementation will be assumed.

The program **mcnalp** provides several types of output, some of which are more useful than others for particular applications. The program produces image files of raster images in HDF form, numerical receiver files of pressure versus time at specified locations, and a file of maximum pressures encountered along the ground surface called rpmx.out. These are the three most often used types of output **mcnalp** provides. The program can also produce ASCII output files of pressures if the raster data output is not desired and can print almost all of the numbers computed in the program using a debugging option. This last type of output was used only in the early stages of this research.

Nine logical variables, i.e., true or false variables, control the major ways the program can operate. When "debug" is true, debugging output is printed to the screen. If "raster" is true, the HDF image files are produced. Otherwise, ASCII output is placed in the file ascii.out. If "sscale" is true the HDF files are printed with the variables scaled by the factor $1/r$ which keeps the images from fading away for long distance propagation. The flag "allrast" specifies whether all the variables will be printed in raster HDF files, or just the acoustic pressures. The variable "rcvrs" indicates whether the numerical receiver data will be produced. The location of the receivers must be specified by the user in **mcnalp**'s main subprogram. The flag "rowpmax" tells **mcnalp** whether or not to save the values of maximum pressure recorded along a line in the d direction, usually the ground surface. If this flag is turned on, the user must specify the distance between the source and this line

of maximum pressure data in the main subprogram. The two variables "gnd" and "hard" together tell whether a ground surface is used and if so what kind is used. If "gnd" is false, a free field calculation is made. If "gnd" is true, "hard" being true specifies that a hard ground is in use, and "hard" being false gives the porous ground case. The last variable "doupdat" indicates whether updating in the d direction is used or not. If "doupdat" is true, an updating routine is called every few time steps to conserve computer memory by overwriting a part of the memory that the wave leaves by more free field that the wave can propagate into.

The coordinate system used in this program is cylindrical. The program employs some different names for the coordinate axes compared to the rest of this thesis, however. While in the main text of this thesis the coordinate system used was (d, z, ϕ) with ϕ variations eliminated, **mcnalp** currently uses the two notations (r, z, ϕ) and $(y1, y2, \phi)$. Therefore, whenever the reader sees a $y1$ or a cylindrical r in the program, it always means d. Similarly $y2$ always means z.

The main grid array "grid" in the air is rectangular in d and z. The coordinate d goes from $y1 =$ 1 to $y1=$ numy1s, and z goes from $y2 =$ 1 to $y2 =$ numy2s. The array "grid" contains the variables ρ', u, v, and s_{fr} at the present time n and the temporary time $\tilde{n}$ used in the MacCormack finite difference methods. The variables p and T' are kept in arrays of the same names. The porous medium is kept in an array "pore" which contains both ρ' and v for the pores at the times n and $\tilde{n}$. All of these variables are kept in a Fortran common block /gridvars/. Because the fourth-order in space MacCormack schemes of the air cannot be used near the boundaries, /gridvars/ also contains the arrays "specr" and "specz" to help with

data storage in implementing the second-order in space MacCormack schemes near the boundaries.

The other common blocks in this program hold global variables grouped together for convenience. The block /times/ contains information needed for printing the raster images at specific times, the values of Δt, and the time at which the program will stop. The block /cons/ holds the constants needed for air propagation such as the sound speed and the other thermodynamic variables. On the other hand, /pcons/ contains the constants needed for the porous medium. The massive block /bndvars/ groups together the variables needed for the boundary calculations. Since "grid" is rectangular, four boundaries are needed, the boundary close to the source, the outer boundary opposite the source boundary, the ground boundary, and the upper boundary.

Some smaller common blocks are much more limited in their scope. The block /flags/ holds the logical variables described above. The block /diffcon/ contains the constants used in the main MacCormack routines which are precomputed to speed program execution. The common block /pulsvars/ holds the variables to describe the modified Jack Reed pulse for the initial conditions of the simulation. The information to control the updating in the d direction routines is contained in the block /upblk/. The block /rcvr/ holds numerical receiver height and distance information. Finally, /rpmax/ includes the variables to save the maximum pressures along a line in the d direction, usually along the ground surface.

The subroutines in the program are for the most part self-documenting with ample comment lines. The largest routines "diffarp," "diffarc," "diffazp,"

"diffazc," "diffbrp," "diffbrc," "diffbzp," and "diffbzc" were the most time consuming to write and perform the MacCormack time difference methods in the air. The diffa routines use the "a" version of the MacCormack methods, while the diffb routines use the "b" version. The next to last of the letters in the names of these eight routines specifies first what direction the routine is for, either r, i.e., d, or z, and the last letter tells whether this routine gives the predictor step or the corrector step. For example, "diffbzp" is the predictor step of the b MacCormack method in the z direction.

The boundary conditions are implemented in routines "upbnd1," "gndbnd1," "outbnd1," "srcbnd1," "prebnd," and "bnd2." The first four routines compute and store the information needed for the boundaries under free field conditions, and "bnd2" applies either these data and/or the appropriate ground condition. Routine "prebnd" precalculates values needed for the numerical boundary conditions. Subroutine "porous" computes all of the variable values in the porous medium for use as a porous boundary condition in "bnd2." The equations of state in the air at the times n and $\tilde{n}$ are used in the routines "pandt" and "pandt2," respectively, to give updated values of p and T'. Subroutines "enta" and "entb" are used in addition to the "diffXXX" modules to keep the values of s_{fr} correctly updated near the boundaries in the air.

Two of the unique features of **mcnalp** include saving memory by updating or windowing in the d direction and recording the maximum pressure values along the ground. The routine "update" performs the first function, and "getrpmax" the

second. The subroutine "wrpmax" writes out the file rpmx.out if the maximum pressure information is desired.

The other routines which give results for later analysis are "prntifok," "prntgrid," and "prraster." The program calls "prntifok" every time step to see if any images should be saved and to save the numerical receiver waveforms, should there be any receivers specified. If the raster data output is needed, "prntifok" calls "prraster," or if ASCII images are needed, it calls "prntgrid."

The first of the rest of the Fortran modules called by the main program are "prediff" which precomputes the constants needed for the MacCormack routines "diffXXX." The routines "getw," "getw2," "getwt," and "getwt2" compute one-directional derivatives so the "diffXXX" routines can calculate the mixed derivatives which occur in the dissipative terms of the air equations. This is one place where one might be able to improve **mcnalp**, by incorporating these routines into the "diffXXX" routines. The program also calls the real functions "rm2" and "rpot2" which are the modified Reed blast pulse pressure and potential waveforms, respectively.

The main routine in **mcnalp** can be thought of in four sections after all the variable declarations. In the first section the user specifies the problem to be solved by setting the flags, defining the constants to be used, placing the boundaries, specifying the times to print images, and placing the numerical receivers. The second section of **mcnalp** generates the discretized grid on which the problem will be

solved, and the third section initializes the variables to their initial condition for the beginning of the calculation.

The last section of **mcnalp** is the main loop of the program in which the numerical solution is advanced in time. For every iteration of this loop the variables are all stepped in time one Δt. Each time the loop is executed, two paths are alternately taken. This alternation is necessary since the MacCormack "a" and "b" schemes must be alternated, as well as the r, i.e., d, and z directions.

The first path through the loop is now described. The second path is similar. The program **mcnalp** first computes the radiation boundary conditions and saves these numbers using "upbnd1," "gndbnd1," "outbnd1," and "srcbnd1." The r, i.e., d, direction routines are then called. The routine "getwt" precomputes information for "diffarp" which comes next. Subroutine "enta" then updates the entropy variable s_{fr} near the boundaries. Routines "pandt2" and "getwt2" then update p and T' at the temporary time and precompute information at the temporary time for "diffarc" which follows. An invocation of "pandt" to obtain the pressure and temperature deviation completes the r direction part of the main loop's first path.

The z direction part of the main loop's first path begins by "getw" precomputing information for "diffazp" which follows it. The routine "pandt2" then updates p and T' at the temporary time. Subroutine "getw2" then precomputes values for "diffazc" which comes next. The "bnd2" routine is then called to update the boundary values for the air grid. If the porous ground is employed in the calculation, "bnd2" calls the routine "porous" at this time. After "bnd2" finishes, the routine "pandt" updates p and T' at this time. The program has now advanced the

numerical solution one time step, Δt. This pass of the main loop ends by calling "getrpmax," "prntifok," and "update."

In the next iteration of the main loop the "b" routines are called, first in the z direction then in the r, i.e., d, direction. It then also calls "getrpmax," "prntifok," and "update." Next the "a" path of the main loop is executed again. This process continues, the program alternately passing through the two paths of the main loop, until **mcnalp** terminates when the time reached exceeds the maximum time the user has specified.

The last major component of **mcnalp** which requires detailed description is the updating procedure. If the flag "doupdat" is false, no updating is performed, and the grid variables span the d direction from "miny1" to "miny2" using the discretization i going from 1 to "numy1s." The problem here is that a wave, initially between "miny1" and "maxy1," moving in the d direction will eventually pass the "maxy1" boundary and propagate out of the numerical domain.

If the flag "doupdat" is true, however, a wave moving in the d direction will never move out of the numerical domain because every few time steps the domain is extended in the $+d$ direction while simultaneously deleted in the $-d$ direction. Performing these extensions beyond the outer boundary and deletions close to the source boundary windows a pulse moving in the $+d$ direction.

This action saves much computer memory for a long distance propagation run. Instead of having all of the distance between the initial pulse position and its final position in memory at once, only the window that the pulse is in at any one time is

kept in memory.

The windowing, or updating, procedure is performed with the array "ii." In **mcnalp**, whenever a variable is given d or z positions such as p(i,j) for the pressure at d = "y1(i)" and z = "y2(j)," the notation p(ii(i),j) is used. If "doupdat" is false, no updating is performed and the "ii" array takes the values "ii(1)"= 1, "ii(2)" = 2, . . ., "ii(n)" = n, etc. Thus in the "doupdat" false case the array "ii" acts as if it is not there at all.

If "doupdat" is true, however, after the wave has propagated a certain distance, an update is performed. Suppose there were ten points in the d direction, "numy1s"= 10, and "ii" and "y1" had the values "ii(1)"= 1, "ii(2)"= 2, . . ., "ii(10)"= 10 and "y1(ii(1))"= 1.0 m, "y1(ii(2))"= 1.1 m, "y1(ii(3))"= 1.2 m, . . ., "y1(ii(10))"= 1.9 m, respectively, initially. If the update shifted things by 2 points, one would be left with "ii(1)"= 3, "ii(2)"= 4, . . ., "ii(8)"= 10, "ii(9)"= 1, "ii(10)"= 2 and "y1(ii(1))"= 1.2 m, "y1(ii(2))"= 1.3 m, . . ., "y1(ii(8))"= 2.0 m, "y1(ii(9))"= 2.1 m, "y1(ii(10))"= 2.2 m. Here the d distances 1.0 m and 1.1 m are no longer represented, having been replaced by distances 2.0 and 2.1 m. By repeating this method over and over for updates as the wave moves, the pulse is windowed for propagation in the d direction.

To implement this updating procedure, the user needs to specify a variable in the main program, "ng." The variable "ng" is the number of grid increments, i.e., the number of Δx's, the wave should move before an update is performed. Another variable the program automatically initializes for the updating procedure is "ut." The variable "ut" is the update time and gives the amount of time elapsed since the

last update. The test "Is ut $c_0 \geq$ ng Δx ?" is made at the bottom of the main loop of the program, and routine "update" is called if this test is true. The routine "update" zeros the variable "ut" every time the procedure is invoked to prepare for the next update. The subroutine "ut" is incremented by Δt on every iteration of the main loop to count up until the update test is true.

One final note about the present version of **mcnalp**. Statements reading CDIR$ IVDEP were placed before some of the do loops in the subroutines. Under Cray FORTRAN the statement is a compiler directive to Ignore Vector DEPendencies. These compiler directives were inserted to tell the Cray FORTRAN compiler that even though the do loop might look as though it could contain a dependency, it does not and should be vectorized. Dependencies are sequences of memory reference operations that keep a loop from vectorizing, and eliminating dependencies gives a marked increase in performance. Under most FORTRAN compilers these CDIR$ IVDEP statements are interpreted as comment statements.

To give some idea of how well **mcnalp** vectorizes and performs on the Cray series, a short run was made on both the Cray-2 at NCSA and the CERL Pyramid Pyr90x mainframe computer. Global optimization was used with the Fortran compilers on both systems. On the CERL Pyramid with no one else logged in, the program took approximately 90 min of CPU time. The Cray-2 ran the same program in 5.3 s, approximately a speed-up of 1000 times.

REFERENCES

1. S. W. Lee, N. Bong, W. F. Richards, and Richard Raspet, "Impedance formulation of the fast field program for acoustic wave propagation in the atmosphere," J. Acoust. Soc. Am. **79**, 628-634 (1986).

2. R. Raspet, S. W. Lee, *et al.*, "A fast-field program for sound propagation in a layered atmosphere above an impedance ground," J. Acoust. Soc. Am. **77**, 345-352 (1985).

3. S. J. Franke and G. W. Swenson, Jr., "A brief tutorial on the fast field program (FFP) as applied to sound propagation in the air," Appl. Acoust. **27**, 203-216 (1989).

4. Richard Raspet and Richard K. Wolf, "Application of the fast field program to the prediction of average noise levels around sources," Appl. Acoust. **27**, 217-226 (1989).

5. Kenneth E. Gilbert and Michael J. White, "Application of the parabolic equation to sound propagation in a refracting atmosphere," J. Acoust. Soc. Am. **85**, 630-637 (1989).

6. Michael J. White and Kenneth E. Gilbert, "Application of the parabolic equation to the outdoor propagation of sound," Appl. Acoust. **27**, 227-238 (1989).

7. *Nonlinear Acoustics in Fluids*, Robert T. Beyer, ed. (Van Nostrand Reinhold, New York, 1984).

8. Robert T. Beyer, *Nonlinear Acoustics* (Naval Sea Systems Command, Navy Dept., 1974).

9. M. F. Hamilton, "Fundamentals and applications of nonlinear acoustics," in *Nonlinear Wave Propagation in Mechanics*, T. W. Wright, ed. (ASME, 1987).

10. David T. Blackstock, "Nonlinear acoustics (theoretical)," in *AIP Handbook*, 3rd ed. (McGraw-Hill, New York, 1972).

11. Robert T. Beyer, *Nonlinear Acoustics* (Naval Sea Systems Command, Navy Dept., 1974), p. 98.

12. Robert T. Beyer, *Nonlinear Acoustics* (Naval Sea Systems Command, Navy Dept., 1974), pp. 1-2.

13. David T. Blackstock, "Connection between the Fay and Fubini solutions for plane sound waves of finite amplitude," J. Acoust. Soc. Am. **39**, 1019-1026 (1966).

14. T. G. Muir and E. L. Carstensen, "Prediction of nonlinear acoustic effects at biomedical frequencies and intensities," Ultrasound in Med. and Biol. **6**, 345-357 (1980).

15. David T. Blackstock, "Generalized Burgers equation for plane waves," J. Acoust. Soc. Am. **77**, 2050-2053 (1985).

16. P. L. Sachdev, *Nonlinear Diffusive Waves* (Cambridge, New York, 1987).

17. J. J. C. Nimmo and D. G. Crighton, "Geometrical and diffusive effects in nonlinear acoustic propagation over long ranges," Phil. Trans. R. Soc. Lond. Ser. A **320**, 1-35 (1986).

18. D. H. Trivett and A. L. Van Buren, "Propagation of plane, cylindrical, and spherical finite amplitude waves," J. Acoust. Soc. Am. **69**, 943-949 (1981).

19. D. H. Trivett and A. L. Van Buren, "A FORTRAN computer program for calculating the propagation of plane, cylindrical, or spherical finite amplitude waves," Naval Research Laboratory Report 4413, AD-A095386.

20. Hideto Mitome, "An exact solution for finite-amplitude plane sound waves in a dissipative fluid," J. Acoust. Soc. Am. **86**, 2334-2338 (1989).

21. Allan D. Pierce, *Acoustics: An Introduction to Its Physical Principles and Applications* (Acoust. Soc. Am., Woodbury, NY, 1989), pp. 587-593.

22. F. M. Pestorius and D. T. Blackstock, "Propagation of finite-amplitude noise," in *Finite-amplitude Wave Effects in Fluids*, L. Bjørnø, ed. (IPC Science and Technology Press, Guilford, England, 1974).

23. Mark A. Theobald, "Experimental study of outdoor propagation of spherically spreading periodic acoustic waves of finite amplitude," Appl. Res. Lab Tech. Rep. No. 77-5 (ARL-TR-77-5), AD-A039020, Applied Research Laboratories, The University of Texas at Austin, Austin, TX (January 1977).

24. Mark O. Anderson, "The propagation of a spherical N wave in an absorbing medium and its diffraction by a circular aperture," Appl. Res. Lab Tech. Rep. No. 77-5 (ARL-TR-74-25), AD-787878, Applied Research Laboratories, The University of Texas at Austin, Austin, TX (August 1974).

25. Henry E. Bass, Jean Ezell, and Richard Raspet, "Effect of vibrational relaxation on rise times of shock waves in the atmosphere," J. Acoust. Soc. Am. **74**, 1514-1517 (1983).

26. H. E. Bass and Richard Raspet, "Vibrational relaxation effects on the atmospheric attenuation and rise times of explosion waves," J. Acoust. Soc. Am. **64**, 1208-1210 (1978).

27. L. B. Orenstein, "The rise time of N waves produced by sparks," Appl. Res. Lab Tech. Rep. No. 82-51 (ARL-TR-82-51), AD-A120817, Applied Research Laboratories, The University of Texas at Austin, Austin, TX (October 1982).

28. B. Edward McDonald and W. A. Kuperman, "Time domain formulation of pulse propagation including nonlinear behavior at a caustic," J. Acoust. Soc. Am. **81**, 1406-1417 (1987).

29. Sigurd Avar Aanonsen, Tor Barkve, Jacqueline Naze Tjótta, and Sigve Tjótta, "Distortion and harmonic generation in the nearfield of a fine amplitude sound beam," J. Acoust. Soc. Am. **75**, 749-768 (1984).

30. Mark F. Hamilton, Jacqueline Naze Tjótta, and Sigve Tjótta, "Nonlinear effects in the farfield of a directive sound source," J. Acoust. Soc. Am. **78**, 202-216 (1985).

31. Timothy S. Hart and Mark F. Hamilton, "Nonlinear effects in focused sound beams," J. Acoust. Soc. Am. **84**, 1488-1496 (1988).

32. J. E. Piercy, T. F. W. Embleton, and L. C. Sutherland, "Review of noise propagation in the atmosphere," J. Acoust. Soc. Am. **61**, 1403-1418 (1977).

33. T. F. W. Embleton, "Sound propagation outdoors– improved prediction schemes for the 80's," Noise Control Eng. **18**, 30-39 (1982).

34. Tony F. W. Embleton, "Outdoor sound propagation," in *Proceedings of Noise-Con 87*, Jiri Tichy and Sabih Hayek, eds. (Penn. State University, State College, PA, 1987), pp. 15-26.

35. Allan D. Pierce, *Acoustics: An Introduction to Its Physical Principles and Applications* (Acoust. Soc. Am., Woodbury, NY, 1989).

36. Lawrence E. Kinsler, Austin R. Frey, Alan B. Coppens, and James V. Sanders, *Fundamentals of Acoustics*, 3rd ed. (John Wiley, New York, 1982).

37. T. F. W. Embleton, J. E. Piercy, and N. Olson, "Outdoor sound propagation over ground of finite impedance," J. Acoust. Soc. Am. **59**, 267-277 (1976).

38. Keith Attenborough, Sabih I. Hayek, and James M. Lawther, "Propagation of sound above a porous half-space," J. Acoust. Soc. Am. **68**, 1493-1501 (1980).

39. G. A. Daigle, T. F. W. Embleton, and J. E. Piercy, "Some comments on the literature of propagation near boundaries of finite acoustical impedance," J. Acoust. Soc. Am. **66**, 918-919 (1979).

40. Matthew A. Nobile and Sabih I. Hayek, "Acoustic propagation over an impedance plane," J. Acoust. Soc. Am. **78**, 1325-1336 (1985).

41. C. I. Chessell, "Propagation of noise along a finite impedance boundary," J. Acoust. Soc. Am. **62**, 825-834 (1977).

42. K. Attenborough, "Acoustical impedance models for outdoor ground surfaces," J. Sound Vib. **99**, 521-544 (1985).

43. Philip M. Morse and K. Uno Ingard, *Theoretical Acoustics* (McGraw-Hill, New York, 1968).

44. Herbert L. Kuntz and David T. Blackstock, "Attenuation of intense sinusoidal waves in air-saturated, bulk porous materials," J. Acoust. Soc. Am. **81**, 1723-1731 (1987).

45. D. A. Nelson, "Interaction of finite-amplitude sound with air-filled porous materials," Appl. Res. Lab Tech. Rep. No. 85-15 (ARL-TR-85-15), AD-A155986, Applied Research Laboratories, The University of Texas at Austin, Austin, TX (March 1985).

46. A. S. Hersh, "Acoustic behavior of fibrous bulk materials," AIAA Pap. 80-0986, AIAA Aeroacoust. Conf., 6th, Hartford, CT, June 4-6, 1980.

47. David K. Wilson, Jason D. McIntosh, and Robert F. Lambert, "Forchheimer-type nonlinearities for high-intensity propagation of pure tones in air-saturated porous media," J. Acoust. Soc. Am. **84**, 350-359 (1988).

48. Mark A. Johnson, Richard Raspet, and Michael T. Bobak, "A turbulence model for sound propagation from an elevated source above level ground," J. Acoust. Soc. Am. **81**, 638-646 (1987).

49. H. A. Panofsky and J. A. Dutton, *Atmospheric Turbulence: Models and Methods for Engineering Applications* (Wiley, New York, 1984).

50. Walton Edward McBride, III, "A scattering center based numerical simulation of small scale atmospheric turbulence," Ph. D. thesis, University of Mississippi, 1989.

51. Allan D. Pierce, *Acoustics: An Introduction to Its Physical Principles and Applications* (Acoust. Soc. Am., Woodbury, NY, 1989).

52. Mark F. Hamilton and David T. Blackstock, "On the coefficient of nonlinearity β in nonlinear acoustics," J. Acoust. Soc. Am. **83**, 74-77 (1988).

53. Frederick D. Cotaras, "Reflection and refraction of finite amplitude acoustic waves at a fluid-fluid interface," Appl. Res. Lab Tech. Rep No. 89-1 (ARL-TR-89-1), Applied Research Laboratories, The University of Texas at Austin, Austin, TX (March 1985), p. 18.

54. J. W. S. Rayleigh, *The Theory of Sound*, Vol. 2 (Dover, New York, 1945), pp. 319-342.

55. C. Zwikker and C. W. Kosten, *Sound Absorbing Materials* (Elsevier, New York, 1949).

56. Philip M. Morse and K. Uno Ingard, *Theoretical Acoustics* (McGraw-Hill, New York, 1968), pp. 252-255.

57. R. J. Donato, "Impedance models for grass-covered ground," J. Acoust. Soc. Am. **61**, 1449-1452 (1977).

58. Keith Attenborough, "Acoustical characteristics of rigid fibrous absorbents and granular materials," J. Acoust. Soc. Am. **73**, 785-799 (1983).

59. Keith Attenborough, "On the acoustic slow wave in air-filled granular media," J. Acoust. Soc. Am. **81**, 93-102 (1987).

60. Keith Attenborough, "Acoustical characteristics of porous materials," Physics Reports **82**, 179-227 (1982).

61. Keith Attenborough, "Acoustical characteristics of rigid fibrous absorbents and granular materials," J. Acoust. Soc. Am. **73**, 786 (1983).

62. Keith Attenborough, "Acoustical characteristics of rigid fibrous absorbents and granular materials," J. Acoust. Soc. Am. **73**, 791 (1983).

63. James Sabatier (private communication).

64. Richard Raspet and Gordon E. Baird, "The acoustic surface wave above a complex impedance ground surface," J. Acoust. Soc. Am. **85**, 638-640 (1989).

65. R. J. Donato, "Propagation of a spherical wave near a plane boundary with a complex impedance," J. Acoust. Soc. Am. **60**, 34-39 (1976).

66. Alan R. Wenzel, "Propagation of waves along an impedance boundary," J. Acoust. Soc. Am. **55**, 956-963 (1974).

67. K. Attenborough, "Predicted ground effect for highway noise," J. Sound Vib. **81**, 413-424 (1982).

68. Keith Attenborough and Yu Chen, "Surface waves at an interface between air and an air-filled poroelastic ground," J. Acoust. Soc. Am. **87**, 1010-1016 (1990).

69. Jack W. Reed, "Atmospheric attenuation of explosion waves," J. Acoust. Soc. Am. **61**, 39-47 (1977).

70. Richard Raspet, Jean Ezell, and Henry E. Bass, "Additional comments on and erratum for "Effect of finite ground impedance on the propagation of acoustic pulses" [J. Acoust. Soc. Am. **74**, 267-274 (1983)]," J. Acoust. Soc. Am. **77**. 1955-1958 (1985), p. 1956.

71. Allan D. Pierce, *Acoustics: An Introduction to Its Physical Principles and Applications* (Acoust. Soc. Am., Woodbury, NY, 1989), p. 44.

72. Wilfred E. Baker, *Explosions in Air*, (University of Texas Press, Austin, 1973), p. 54.

73. Jack W. Reed, "Atmospheric attenuation of explosion waves," J. Acoust. Soc. Am. **61**, 40 (1977).

74. Paul D. Schomer, "Predicting community response to blast noise," United States Army Construction Engineering Research Lab. Tech. Rep. E-17 (CERL-TR-E-17, December, 1973). Here, see Equation [Eq 2] and Table 3, p. 12.

75. Mark O. Anderson, "The propagation of a spherical N wave in an absorbing medium and its diffraction by a circular aperture," Appl. Res. Lab Tech. Rep. No. 77-5 (ARL-TR-74-25), AD-787878, Applied Research Laboratories, The University of Texas at Austin, Austin, TX (August 1974), p. 31.

76. Richard Feynman, *The Feynman Lectures on Physics*, Vol. 2 (Addison-Wesley, Reading, MA, 1964), p. 7-1.

77. Jean-Claude Sabonnadiere and Jean-Lois Coulomb, *Finite Element Methods in CAD: Electrical and Magnetic Fields*, English trans. by S. Salon, (North Oxford Academic, London, 1987), p. 50 and p. 108.

78. Claes Johnson, *Numerical Solution of Partial Differential Equations by the Finite Element Method* (Cambridge, New York, 1987).

79. Robert D. Richtmyer and K. W. Morton, *Difference Methods for Initial-Value Problems*, 2nd ed. (Wiley-Interscience, New York, 1967).

80. Harold L. Brode, "Numerical Solutions of Spherical Blast Waves," J. Appl. Phys. **26**, 766-775 (1950).

81. Harold L. Brode, "Blast wave from a spherical charge," Phys. Fluids **2**, 217-229 (1959).

82. B. M. Rao and G. W. Zumwalt, "A numerical method for predicting the pressure history of a sonic boom wave incident on arbitrarily oriented plane walls," J. Appl. Mech. **37**, 889-894 (1970).

83. Patrick J. Roache, *Computational Fluid Dynamics*, rev. ed. (Hermosa Publishers, Albuquerque, 1976), p. 307.

84. R. M. Alford, K. R. Kelley, and D. M. Boore, "Accuracy of finite-difference modeling of the acoustic wave equation," Geophysics **39**, 834-842 (1974).

85. N. J. Walkington and W. Eversman, "A numerical model of acoustic choking, part II: Shocked solutions," J. Sound Vib. **104**, 81-107 (1986).

86. N. J. Walkington and W. Eversman, "A numerical model of acoustic choking, part I: Shock free solutions," J. Sound Vib. **90**, 509-526 (1983).

87. L. Maestrello, A. Bayliss and E. Turkel, "On the interaction of a sound pulse with the shear layer of an axisymmetric jet," J. Sound Vib. **74**, 281-301 (1981).

88. A. Bayliss and L. Maestrello, "On the interaction of a sound pulse with the shear layer of an axisymmetric jet, II. Heated jets," J. Sound Vib. **86**, 395-409 (1982).

89. A. Bayliss, L. Maestrello, and E. Turkel, "On the interaction of a sound pulse with the shear layer of an axisymmetric jet, III: Non-linear effects," J. Sound Vib. **107**, 167-175 (1986).

90. Alvin Bayliss and Lucio Maestrello, "Simulation of instabilities and sound radiation in a jet," AIAA J. **19**, 835-841 (1981).

91. L. Maestrello and A. Bayliss, "Flowfield and far field acoustic amplification properties of heated and unheated jets," AIAA J. **20**, 1539-1546 (1982).

92. David Gottlieb and Eli Turkel, "Dissipative two-four methods for time-dependent problems," Math. Comp. **30**, 703-723 (1976).

93. S. I. Hariharan, "Nonlinear acoustic wave propagation in the atmosphere," NASA Contractor Rep. 178069, ICASE Rep. No. 86-10, March 1986.

94. Gilbert Strang, "On the construction and comparison of difference schemes," SIAM J. Numer. Anal. **5**, 506-517 (1968).

95. Eli Turkel, "On the Practical Use of High-Order Methods for Hyperbolic Systems," J. Comp. Phys. **35**, 319-340 (1980), p. 322.

96. Stephen Wolfram, *Mathematica, A System for Doing Mathematics by Computer* (Addison-Wesley, Redwood City, CA, 1988).

97. Lloyd Nicholas Trefethen, "Wave propagation and stability for finite difference schemes," Ph. D. thesis, Stanford Univ., 1982.

98. Lloyd N. Trefethen, "Group velocity in finite difference schemes," SIAM Rev. **24**, 113-136 (1982).

99. Victor Ward Sparrow, "A finite difference model for arbitrary acoustic pulses applicable in investigating finite ground impedance effects," M. S. thesis, Univ. of Illinois, Urbana-Champaign, 1987.

100. Contact National Center for Supercomputing Applications, 152 Computing Applications Building, 605 East Springfield Avenue, Champaign, IL 61820, (217) 244-0072.

101. R. Higdon, "Absorbing boundary conditions for difference approximations to the multi-dimensional wave equation," Math. Comp. **47**, 437 - 459 (1986).

102. R. Higdon, "Numerical absorbing boundary conditions for the wave equation," Math. Comp. **49**, 65 - 90 (1987).

103. R. G. Keys, "Absorbing boundary conditions for acoustic media," Geophysics **50**, 892 - 902 (1985).

104. B. Engquist and A. Majda, "Absorbing boundary conditions for the numerical simulation of waves," Math. Comp. **31**, 629 - 651 (1977).

105. B. Engquist and A. Majda, "Radiation boundary conditions for acoustic and elastic wave calculations," Commun. Pure Appl. Math. **32**, 313 - 357 (1979).

106. D. Gottlieb, M. Gunzburger, and E. Turkel, "On numerical boundary treatment of hyperbolic systems for finite difference and finite element methods," SIAM J. Numer. Anal. **19**, 671 - 682 (1982).

107. W. Coughran, Jr., "On noncharacteristic boundary conditions for discrete hyperbolic initial-boundary-value problems," J. Comp. Phys. **60**, 135-154 (1985).

108. R. Higdon, "Initial-boundary value problems for linear hyperbolic systems," SIAM Rev. **28**, 177 - 217 (1986).

109. A. Bayliss and E. Turkel, "Radiation boundary conditions for wave-like equations," Commun. Pure Appl. Math. **33**, 707 - 725 (1980).

110. A. Bayliss and E. Turkel, "Boundary conditions for exterior acoustic problems," in *Advances in Computer Methods for Partial Differential Equations-III*, R. Vichnevetsky and B. Stepleman, eds. (IMACS, 1979), pp. 127-131.

111. T. Hagstrom and S. Hariharan, "Accurate boundary conditions for exterior problems in gas dynamics," Math. Comp. **51**, 581-597 (1988).

112. B. Gustafsson, "Inhomogeneous conditions at open boundaries for wave propagation problems," Appl. Num. Math. **4**, 3-19 (1988).

113. A. Majda and S. Osher, "Initial-boundary value problems for hyperbolic equations with uniformly characteristic boundary," Commun. Pure Appl. Math. **28**, 607 - 675 (1975).

114. Robert D. Richtmyer and K. W. Morton, *Difference Methods for Initial-Value Problems,* 2nd ed. (Wiley-Interscience, New York, 1967), pp. 66-67.

115. Marsha J. Berger, "Stability of interfaces with mesh refinement," Math. Comp. **45**, 301-318 (1985).

116. George W. Swenson, Jr., *Principles of Modern Acoustics* (Van Nostrand, New York, 1953), pp. 88-91.

117. Allan D. Pierce, *Acoustics: An Introduction to Its Physical Principles and Applications* (Acoust. Soc. Am., Woodbury, NY, 1989), pp. 111-113.

118. "American national standard method for the calculation of the absorption of sound in the atmosphere," ANSI Standard S1.26/ASA23-1979.

119. Henry E. Bass, Jean Ezell, and Richard Raspet, "Effect of vibrational relaxation on the rise times of shock waves in the atmosphere," J. Acoust. Soc. Am. **74**, 1514-1517 (1983).

120. Lawrence E. Kinsler, Austin R. Frey, Alan B. Coppens, and James V. Sanders, *Fundamentals of Acoustics,* 3rd ed. (John Wiley, New York, 1982), p. 147.

121. David T. Blackstock, "Nonlinear acoustics (theoretical)," in *AIP Handbook*, 3rd ed. (McGraw-Hill, New York, 1972), p. 3-203.

122. S. Glasstone, ed. *The Effects of Nuclear Weapons,* U.S. Atomic Energy Commission, rev. ed., April 1962, p. 147.

123. Gilbert F. Kinney and Kenneth J. Graham, *Explosive Shocks in Air,* 2nd ed. (Springer Verlag, New York, 1985), p. 82.

124. C. W. Heaps, K. S. Fansler, and E. M Schmidt, "Computer implementation of a muzzle blast prediction technique," The Shock and Vibration Bulletin, (Shock and Vibration Information Center, Naval Research Laboratory, Washington) **56**, 213-228 (August, 1986).

125. Allan D. Pierce, *Acoustics: An Introduction to Its Physical Principles and Applications* (Acoust. Soc. Am., Woodbury, NY, 1989), p. 561.

126. Jack W. Reed, "Atmospheric attenuation of explosion waves," J. Acoust. Soc. Am. **61**, 40 (1977).

127. Program **gzero**. Contact Dr. Mike White, USA-CERL, PO BOX 4005, Champaign, IL, 61824-4005.

128. Richard Raspet, Henry E. Bass, and Jean Ezell, "Effect of finite ground impedance on the propagation of acoustic pulses," J. Acoust. Soc. Am. **74**, 272 (1983).

129. Chi-Wang Shu and Stanley Osher, "Efficient implementation of essentially non-oscillatory shock capturing schemes, II," NASA Contractor Rep. 181656, ICASE Rep. No. 88-24, April 1988.

130. Ami Harten, "Preliminary results on the extension of ENO schemes to two-dimensional problems," in *Nonlinear Hyperbolic Problems*, C. Carasso, P.-A. Raviart, and D. Serre, eds., Springer-Verlag Lecture Notes in Mathematics No. 1270, pp. 23-40.

131. Peter Ilyich Tchaikovsky, *1812, Overture Solennelle, Op. 49.* The International Music Edition: Orchestral Scores, Volume 2. (Books and Music, Inc., New York, 1939).

132. J. Paul Barnett (private communication).

VITA

Victor Ward Sparrow was born on February 18, 1963 in Salina, Kansas. He attended public school in the Roanoke City School System, Roanoke, VA and there graduated from William Fleming High School as a co-salutatorian in 1981. During high school Mr. Sparrow played violin with the Roanoke Youth Symphony.

For undergraduate preparation he attended Duke University, Durham, NC in electrical engineering. Mr. Sparrow was given a full scholarship his last two years at Duke, in exchange for running the EE department's mainframe computer, a Data General MV/8000, as system administrator. He developed software to support both faculty and graduate student research and undergraduate teaching. Mr. Sparrow graduated from Duke in 1985 summa cum laude with the degree of Bachelor of Science in Engineering, receiving the honors of the George Sherrard III Memorial Award in Electrical Engineering and the Schlumberger Collegiate Award. While at Duke he was elected to Phi Beta Kappa, Tau Beta Pi, and Eta Kappa Nu.

Mr. Sparrow next began graduate work in acoustics at the University of Illinois, Urbana-Champaign in the Department of Electrical and Computer Engineering under Richard Raspet. He was supported throughout his graduate training by the United States Army Construction Engineering Research Laboratory (USA-CERL) in Champaign, IL. Mr. Sparrow received the degree of M.S. in 1987 and married C. Jan Carpenter on August 1 of that year. He has coauthored numerous abstracts for conference presentations at Acoustical Society of America meetings.